COMPUTATIONAL MODELING OF DUSTY NUCLEAR STARBURST DISKS AND ITS CONSEQUENCES ON OBSERVABLES

A Dissertation
Presented to
The Academic Faculty

By

Raj Gohil

In Partial Fulfillment
of the Requirements for the Degree
Doctor of Philosophy in the
School of Physics

Georgia Institute of Technology

August 2018

Copyright © Raj Gohil 2018

COMPUTATIONAL MODELING OF DUSTY NUCLEAR STARBURST DISKS AND ITS CONSEQUENCES ON OBSERVABLES

Approved by:

Dr. David Ballantyne, Advisor
School of Physics
Georgia Institute of Technology

Dr. John Wise
School of Physics
Georgia Institute of Technology

Dr. Tamara Bogdanovic
School of Physics
Georgia Institute of Technology

Dr. Carol Paty
School of Earth and Atmospheric Sciences
Georgia Institute of Technology

Dr. Gongjie Li
School of Physics
Georgia Institute of Technology

Date Approved: May 14, 2018

“There is a theory which states that if ever anyone discovers exactly what the Universe is for and why it is here, it will instantly disappear and be replaced by something even more bizarre and inexplicable.

There is another theory which states that this has already happened.”

–Douglas Adams

To my parents and sister:

"*The family is one of nature's masterpieces.*"–George Santayana

ACKNOWLEDGEMENTS

The success of a long voyage is not possible without the love and support of many. I am grateful to my family for their love and support for the last 27 years. Especially, I am indebted to my mother, Dharmendraben Gohil, for guiding me as a person. I would like to thank my high school teacher, Sanjay Talati, for providing me with a strong mathematical foundation. I must thank all my teachers as well as the counselor of the Crescenta Valley High school for providing a very friendly, supportive, and encouraging environment during the time when I first moved to the U.S.A. This really made a positive impact on my academics. I am thankful to all professors of physics and mathematics of the El Camino College for providing a great training in fundamentals. I would like to thank the University of California - Los Angeles as well as the Georgia Institute of Technology for providing all the great in-depth lectures, especially to Prof. Terry Tomboulis (for quantum mechanics courses). Most importantly, I would like to express my sincere gratitude to my advisor Prof. David Ballantyne for his guidance in the field of Astrophysics and also for his patience.

TABLE OF CONTENTS

LIST OF TABLES

LIST OF FIGURES

SUMMARY

Active galactic nuclei (AGNs) are the most energetic non-explosive objects in the universe whose comoving space density peaks near redshift $z \sim 2$ (Wolf et al., 2003). They radiate energy across the electromagnetic spectrum from radio to gamma rays. The number density of AGNs and their luminosity function with redshift play a key role in the evolution of massive black holes. They can also provide a feedback mechanism that can regulate galaxy growth, thus playing an important role in galaxy formation and their evolutionary models. However, the study of AGNs can be extremely complicated. There are numerous AGN classes dependent on physical characteristics such as luminosity, amount of obscuration, and observed emission lines. Many AGNs are observed to be obscured by dust and gas (Alexander & Hickox, 2012; LaMassa et al., 2017). The geometrical and physical conditions of these regions are not well understood. Moreover, obscured AGNs play an important role in explaining the cosmic X-ray background (Gilli et al., 2007; Akylas et al., 2012). Dusty nuclear starburst disks (NSDs) could potentially obscure the AGN in Seyfert galaxies (Ballantyne, 2008). I worked on testing this hypothesis by modeling the two-dimensional structure of NSDs. Since these disks are dusty, the atmosphere of a disk can be expanded when the dust sublimates near mid-plane. The expanded dusty atmosphere (near the surface) can then be supported by stellar radiation pressure (Thompson et al., 2005). NSDs could be a key to understanding the relation among the observed AGN obscuration, cosmic X-ray background, and star-forming regions at intermediate redshift.

CHAPTER 1

BACKGROUND

1.1 Introduction

Active galactic nuclei (AGNs) are nuclear regions in many galaxies whose luminosity is more than billion times higher luminosity than the solar luminosity. The responsible mechanism is thought to be accretion onto a central body (Balbus, 2003). As gas accretes towards a black hole, its potential energy is converted into radiation across the electromagnetic spectrum from radio to gamma rays. These galaxies show the presence of a supermassive black hole at its nucleus (Kormendy & Richstone, 1995) which are capable of extracting energy from its surroundings with extreme efficiency $\eta_{rad} \sim 0.1$ (Marconi et al., 2004; Merloni, 2004) which is higher by an order of magnitude in comparison to the efficiency of energy extraction in nuclear fusion, ~ 0.007. Many AGNs are observed to show the following features (Netzer, 2015): (1) accretion disk at sub-parsec scale, (2) non-Gaussian and asymmetric emission lines (Stirpe, 1991; Corbin, 1995) from a broad line region (BLR) of high density gas (dust-free) clouds at 0.01-1 pc moving with 10^3-10^4 km s^{-1}, (3) a dusty torus at 0.1-10 parsec scale, (4) narrow line region (NLR) of low density-ionized gas moving with hundreds of km s^{-1} which resides from hundreds to thousands of parsec, and (5) maser disks and/or radio jet. Some of these features are shown in Fig. 1.1. A traditional unification scheme suggests that AGNs with different features are the same type of objects and the observed variance is due to the different orientations of AGNs with respect to an observer (Antonucci, 1993; Urry & Padovani, 1995). AGNs are mainly divided into two classes: ones showing broad emission lines (BELs) are classified as type-I and others showing no presence of BELs, possibly due to obscuration (i.e. dusty obscuring pc-scale torus; Antonucci, 1993), are classified as type-II. Besides BELs, type-I AGNs also show highly

ionized narrow emission lines (NELs) unless they have high luminosity (Netzer, 2015). On the other hand, type-II AGNs show NELs in their spectra; however, in recent years, mid-IR (MIR) BELs are observed in polarized light from optically selected Seyfert 2 galaxies (Lumsden & Alexander, 2001; Tran, 2001). These AGNs are sub-classified as "hidden type-I" and others are called "true type-II" AGNs (Netzer, 2015). A majority of AGNs discovered by Chnadra and XMM-Newton (in thousands) show a presence of obscuration by dust and gas (Brandt & Hasinger, 2005; Gilli et al., 2007; Alexander & Hickox, 2012). The mechanisms and physical conditions responsible behind this obscuration are still not well understood.

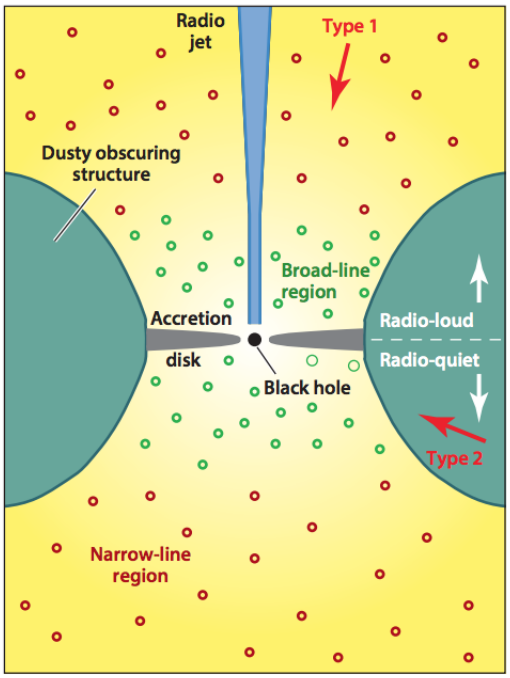

Figure 1.1: Graphical representation of the central region of AGNs illustrates some key features: a geometrically thin-optically thick accretion disk, broad-line region, narrow-line region, dusty obscuring medium, radio jet as well as Type-1 and Type 2 classes of AGNs (Heckman & Best, 2014).

Recent studies of obscured AGNs require the modification of a simple unification scheme which is based on orientation with respect to an observer. X-ray observations

show that the fraction of obscured AGNs depends on luminosity: higher fraction of obscured AGNs at lower luminosity (Lawrence & Elvis, 2010). Moreover, the obscured AGN fraction also shows evolution with redshift (Ballantyne et al., 2006b; Hasinger, 2008). This evidence points toward a nuclear obscuration due to the AGN feedback (Hopkins et al., 2006; Menci et al., 2008). Moreover, young stellar populations are found in the inner regions of close by AGNs (e.g. González Delgado et al., 2001; Gu et al., 2001; Cid Fernandes et al., 2004; Storchi-Bergmann et al., 2005) including Seyfert galaxies (Davies et al., 2007). Davies et al. (2007) highlights a possible causality between star-formation and AGN activity (time delay of $\approx$ 50-200 Myrs with the AGN activity peaking at later) by studying nine nearby Seyfert galaxies. Such causality suggests a possible fueling of gas toward a central black hole by stellar winds and supernovae (e.g Vollmer et al., 2008; Hopkins, 2012), perhaps indicating a strong coupling among star-formation, stellar winds/supernovae, and the AGN activity. From observations, the star-formation rate (SFR) is observed to be rising with redshift from 0 to 1, peaking between 2 and 3, then afterward decreasing (Shankar et al., 2009) which is a similar evolution to the AGN activity (Ueda, 2015). The cosmic evolution of the cosmic SFR density and the number density of Compton-thin AGNs are illustrated in Fig. 1.2.

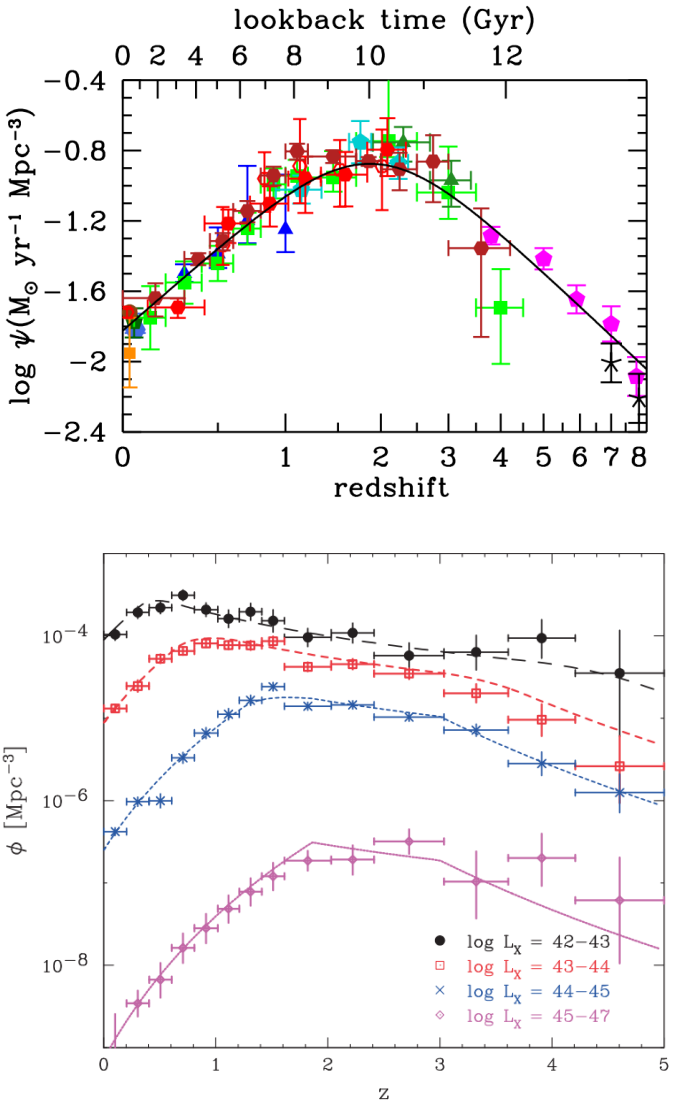

Figure 1.2: Figures illustrate that the cosmic evolution of the star-formation rate density and number density of Compton-thin AGNs has similar trend. *Top:* The figure shows the cosmic SFR density as a function of redshift based on the FUV (Far-Ultraviolet) and IR (infrared) measurements in rest-frame (Madau & Dickinson, 2014). *Bottom:* The figure shows the evolution of comoving density of Compton-thin AGNs for different luminosity bins (Ueda, 2015).

Additionally, the star-formation rate (from far-IR) shows the correlation with the hard X-ray AGN luminosity for redshift z<0.8 for the AGN bolometric luminosity greater than

$10^{43.5}$ erg s^{-1}; however, such a correlation is not observed at higher redshift (Rosario et al., 2013). Therefore, the star-forming regions in nucleus may be responsible for the observed obscuration in Seyfert galaxies at intermediate redshift z$\sim$1.

1.2 Dusty Star-forming Regions

The link between a host galaxy and its AGN has been confirmed via the observational correlation between the mass of the central supermassive black hole and velocity dispersion of the bulge (Ferrarese & Merritt, 2000; Gebhardt et al., 2000). As gas flows in the geometrically thin-optically thick accretion disk towards a black hole (at sub-parsec scale), the potential energy of the viscous gas flow is converted into intense radiation (the AGN spectrum). Infrared observation reveals the location of dusty obscuration of the AGN spectrum at parsec/sub-parsec scale (Burtscher et al., 2013, and references therein). Regions around AGNs are highly self-gravitating (Goodman, 2003; Levin, 2003; Tan & Blackman, 2005) and are radiation pressure on dust dominated (Sirko & Goodman, 2003). This kind of physical system is illustrated in Fig. 1.1. Due to the gravitational instabilities, the fragmentation of these regions would turn into the formation of stars. However, the fragmentation can be avoided if angular momentum is transported efficiently via global torque (i.e. bars, spiral waves and magnetic stresses) instead of viscosity (Mihos & Hernquist, 1996; Goodman, 2003). Only a small fraction of dusty gas is converted into stars due to an efficient accretion and gas is able to accrete radially resulting into a star-forming disk. However, the star-formation seizes when the region at sub-parsec scale becomes highly stable and the viscosity becomes a dominate transport. This location can be considered as a transition radius between the star-forming disk and accretion disk (AD).

By implementing such a phenomenon in a simple one-dimensional (1D) semi-analytical model, Thompson et al. (2005) shows that regions near the sublimation of dust temperature can inflate the atmosphere vertically. The expanded atmosphere is supported by the starburst formation at mid-plane and, in turn, this inflationary region can obscure the incoming

external irradiation of an AGN. Such a mechanism can build a bridge among star-forming regions, AGN activity, and observed obscuration. Using the model of Thompson et al. (2005), Ballantyne (2008) showed that there are various conditions (i.e. dependent on Mach number, black hole mass and gas fraction) of nuclear starburst disks (NSDs) which can be responsible for obscuration at parsec scale in Seyfert galaxies. Moreover, observational signatures can be predicted in radio and far-infrared (IR) which may be detected in the future surveys.

Molecular outflows are observed in many star-forming galaxies with the outflow speed of $\simeq 48 - 128$ km s^{-1} in NGC 1808 (Salak et al., 2016), $\simeq 23 - 42$ km s^{-1} in NGC 253 (Bolatto et al., 2013), ~ 90 km s^{-1} in NGC 3628 (Tsai et al., 2012), and ~ 100 km s^{-1} in M82 (Walter et al., 2002). From dynamical modeling perspective, to numerically simulate a dusty radiation pressure dominated atmosphere is not an easy task due to difficulties in solving the radiative transfer equation (RTE). Whether the dusty gas accelerated due to the radiation pressure achieves a steady-state conditions depends on the method used in solving the RTE: implicit Monte Carlo (Tsang & Milosavljević, 2015), M1 closure (Rosdahl & Teyssier, 2015), variable Eddington tensor (Davis et al., 2014), and flux limited diffusion (Krumholz & Thompson, 2012). For instance, the numerical simulation done by Krumholz & Thompson (2012) shows that the momentum exchange between radiation and dusty atmosphere can be limited due to the presence of Rayleigh-Taylor instabilities, while Davis et al. (2014) shows, under conditions with high luminosity and optically thick medium, gas is able to achieve enough acceleration where it never reaches to a steady-state condition. However, for a lower luminous radiation pressure, their simulations do show an existence of equilibrium. Stimulating observed outflows coherently is one of the open problems due to the challenges in solving the RTE. Therefore, we focus on the hydrostatic conditions which will be reasonable enough to explain obscuration if even partial regions of star-forming disks (i.e. near mid-plane) are in steady-state.

1.3 1D Model of Nuclear Starburst Disks

The one dimensional (1D) model of nuclear starburst disks (NSDs), including radiation physics, has been computed by Thompson et al. (2005). These models require four input parameters (a disk size $R_{\rm out}$, black hole mass $M_{\rm bh}$, gas fraction at the outer radius $f_{\rm g,out}$, and Mach number $m = v_r/c_s$, where v_r is the radial velocity and c_s is the total speed of sound) and compute the radial structure of these disks. A 1D model possesses a central black hole with a NSD rotating with the Keplerian frequency Ω and energy sources (star-formation and viscosity) at mid-plane. The Ω includes both potentials of a black hole and a bulge,

$$\Omega(r) = \Big(\frac{GM_{BH}}{r^3} + \frac{2\sigma^2}{r^2}\Big)^{1/2}, \tag{1.1}$$

where the dispersion σ is computed using the M-σ relation (Ferrarese & Merritt, 2000; Gebhardt et al., 2000; Tremaine et al., 2002)

$$M_{BH} = 2 \times 10^8 \Big(\frac{\sigma}{200 \text{ km s}^{-1}}\Big)^4 M_\odot. \tag{1.2}$$

The stability of the disk is always governed by the Toomre parameter Q (parametrizing the stability of a disk against gravitational collapse)[1]. A gas fraction $f_{\rm g,out}$ is injected at an outer radius $R_{\rm out}$ of the disk which is driven towards a black hole at the constant Mach number $m = v_r/c_s$ through presumed global torque (which can be due to a spiral instability or a bar; Goodman (2003)). As gas accretes toward the black hole, the star-formation adjusts to maintain the Toomre criteria Q and to provide the vertical support against gravity. The Toomre parameter Q is maintained to be 1 because there is an observational evidence in the Milky Way (Binney & Tremaine, 1987), local spiral galaxies (Martin & Kennicutt, 2001), and starbursts (Downes & Solomon, 1998) for Q$\simeq$1.

[1]The Toomre parameter parameterizes the stability of a differentially rotating Keplerian disk. The disk is stable if $Q \geq 1$ and this criteria can be obtained with a perturbation analysis of the Poisson potential in the rotating frame.

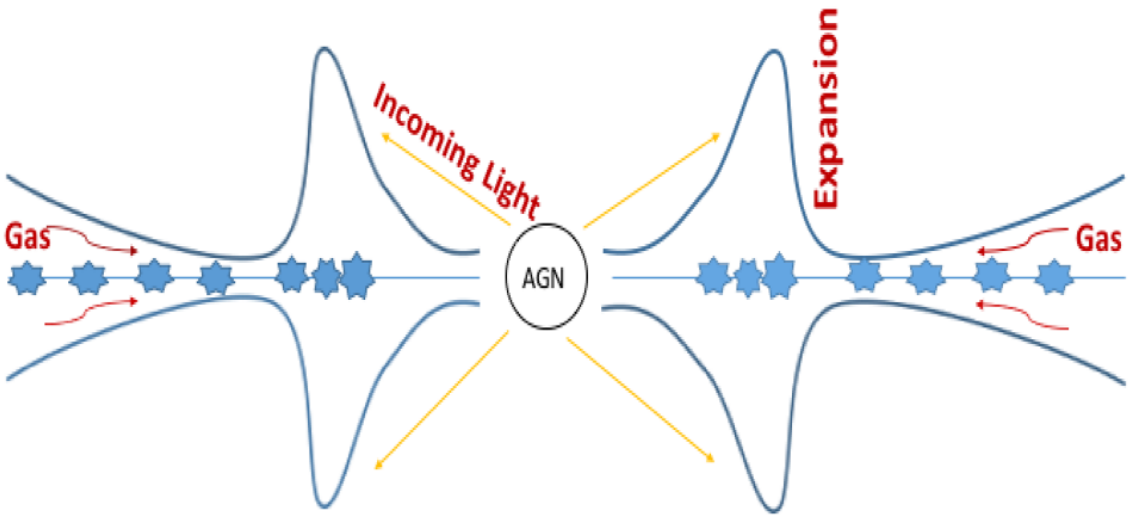

Figure 1.3: Graphical representation of a nuclear starburst disk. The figure illustrates the symmetry of a disk around $z = 0$ plane and $z-$axis as well as obscuration of the AGN light due to the expansion of an atmosphere which is supported by the starburst phenomenon at mid-plane.

The schematic of a nuclear starburst disk is illustrated in Fig. 1.3. As gas accretes toward the central black hole, star-formation occurs and the amount of available gas decreases with radius. When the temperature at mid-plane exceeds the dust sublimation temperature, the disk becomes geometrically thick due to the loss of dust opacity and the vertically expanded atmosphere is supported by the radiation pressure from a starburst formation. This geometrically thick region can obscure the incoming AGN radiation. At some inner radius $R_{\rm in}$, the energy production from viscosity takes over the star-formation energy and the $R_{\rm in}$ is considered as the transition radius between an NSD and accretion disk (AD). The upper limit on accretion luminosity is computed using the accretion rate $\dot{M}_{\rm in}$ at the inner radius. In the model of Thompson et al. (2005), the vertical structures are not computed except the scale-height of a photosphere $h_{\rm ph}$ is approximated by scaling mid-plane scale-height $h_{\rm mid}$ with the opacity ratio of $\kappa_{\rm ph}$ and $\kappa_{\rm mid}$:

$$h_{\rm ph} \approx h_{\rm mid} \frac{\kappa_{\rm ph}}{\kappa_{\rm mid}}. \tag{1.3}$$

The surface opacity is computed by approximating the surface temperature as the effective temperature. We relax these assumptions and compute the explicit structure of NSDs solving the coupled equations of hydrostatic balance, radiative transfer, and energy balance coherently to obtain the vertical properties of disks (i.e., density, temperature, total speed of sound, pressure, etc.). To understand all the minor details and physical significances of a model, one should start with the most basic model and iterate with additional complications. Moreover, for time-independent conditions, it is not possible to solve radial and vertical structures simultaneously. Therefore, a one-dimensional model is computed for the radial structure which is then used to construct the 2D structure of NSDs. In order words, radial and vertical structures are not coupled. We first successfully computed the radial structure of NSDs by following the work of Thompson et al. (2005). For example, the Fig. 5 of Thompson et al. (2005) is produced and shown in Fig. 1.4. The dashed and solid lines represent accretion rate and star-formation rate (SFR), respectively. The figure illustrates that, depending on the physical conditions, some NSDs show starburst phenomenon at parsec/sub-parsec scale. Various models dependent on input parameters for "Seyfert-like" conditions are computed and its results are discussed in Ballantyne (2008). Therefore, to look at the detailed analysis for the results of radial structures, a reader is referred to Thompson et al. (2005) and Ballantyne (2008).

We present results of one nuclear starburst disk: $f_{\rm g,out} = 80\%$ with the Mach number $m = 0.3$ supplied at the outer radius of 120 pc and the central black hole with the mass of $10^7\ M_\odot$. Useful physical quantities are plotted in Fig. 1.5. The figure illustrates that as gas is driven toward the black hole, density increases due to an increased in the vertical gravitational component. In return, there is decreased in scale-height h (middle-left panel), and

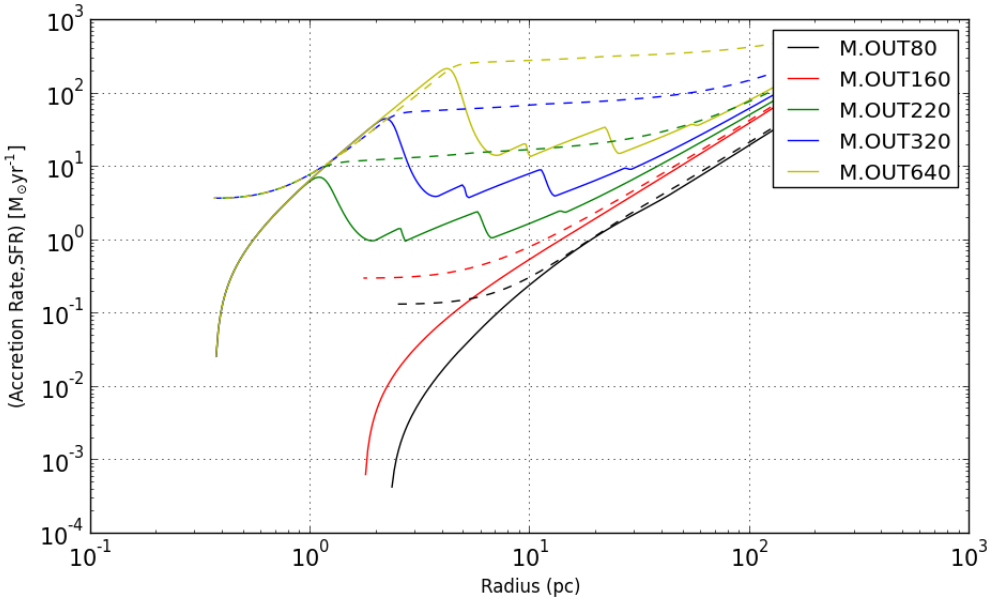

Figure 1.4: The figure shows the accretion rate (dashed lines) and star-formation rate (solid lines) as a function of radius for various models varying $\dot{M}_{\rm out} \in [80, 160, 220, 320, 640] M_\odot$ yr^{-1} with R$_{\rm out}$=200 pc, Mach number m=0.2, and velocity dispersion σ=300 km s^{-1}.

increased in the column density $\Sigma_{\rm mp}$ and optical depth τ (top-right panel). As the optical depth increases with radius, temperature T rises (result of the radiation transfer equation) which is shown in the top-left panel. When grains sublimate at the critical temperature (1400K and 1750K for silicate and graphite grains, respectively; Kishimoto et al. (2013)), a large opacity gradient occurs due to the loss of dust opacity which results in expanding an atmosphere (middle-left panel). For this model, the sublimation occurs at the critical radius of $R_{\rm cric} \sim 0.4$ pc which results in big starbursts (middle-right panel) to provide enough radiation pressure to balance against the gravitational component. The expansion of the atmosphere at $R_{\rm cric}$ exceeds the radial distance by orders of magnitudes. In other words, if we assume the disk is symmetric around azimuthal angle, then almost an entire sky is covered by the inflated atmosphere when viewed from the central black hole.

The spectrum energy distribution (SEDs) of the NSD is displayed in the bottom panel of Fig. 1.5 assuming the blackbody emission at each radius and face-on viewing angle

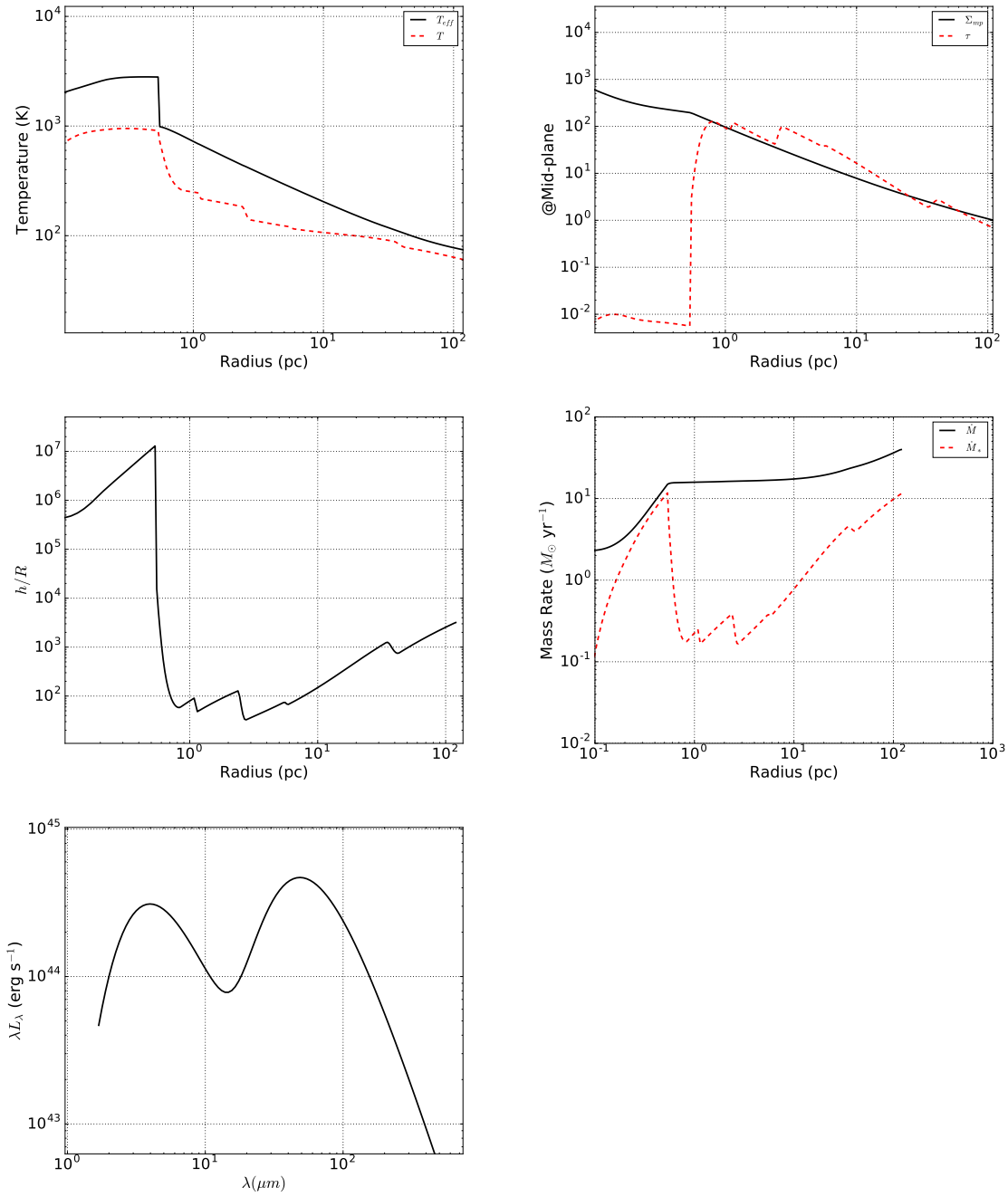

Figure 1.5: Illustrating a few important quantities for a NSD: 80% gas supply at the outer radius of 120 pc with 0.3 Mach number and the black hole mass of 10^7 $M_\odot$. Some important features: (1) The top-left panel shows the temperature (red curve) and the effective temperature (black curve). The top-right panel illustrates how the integrated mass column density (black curve) and optical depth (red curve) varies with radius. (2) The middle-left panel shows an expansion of the scale-height h near 0.4 pc exceeding the radial distance by orders of magnitude due to the starburst which is shown in the middle-right panel. In the middle-right panel, the red and black curves represent the star-formation rate and the accretion rate, respectively. And, (3) The SED of the disk is illustrated in the bottom panel showing two peak emissions at $\sim$4 μm and $\sim$50 μm.

(Thompson et al., 2005):

$$\lambda L_{\lambda}^{BB} = \frac{2\pi hc^2}{\lambda^4} \int_{R_{\text{in}}}^{R_{\text{out}}} \frac{2\pi R dR}{\exp[h_p c/\lambda k_B T_{\text{eff}}(R)] - 1}. \tag{1.4}$$

The black curve represents the blackbody emission parameterizing the Planck's function by the effective temperature T_{eff}. The SED shows two maxima at $\sim 4\ \mu m$ and $\sim 50\ \mu m$ due to two starbursts occurring at ∼0.4 pc and ∼2 pc, respectively. The reprocessing of UV emission from the starburst of parsec scale is limited due to the lost of opacity from grains and the resultant emission emerges into NIR regime (near-infrared). To compute the AGN luminosity, the accretion rate ($\dot{M}$) at the inner radius R_{in} of the NSD [2] is assumed to be the same as the accretion onto the black hole (providing an upper limit). Then, the bolometric AGN luminosity $L_{\text{bol}} = 10^{46.3}$ erg s^{-1} and the Eddington factor $f_{\text{Edd}} = 0.17$ are computed as

$$L_{\text{bol}} = \eta_{\text{rad}} \dot{M} c^2 \ \text{ and } \ f_{\text{Edd}} = L_{\text{bol}}/L_{\text{Edd}} \tag{1.5}$$

where η_{rad} is the radiative efficiency, typically 0.1 (Marconi et al., 2004; Merloni, 2004) and L_{Edd} is the Eddington luminosity defined as

$$L_{\text{Edd}} := 4\pi G M_{BH} m_p c/\sigma_T. \tag{1.6}$$

Again, these luminosities are the upper limit due to the restriction on $\dot{M}$.

1.4 Modeling of 2D Structure: From Accretion Disks to Nuclear Starburst Disks

Modeling of NSDs has a similar core as accretion disk (AD): (1) Both disks possess energy source with possibility of vertical distribution. (2) Energy sources in both type of disks has dependency on column density (e.g., Shakura & Sunyaev, 1973; Kennicutt, 1998).

[2] R_{in} is defined at radius when the flux produced from viscosity dominates over the flux from star-formation rate.

However, the main difference between NSDs and ADs is that the NSDs can be highly self-graviting (Toomre parameter Q<<1), while the ADs are highly gravitationally stable (Q>>1). There has been substantial amount of work done in modeling of ADs (e.g., Hubeny, 1990; Hubeny & Hubeny, 1998)). Hubeny (1990) has outlined major iterative steps to construct the vertical structure and the analytical frame work for an initially guessed solution as well as a treatment for inclusion of the AGN heating. His later paper, Hubeny & Hubeny (1998), describes on how to take care of a vertical distribution of an energy source, viscosity, which has a power-law dependency on the column density. Thus, using these papers as guidance, the idea is to construct vertical structures of ADs. Upon its success, we modify the theory with necessary changes needed for the environment of NSDs.

Here, I briefly summarize the foundation of modeling for vertical structure under hydrostatic condition of accretion disks. The AD with an energy source of viscosity was modeled by Hubeny (1990) using an iterative method. The vertical structure is approximated by assuming locally plane-parallel geometry. In order words, the radial distance is divided into annuli and vertical solutions of each annulus does not communicate with each other. Conduction and convection heat transports are excluded in modeling. The energy transport in the vertical direction is solely by radiation. The radiation flux from viscosity is parameterized by an effective temperature ($T_{\rm eff}$) since the energy is transported losslessly to the surface and then radiated away. The radial distribution of a column density at midplane $\Sigma_{\rm mp}$ and the energy content $T_{\rm eff}$ are computed using α_0 prescription of accretion disk model (Shakura & Sunyaev, 1973). In order to obtain solutions for a vertical structure at a given annulus, one is required to solve a coupled hydrostatic equation (HSE), radiative

transfer equation (RTE), and the energy balance equation (EBE).

$$\text{RTE}: \quad \frac{\delta I_\nu(\vec{r},t,\vec{n})}{\delta s} = \eta_\nu(\vec{r},\vec{n},t) - \chi_\nu(\vec{r},t) I_\nu(\vec{r},t,\vec{n}) \tag{1.7}$$

$$\text{HSE}: \quad \frac{d^2 P(\Sigma)}{d\Sigma^2} = -\frac{c_s^2(\Sigma)\Omega^2}{P(\Sigma)} \tag{1.8}$$

$$\text{EBE}: \quad P_{\text{tot}} = P_{\text{rad}} + P_{\text{gas}} + P_{\text{turb}} \tag{1.9}$$

The solution of the RTE is given by

$$T^4 = \frac{3}{4} {T_{\text{eff}}}^4 \Big[\tau + q(\tau)\Big] \tag{1.10}$$

where $q(\tau)$ is the Hopf function. For the derivation of the RTE solution, a reader is referred to Ch. 2.

A vertical structure of a column of gas Σ_{mp}, which is R distance away from a central body with the energy source parameterized by T_{eff}, is governed by the following highly coupled equations [3]:

$$P(\Sigma) = P_g(\Sigma) + P_r(\Sigma) = \frac{\rho(\Sigma) k T(\Sigma)}{m_p} + \frac{4\sigma_{sb}}{3c} T^4(\Sigma), \tag{1.11}$$

$$c_s^2(\Sigma) = \frac{P(\Sigma)}{\rho(\Sigma)}, \tag{1.12}$$

$$\kappa = \kappa\Big(\rho(\Sigma), T(\Sigma)\Big) \tag{1.13}$$

$$\tau(\Sigma) = \int_0^\Sigma \kappa(\rho, T) d\Sigma', \tag{1.14}$$

[3] Among the seven coupled equations, some are definitions. However, they are necessary to avoid indo-differential equations.

$$z(\Sigma) = \int_{\Sigma_{mp}}^{\Sigma} -\frac{1}{\rho(\Sigma')} d\Sigma', \tag{1.15}$$

$$T^4(\Sigma) = \frac{3}{4} {T_{\text{eff}}}^4 \Big[\tau(\Sigma) + q(\tau)\Big], \tag{1.16}$$

and (1.17)

$$\frac{d^2 P(\Sigma)}{d\Sigma^2} = -\frac{c_s^2(\Sigma)\Omega^2}{P(\Sigma)} \tag{1.18}$$

with the following boundary conditions[4]

$$P_{\text{mp}}(\Sigma_{\text{mp}}) = P_{\text{mp}} \text{ and } P_s(\Sigma_s) = P_s.$$

Analytical solution requires some prior knowledge of physical conditions of ADs (i.e., vertical distribution of a speed of sound and opacity). Due to the highly coupled nature of these equations and a lack of prior knowledge on distributions of any physical quantity, an iterative method becomes necessary.

1.4.1 Vertical Structure of NSDs

At fundamental level, both nuclear starburst disks and accretion disks have similar characteristics. The 2D structure of NSDs can be modeled with certain changes in the accretion disk model. First, an additional energy source, star-formation, is needed to include besides viscosity. The radial distribution of Σ_{mp} and energy sources (i.e., star-formation rate and viscosity) are computed using the Thompson et al. (2005) model rather than Shakura & Sunyaev (1973) theory. We also include a self-gravity term in the equation of hydrostatic balance. Since a NSD is highly gravitationally unstable, the Toomre criteria is forced to satisfy at mid-plane:

$$Q(\Sigma_{\text{mp}}) = \frac{c_s(\Sigma_{\text{mp}})\Omega}{\pi G \Sigma_{\text{mp}}} = 1.0. \tag{1.19}$$

[4]Subscript 's' and 'mp' represent quantities at surface and mid-plane, respectively.

A turbulence pressure P_t from stellar winds/supernovae is also included. The pressure from supernovae explosion into the cold ISM is given by (Thompson et al., 2005)

$$P_t(\Sigma) = 1.5 \times 10^8 \Big[\frac{E_0}{10^{51}}\Big]^{13/14} \Big[\frac{\rho(\Sigma)}{m_p}\Big]^{-1/4} \dot{\Sigma}_*. \tag{1.20}$$

Then, the turbulence speed associated with this pressure is

$$v_t = \Big(\frac{2P_t}{\rho}\Big)^{1/2}, \tag{1.21}$$

where $E_0 = 10^{51}$ ergs is the energy released from a supernova [5]. Moreover, the opacity $\kappa = \kappa(\rho, T)$ is computed using CLOUDY (Ferland et al., 2013).

By constructing the 2D structure of NSDs, we infer a distribution of column density along the line of sight $N_{\rm H}$ associated with these disks and compare against observational constraints. We also determine if these disks can obscure and fuel Seyfert galaxies at intermediate redshift $z \sim 1$ by modeling the associated cosmic X-ray background. Chapter 2 starts with the basic radiative transfer equation. It goes through all assumptions/approximations and finally derives the temperature solution which is used for the 2D theory of NSDs. Chapter 3 discusses the iterative algorithm used to solve coupled equations. A total of 192 NSD models are computed across the input parameter space and the statistical distribution of a column density along the line of sight $N_{\rm H}$ is predicted. Moreover, the chapter also discusses the impact of vertical distribution of star-formation on the structure of NSDs. Thereafter, Chapter 4 describes the methodology used to evolve the $N_{\rm H}$ distribution with redshift. The chapter predicts the cosmic X-ray background associated with nuclear starburst disks as well as the fraction of obscured quasars. In Chapter 5, the interaction between the AGN spectrum and a dusty column of gas is studied in order to explore the effect of dust on the equivalent width of Fe Kα. Finally, the thesis is concluded in Chapter 6.

[5] v_t is approximated to be a constant in the vertical direction using the density computed from a radial structure if the star-formation are only allowed to occur at mid-plane.

CHAPTER 2

RADIATIVE TRANSFER EQUATION

The intensity of radiation as it passes through material of a length ds is reduced due to an outward-scattering (from the line of slight) and absorption processes before it emerges besides the emissivity η of matter (the inward-scattering processes and thermal photons). The emerged light depends on the frequency ν of photons, time t, directional unit vector $\vec{n}$, and the spacial coordinate $\vec{r}$. This phenomenon can be formulated as

$$\frac{\delta I_\nu(\vec{r},t,\vec{n})}{\delta s} = \eta_\nu(\vec{r},\vec{n},t) - \chi_\nu(\vec{r},t) I_\nu(\vec{r},t,\vec{n}) \tag{2.1}$$

where δ is the absolute/total derivative and χ_ν [cm^{-1}] is the total extinction coefficient

$$\chi_\nu = \chi_\nu^{\text{abs}} + \chi_\nu^{\text{sct}}. \tag{2.2}$$

The χ_ν^{abs} and χ_ν^{sct} are absorption and scattering extinction coefficient, respectively. The Eq. 2.1 is the eight dimensional radiative transfer equation (RTE): t, ν, 3 spatial coordinates $\vec{r}$, and 3 momentum coordinates $\vec{n}$[1].

2.1 RTE: Assumptions and Method

To reduce the complexities and the dimensionality of the radiative transfer equation (RTE), we consider the following assumptions [2]:

1) Time independent (static).

2) Homogeneous plane-parallel geometry (azimuthal symmetry) where properties of mate-

[1] This is one of the standard treatments of RTE which may be found in various astrophysical books and papers (e.g., Hubeny, 1990; Hubeny & Mihalas, 2014).

[2] A sub-sequential derivation is done under previously mentioned assumptions.

rial only depends on the z-direction. In other words, χ_ν is isotropic.

$$\int_{2D} \chi_\nu I_\nu(z,\mu) d\Omega = \chi_\nu \int_{2D} I_\nu(z,\mu) d\Omega. \tag{2.3}$$

Then, the RTE becomes

$$\mu \frac{\partial I_\nu(z,\mu)}{\partial z} = \eta_\nu(\mu, z) - \chi_\nu I_\nu(z) \tag{2.4}$$

where μ is the directional cosine angle defined as $\cos(\theta)$. One of the basic quantity defined in radiation transfer problems is the source function $S_\nu(\mu, z)$

$$S_\nu(\mu, z) := \eta_\nu(\mu, z)/\chi_\nu(z). \tag{2.5}$$

A physical interpretation of S_ν is that it represents a total number of photons emitted in a unit interval of optical depth τ_ν which is defined as

$$d\tau_\nu := -\chi_\nu(z) dz := \kappa_\nu(z) d\Sigma. \tag{2.6}$$

κ_ν [cm^2 g^{-1}] and Σ [g cm^{-2}] are opacity and column density, respectively, defined as

$$\kappa_\nu(z) := \chi_\nu(z)/\rho \ \text{ and } \ d\Sigma := \rho dz. \tag{2.7}$$

Then,

$$\mu \frac{\partial I_\nu(z,\mu)}{\partial \Sigma} = \kappa_\nu(z) \Big[I_\nu(z) - S_\nu(\mu, z) \Big]. \tag{2.8}$$

3) Isotropic absorption and emission $\Rightarrow S_\nu(\mu, z) = S_\nu(z)$.

The emissivity has two contributors: thermal emission and inward scattering.

$$\eta_\nu = \eta_\nu^{\text{thermal}} + \eta_\nu^{\text{sct}} \tag{2.9}$$

Using the Kirchhoff's law under the assumption of local thermal equilibrium and the coherent isotropic scattering,

$$\eta_\nu^{\text{thermal}} = \chi_\nu^{\text{abs}} B_\nu \text{ and } \eta_\nu^{\text{sct}} = \chi_\nu^{\text{sct}} J_\nu, \tag{2.10}$$

the source function becomes

$$S_\nu(z) = \eta_\nu/\chi_\nu = \frac{\chi_\nu^{\text{abs}} B_\nu + \chi_\nu^{sct} J_\nu}{\chi_\nu} = \frac{\kappa_\nu^{\text{abs}} B_\nu + \kappa_\nu^{\text{sct}} J_\nu}{\kappa_\nu}, \tag{2.11}$$

where B_ν is the Planck function. Then the RTE is given by

$$\mu \frac{\partial I_\nu(z,\mu)}{\partial \Sigma} = \kappa_\nu^{\text{abs}} \Big(I_\nu - B_\nu \Big) + \kappa_\nu^{\text{sct}} \Big(I_\nu - J_\nu \Big). \tag{2.12}$$

Angular Moments

One of the methods to solve RTE is using angular moments $M_N(\nu, \vec{n})$, approximated angular distribution of a radiation field. The N$^{\text{th}}$ angular moment is defined as

$$M_\nu(N^{th}) := \frac{\oint_{2D} I_\nu(\mu, \phi, \tau_\nu) \mu^N d\Omega}{\oint_{2D} d\Omega} \tag{2.13}$$

$$\text{where } d\Omega = \sin\theta d\theta d\phi. \tag{2.14}$$

Using azimuthal symmetry (radiation field independent of ϕ),

$$\oint_{2D} d\Omega = \int_0^{2\pi} d\phi \int_0^{\pi} \sin\theta d\theta = 4\pi, \tag{2.15}$$

the N_{th} angular moment becomes

$$M_\nu(N_{th}) := \frac{1}{4\pi} \oint_{2D} I_\nu(\mu, \tau_\nu) \mu^N d\Omega. \tag{2.16}$$

Then, the zeroth, first, and second moments are

$$M_\nu(0^{th}) = \frac{1}{4\pi} \oint_{2D} I_\nu(\mu, \tau_\nu) d\Omega := J_\nu(\tau_\nu), \tag{2.17}$$

$$M_\nu(1^{st}) = \frac{1}{4\pi} \oint_{2D} I_\nu(\mu, \tau_\nu) \mu d\Omega := H_\nu(\tau_\nu), \text{ and} \tag{2.18}$$

$$M_\nu(2^{nd}) = \frac{1}{4\pi} \oint_{2D} I_\nu(\mu, \tau_\nu) \mu^2 d\Omega := K_\nu(\tau_\nu). \tag{2.19}$$

These three moments, respectively, are related to the energy density u_ν, flux F_ν, and pressure P_ν by

$$u_\nu = \frac{4\pi}{c} J_\nu, \quad F_\nu = 4\pi H_\nu, \quad \text{and} \quad P_\nu = \frac{4\pi}{c} K_\nu. \tag{2.20}$$

Moments Transfer Equations

We can substitute the definitions of angular moments into the radiation transfer equation.

$$\mu \frac{\partial I_\nu(z, \mu)}{\partial \Sigma} = \kappa_\nu^{\text{abs}} \Big(I_\nu - B_\nu \Big) + \kappa_\nu^{\text{sct}} \Big(I_\nu - J_\nu \Big) \tag{2.21}$$

The first moment transfer equation (MTE) becomes

$$\frac{1}{4\pi} \frac{\partial}{\partial \Sigma} \oint_{2D} I_\nu \mu d\Omega = \frac{\kappa_\nu^{\text{abs}}}{4\pi} \oint_{2D} (I_\nu - B_\nu) d\Omega + \frac{\kappa_\nu^{\text{sct}}}{4\pi} \oint_{2D} (I_\nu - J_\nu) d\Omega. \tag{2.22}$$

Since J_ν and B_ν are independent of Ω,

$$\frac{\partial H_\nu}{\partial \Sigma} = \kappa_\nu^{\text{abs}}(J_\nu - B_\nu) + \kappa_\nu^{\text{sct}}(J_\nu - J_\nu) \tag{2.23}$$

$$\frac{\partial H_\nu}{\partial \Sigma} = \kappa_\nu^{\text{abs}}(J_\nu - B_\nu). \tag{2.24}$$

The second MTE is

$$\begin{aligned}
\frac{1}{4\pi}\frac{\partial}{\partial \Sigma}\oint_{2D} I_\nu \mu^2 d\Omega &= \frac{\kappa_\nu^{\text{abs}}}{4\pi}\oint_{2D} \mu(I_\nu - B_\nu)d\Omega + \frac{\kappa_\nu^{\text{sct}}}{4\pi}\oint_{2D} \mu(I_\nu - J_\nu)d\Omega \\
\frac{1}{4\pi}\frac{\partial}{\partial \Sigma}\oint_{2D} I_\nu \mu^2 d\Omega &= \frac{\kappa_\nu}{4\pi}\oint_{2D} \mu I_\nu d\Omega - \frac{\kappa_\nu^{\text{abs}}}{4\pi}\oint_{2D} B_\nu \mu d\Omega - \frac{\kappa_\nu^{\text{sct}}}{4\pi}\oint_{2D} J_\nu \mu d\Omega \\
\frac{1}{4\pi}\frac{\partial}{\partial \Sigma}\oint_{2D} I_\nu \mu^2 d\Omega &= \frac{\kappa_\nu}{4\pi}\oint_{2D} \mu I_\nu d\Omega - \frac{\kappa_\nu^{\text{abs}}}{4\pi} B_\nu \oint_{2D} \mu d\Omega - \frac{\kappa_\nu^{\text{sct}}}{4\pi} J_\nu \oint_{2D} \mu d\Omega
\end{aligned}$$

Last two integrals are zeros. Then, the equation becomes

$$\frac{\partial K_\nu}{\partial \Sigma} = \kappa_\nu H_\nu. \tag{2.25}$$

We further consider the grey approximation (frequency integrated radiation field and opacity). Thus, the following equations

$$\frac{\partial H_\nu}{\partial \Sigma} = \kappa_\nu^{\text{abs}}(J_\nu - B_\nu) \text{ and } \frac{\partial K_\nu}{\partial \Sigma} = \kappa_\nu H_\nu \tag{2.26}$$

become frequency integrated

$$\frac{\partial H}{\partial \Sigma} = \kappa_J J - \kappa_B B \text{ and } \frac{\partial K}{\partial \Sigma} = \kappa_H H \tag{2.27}$$

where κ_J, κ_B and κ_H are absorption, Planck, and flux opacity, respectively. They are defined as:

$$\kappa_J(\Sigma) = \int_0^\infty \kappa_\nu^{\text{abs}} J_\nu d\nu / J, \tag{2.28}$$

$$\kappa_B(\Sigma) = \int_0^\infty \kappa_\nu^{\text{abs}} J_\nu d\nu / B, \tag{2.29}$$

$$\kappa_H(\Sigma) = \int_0^\infty \kappa_\nu H_\nu d\nu / H, \tag{2.30}$$

$$H(0) = \sigma_{\text{SB}} T_{\text{eff}}^4 / 4\pi, \tag{2.31}$$

$$B(\Sigma) = \frac{\sigma_{\text{SB}} T^4}{\pi}. \tag{2.32}$$

2.2 RTE: Solution

Using angular moments, we want to acquire the temperature solution of the radiative transfer equation [3]. Solving coupled first and second moment equations, respectively

$$\frac{\partial H}{\partial \Sigma} = \kappa_J J - \kappa_B B \text{ and } \frac{\partial K}{\partial \Sigma} = \kappa_H H \tag{2.33}$$

has a closure problem since there are three unknowns ($J, H,$ and, K) and two equations. The solution can be obtained using the following Eddington approximations:

1)$f_k(\tau) := \frac{K(\tau)}{J(\tau)}$ and

2)$f_H(\tau = 0) := \frac{H(\tau=0)}{J(\tau=0)}$.

These provides the third equation and a boundary condition needed for differentiation. In stellar atmosphere problem, the system is in radiative equilibrium such that

$$\frac{\partial H}{\partial \Sigma} = \kappa_J J - \kappa_B B = 0. \tag{2.34}$$

[3]This is one of the standard treatments for the RTE (e.g., Hubeny, 1990; Hubeny & Mihalas, 2014).

However, this is not the case for NSDs due the presence of energy source, the star-formation rate. The vertical distribution of the energy source can be formulated as

$$F(\Sigma) = F_1\Big[1 - \Psi(\Sigma)\Big] \text{ or } H(\Sigma) = H_1\Big[1 - \Psi(\Sigma)\Big]. \tag{2.35}$$

Here, F_1 is the flux emerging from the top surface layer and $\Psi(\Sigma)$ is the normalized distribution function of the energy source defined as

$$\Psi(\Sigma) := \frac{1}{\psi_1 \Sigma_{\text{mp}}} \int_0^{\Sigma} \psi(\Sigma')d\Sigma'. \tag{2.36}$$

Then, the first MTE is given by

$$\frac{\partial H}{\partial \Sigma} = \kappa_J J - \kappa_B B = -\frac{H(\Sigma)}{\Sigma_{\text{mp}}}. \tag{2.37}$$

Let's substitute the Eddington approximations and Eq. 2.35 into the Eq. 2.33 in order to obtain $J(\Sigma)$.

$$\begin{aligned}
\frac{\partial K}{\partial \Sigma} = \frac{\partial}{\partial \Sigma}(J f_k) &= \kappa_H H \\
J(\Sigma) f_k(\Sigma) - J(0) f_k(0) &= \int_0^{\Sigma} \kappa_H d\Sigma' \\
&= \int_0^{\Sigma} \kappa_H H_1\Big[1 - \Psi(\Sigma)\Big] d\Sigma' \\
&= H_1 \int_0^{\Sigma} \kappa_H d\Sigma' - H_1 \int_0^{\Sigma} \kappa_H \Psi(\Sigma) d\Sigma' \\
&= H_1(\tau_H - \tau_\Psi)
\end{aligned}$$

where

$$\tau_H := \int_0^{\Sigma} \kappa_(\Sigma) d\Sigma' \text{ and } \tau_\Psi := \int_0^{\Sigma} \kappa_H(\Sigma)\Psi(\Sigma) d\Sigma'$$

This gives

$$J(\Sigma) = \frac{1}{f_k(\Sigma)}\Big[J(0)f_k(0) + H_1\Big(\tau_H - \tau_\Psi\Big)\Big]. \tag{2.38}$$

Using the 1st MTE, we get

$$\frac{\partial H}{\partial \Sigma} = \kappa_J J - \kappa_B B = -\frac{H(\Sigma)}{\Sigma_{\text{mp}}}.$$

and

$$J(\Sigma) = \frac{1}{\kappa_J(\Sigma)}\Big[\kappa_B(\Sigma)B(\Sigma) - \frac{H(\Sigma)}{\Sigma_{\text{mp}}}\Big]. \tag{2.39}$$

We can solve for $B(\Sigma)$ by equating Eq. 2.38 and 2.39,

$$B(\Sigma) = 3H_1\Big[\frac{\kappa_J}{3\kappa_B f_k}\Big\{\frac{J(0)f_k(0)}{H_1} + \tau_H - \tau_\Psi\Big\} + \frac{H(\Sigma)}{3\Sigma_{\text{mp}}\kappa_B H_1}\Big]. \tag{2.40}$$

With

$$H_1 = H(0) = \sigma_{\text{SB}}T_{\text{eff}}^4/4\pi, \;\; B(\Sigma) = \frac{\sigma_{\text{SB}}T^4}{\pi}, \;\; \text{and} \;\; f_H = H(0)/J(0), \tag{2.41}$$

the temperature profile is computed to be

$$T^4(\Sigma) = \frac{3}{4}T_{\text{eff}}^4\Big[\frac{\kappa_J}{3\kappa_B f_k}\Big\{\frac{f_k(0)}{f_H} + \tau_H - \tau_\Psi\Big\} + \frac{H(\Sigma)}{3\Sigma_{\text{mp}}\kappa_B H_1}\Big]. \tag{2.42}$$

This can be rewritten as

$$T^4(\Sigma) = \frac{3}{4}T_{\text{eff}}^4\Big[\tau_H(\Sigma) + q(\Sigma)\Big]. \tag{2.43}$$

Then, the Hopf function q becomes

$$q(\Sigma) = \gamma_J \Big[\frac{f_k(0)}{f_H} + \Big(\frac{\gamma_J - 1}{\gamma_J} \Big) \tau_H - \tau_\Psi + \gamma_H \Big], \tag{2.44}$$

where

$$\gamma_J := \kappa_J / 3\kappa_B f_k \ \text{ and } \ \gamma_H := H(\Sigma)/3\Sigma_{\text{mp}} H_1. \tag{2.45}$$

2.3 Vertical Distribution of Energy Sources

The vertical distribution of an energy source which possess a power-law dependency on a column density (Σ) can be formulated using a similar frame-work done for an accretion disk model by Hubeny & Hubeny (1998) [4]. Their work suggests that the single power-law distribution can lead to the density inversion in the deep layers and also the "thermal catastrophe" in the low optical depth. This may be resolved using a broken power-law distribution (dividing a slab between the surface-layers and deep-layers with δ_s and δ_d power-law exponents, respectively). Then, a distribution of energy source ψ is formulated as:

$$\psi(\Sigma) = \psi_s (\Sigma / \Sigma_{\text{mp}})^{\delta_s}, \ \ \Sigma < \Sigma_d \ \text{ and} \tag{2.46}$$

$$\psi(\Sigma) = \psi_d (\Sigma / \Sigma_{\text{mp}})^{\delta_d}, \ \ \Sigma > \Sigma_d \tag{2.47}$$

where Σ_d is the dividing layer between surface-layers and deep-layers [5]. The fraction of energy sources in the surface-layers f_s and in the deep layers f_d are given by

[4] This is the reproduced work which is done in (Hubeny & Hubeny, 1998).

[5] Subscripts 's' and 'd' represents surface-layers and deep-layers, respectively.

$$f_s\psi_1 = \frac{1}{\Sigma_{\rm mp}}\int_0^{\Sigma_d}\psi(\Sigma)d\Sigma \;\text{ and }\; f_d\psi_1 = \frac{1}{\Sigma_{\rm mp}}\int_{\Sigma_d}^{\Sigma_{\rm mp}}\psi(\Sigma)d\Sigma \tag{2.48}$$

$$f_s\psi_1 = \frac{\psi_s}{\Sigma_{\rm mp}}\int_0^{\Sigma_d}(\Sigma/\Sigma_{\rm mp})^{\delta_s}d\Sigma \;\text{ and }\; f_d\psi_1 = \frac{\psi_d}{\Sigma_{\rm mp}}\int_{\Sigma_d}^{\Sigma_{\rm mp}}(\Sigma/\Sigma_{\rm mp})^{\delta_d}d\Sigma \tag{2.49}$$

$$f_s\psi_1 = \frac{\psi_s}{\delta_s+1}(\Sigma_d/\Sigma_{\rm mp})^{\delta_s+1} \;\text{ and }\; f_d\psi_1 = \frac{\psi_d}{\delta_d+1}\Big[1-(\Sigma/\Sigma_{\rm mp})^{\delta_d+1}\Big] \tag{2.50}$$

where ψ_1 is the total energy sources responsible for an overall emergent flux from the top surface $F(\Sigma = 0)$. Since $f_s + f_d = 1$, the total energy sources in the surface and deep layers are formulated to be

$$\psi_s = \psi_1\frac{(1-f_d)(\delta_s+1)}{(\Sigma_d/\Sigma_{\rm mp})^{\delta_s+1}} \;\text{ and }\; \psi_d = \psi_1\frac{f_d(\delta_d+1)}{1-(\Sigma_d/\Sigma_{\rm mp})^{\delta_d+1}}. \tag{2.51}$$

Demanding the distribution function to be continuous at the dividing layer Σ_d, the relationship between f_d and Σ_d is given by

$$\Sigma_d = \Sigma_{\rm mp}\left(1+\frac{f_d}{1-f_d}\frac{\delta_d+1}{\delta_s+1}\right)^{-1/(\delta_d+1)}. \tag{2.52}$$

The normalized distribution function of the energy source Ψ is

$$\Psi(\Sigma) := \frac{1}{\psi_1\Sigma_{\rm mp}}\int_0^{\Sigma}\psi(\Sigma')d\Sigma' \tag{2.53}$$

where

$$\psi(\Sigma) = \psi_s(\Sigma/\Sigma_{\rm mp})^{\delta_s},\;\; \Sigma < \Sigma_d \tag{2.54}$$

$$\psi(\Sigma) = \psi_d(\Sigma/\Sigma_{\rm mp})^{\delta_d},\;\; \Sigma > \Sigma_d. \tag{2.55}$$

(I) $\Sigma < \Sigma_d$

$$\Psi(\Sigma) := \frac{1}{\psi_1}\int_0^{\Sigma} \psi(\Sigma')d\Sigma'/\Sigma_{\rm mp} \tag{2.56}$$

$$= \frac{\psi_s}{\psi_1}\int_0^{\Sigma} (\Sigma'/\Sigma_{\rm mp})^{\delta_s} d\Sigma'/\Sigma_{\rm mp} \tag{2.57}$$

$$= \frac{\psi_s}{\psi_1(\delta_s+1)}\Big(\Sigma/\Sigma_{\rm mp}\Big)^{\delta_s+1} \tag{2.58}$$

Using Eq. 2.51,

$$\Psi(\Sigma) = \frac{1-f_d}{(\Sigma_d/\Sigma_{\rm mp})^{\delta_s+1}}\Big(\Sigma/\Sigma_{\rm mp}\Big)^{\delta_s+1} = (1-f_d)\Big(\Sigma/\Sigma_d\Big)^{\delta_s+1}. \tag{2.59}$$

(II) $\Sigma > \Sigma_d$

$$\Psi(\Sigma) := \frac{1}{\psi_1}\int_0^{\Sigma} \psi(\Sigma')d\Sigma'/\Sigma_{\rm mp} \tag{2.60}$$

$$= \frac{1}{\psi_1}\int_0^{\Sigma_d} \psi(\Sigma')d\Sigma'/\Sigma_{\rm mp} + \frac{1}{\psi_1}\int_{\Sigma_d}^{\Sigma} \psi(\Sigma')d\Sigma'/\Sigma_{\rm mp} \tag{2.61}$$

$$= \Psi(\Sigma_d) + \frac{\psi_d}{\psi_1}\int_{\Sigma_d}^{\Sigma} (\Sigma'/\Sigma_{\rm mp})^{\delta_d} d\Sigma'/\Sigma_{\rm mp} \tag{2.62}$$

$$= (1-f_d) + \frac{\psi_d}{\psi_1(\delta_d+1)}\Big[\Big(\Sigma/\Sigma_{\rm mp}\Big)^{\delta_d+1} - \Big(\Sigma_d/\Sigma_{\rm mp}\Big)^{\delta_d+1}\Big] \tag{2.63}$$

Using Eq. 2.51,

$$\Psi(\Sigma) = (1-f_d) + f_d\left[\frac{\Big(\Sigma/\Sigma_{\rm mp}\Big)^{\delta_d+1} - \Big(\Sigma_d/\Sigma_{\rm mp}\Big)^{\delta_d+1}}{1-(\Sigma_d/\Sigma_{\rm mp})^{\delta_d+1}}\right]. \tag{2.64}$$

For nuclear starburst disks, there are two energy sources: star-formation and viscosity. We assume that the matter is optically thick ($\tau > 1$) to the UV photons. Then, the flux from

star-formation F_* is related to the the star-formation rate $\dot{\Sigma}_*$ by (Thompson et al., 2005)

$$F_*(0) = \frac{1}{2}\epsilon\dot{\Sigma}_* c^2 = \sigma_{\rm SB} T_{\rm eff,*}^4 \text{ and } \psi_{1,*} = \dot{\Sigma}_* \tag{2.65}$$

and the flux from viscosity is given by (Thompson et al., 2005)

$$F_{\rm vis}(0) = \frac{3}{8\pi}\dot{M}\left(1 - \sqrt{R_{\rm in}/r}\right) = \sigma_{\rm SB} T_{\rm eff,vis}^4 \tag{2.66}$$

where $\dot{M}$ is the accretion rate and $R_{\rm in}$=3(2GM$_{\rm BH}$)/c^2. Since the radial and vertical structure are computed independently, one of the implicit assumption is that accretion occurs at mid-plane. Therefore, $F_{\rm vis}$ is taken to be produced at the mid-plane. There has been an empirical power-law relationship "Schmidt law" between $\dot{\Sigma}_*$ and the surface column density $\Sigma_{\rm mp}$ (Kennicutt, 1998),

$$\dot{\Sigma}_* \propto \left(\Sigma_{\rm mp}\right)^n. \tag{2.67}$$

Therefore, the power-law distribution of $\dot{\Sigma}_*$ is a good starting point.

2.4 Opacity

Modeling of radiation pressure dominated regions, such as NSDs, requires one to take into account the interaction between the radiation field and matter. This interaction can be quantified with a macroscopic quantity, opacity. A computation of opacity is not a trivial task since each chemical element interacts differently with a different frequency of light. Moreover, the inclusion of dust in the astrophysical composition increases the complexities due to the variability (e.g., size, shape, and distribution of grains) of dust opacity. However, for an optically thick medium (optical depth $\tau >> 1$), the opacity of a medium can be well treated as the Rosseland mean opacity (κ_R) (Hubeny & Mihalas, 2014) where the radiation pressure can be well described by the diffusion approximation (Hubeny & Mihalas, 2014).

Under the condition of LTE, κ_R depends on the composition of matter, its temperature T, and the number density n_H. For NSDs, we choose Orion abundances to compute opacity under LTE using CLOUDY (Ferland et al., 2013). CLOUDY is a one dimensional photo-ionization code which includes grain physics (Weingartner & Draine, 2001; van Hoof et al., 2004; Weingartner et al., 2006) with a realistic size distribution of various grain species (e.g. Mathis et al., 1977); for instance, the size and shape based absorption and scattering processes of grains. For NSDs, we explore a wide range of temperature T and density n_H:

$$10\text{K} \leq T \leq 10^{6.1}\text{K} \tag{2.68}$$

$$10^{-7}\text{cm}^{-3} \leq n_H \leq 10^{13}\text{cm}^{-3} \tag{2.69}$$

The curves in Fig. 2.1 show κ_R as a function of T for n_H of 10^3 cm^{-3} and 10^6 cm^{-3}. In low temperature regime, the κ_R is increasing with the temperature for a given n_H. This is expected since dust is the dominant source of opacity in this region and the dust cross-sectional area is proportional to the wavelength λ of incoming electromagnetic wave by $\lambda^{-\alpha}$, where α approaches to 2 in the Rayleigh limit (Pollack et al., 1985). (As temperature increases, the peak of radiation power shifts toward a lower λ). The κ_R has a small drop near 1400K (Kishimoto et al., 2013) due to the sublimation of silicate grains and the second deep drop occurs near 1750K (Kishimoto et al., 2013) due to the sublimation of graphite grains. The increase in κ_R after the deep drop is due to the H- scattering opacity then subsequently bound-free and free-free opacity. Hydrogen starts ionizing near 5000K, and further ionized by $\sim 80\%$ and $\sim 100\%$ near 10^4K and 1.5×10^4K, respectively. Using Saha's equation, one can show an ionization fraction decreases (higher bound-free opacity) with density. This is responsible for an overall decreased in κ_R with n_H in the intermediate temperature regime since hydrogen is the abundant element in the composition. After hydrogen is fully ionized, the opacity is fairly independent of density since Thompson

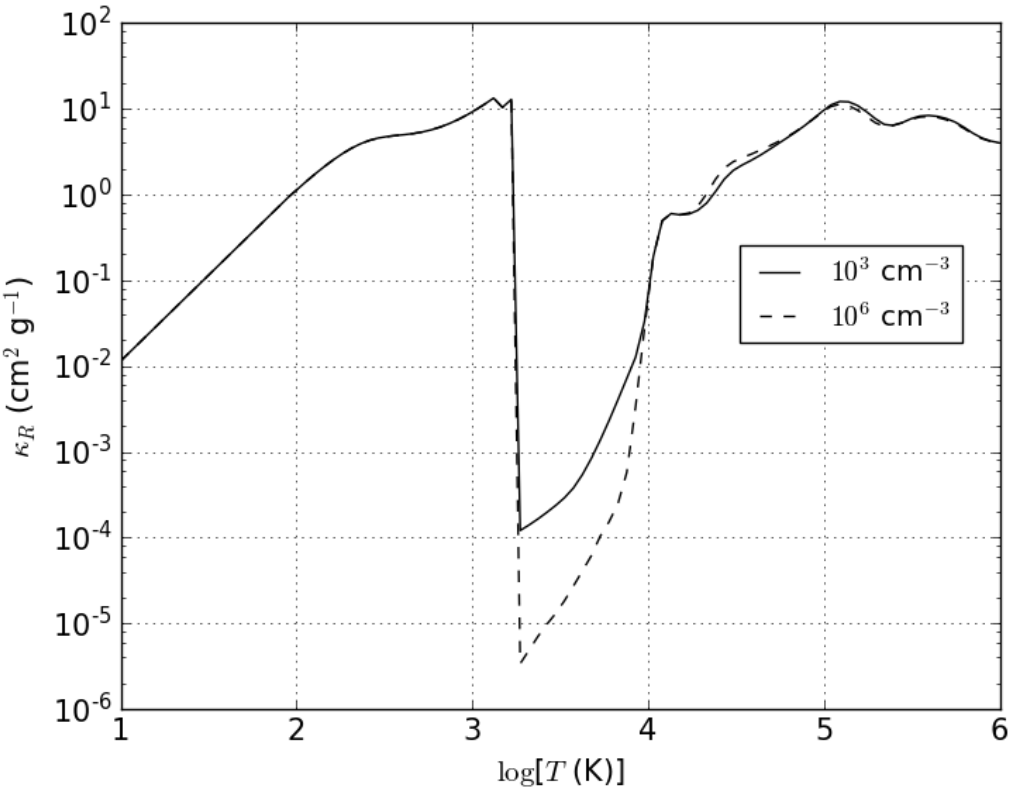

Figure 2.1: Rosseland mean opacity (κ_R) as a function of temperature. Solid and dashed lines represent for $\log[n_H(\text{cm}^{-3})] = 3$ and 6, respectively. In low-temperature region, the opacity is dominated by grains which drops near 1750K when graphite grains are destroyed. Due to the decrease in ionization factor with density, an overall opacity decreases as a function of density for a fixed temperature near $\log[T(\text{K})] = 3.5$. In high temperature limit, κ_R is dominated by the Thompson scattering, thus it becomes nearly independent of density.

Region	I	A	B	C	D
$\log(n_H)$	Independ.	[3.0,6.0]	[6.0,13.0]	[3.0,13.0]	[-7.0,3.0]
$\Delta \log(n_H)$	N/A	0.25	0.5	0.5	0.25
$\log(T)$	[1.0,3.0]	[3.0,4.1]	[3.0,4.1]	[4.1,6.1]	[3.0,6.1]

Table 2.1: 2D interpolation of n_H and T. The resolution among temperature points is taken to be 0.01 except for ranges of [3.13,3.26] and [3.243,3.2431] which has resolutions of 0.005 and 0.0001, respectively.

scattering becomes dominant. As temperature increases, gas absorbs more energy from incoming radiation which increases overall opacity of the medium.

Based on the complexities and behaviors of the Rosseland mean opacity as shown in Fig. 2.1, two dimensional space of density and temperature is divided among five regions to have an optimal algorithm for interpolation. The logarithmic grids and its resolution for each region are described in Table 1 and were chosen in a way to optimize a computational time and an accuracy of an interpolation algorithm. For region I, κ_R is an independent of density as seen in Fig. 2.1. Therefore, the κ_R of $\log(n_H)$ = 3.0 is taken for whole density range in interpolation function and only temperature grid points are interpolated.

2.4.1 Analysis

To check an accuracy of the interpolation algorithm, opacities from the algorithm were predicted for various temperature and density (off the grids) points and discrepancy against the real data from CLOUDY was computed as

$$\%\text{Error} := \frac{100 \times (\text{Predicted value-Actual value})}{\text{Actual value}}. \tag{2.70}$$

Some of the error analysis is illustrated in the Fig. 2.2.

The percentage error in regions I and C are less than 4%. For regions A and B, the spacing of grid points is not linear because of the deep dropped in the κ_R due to the sublimation

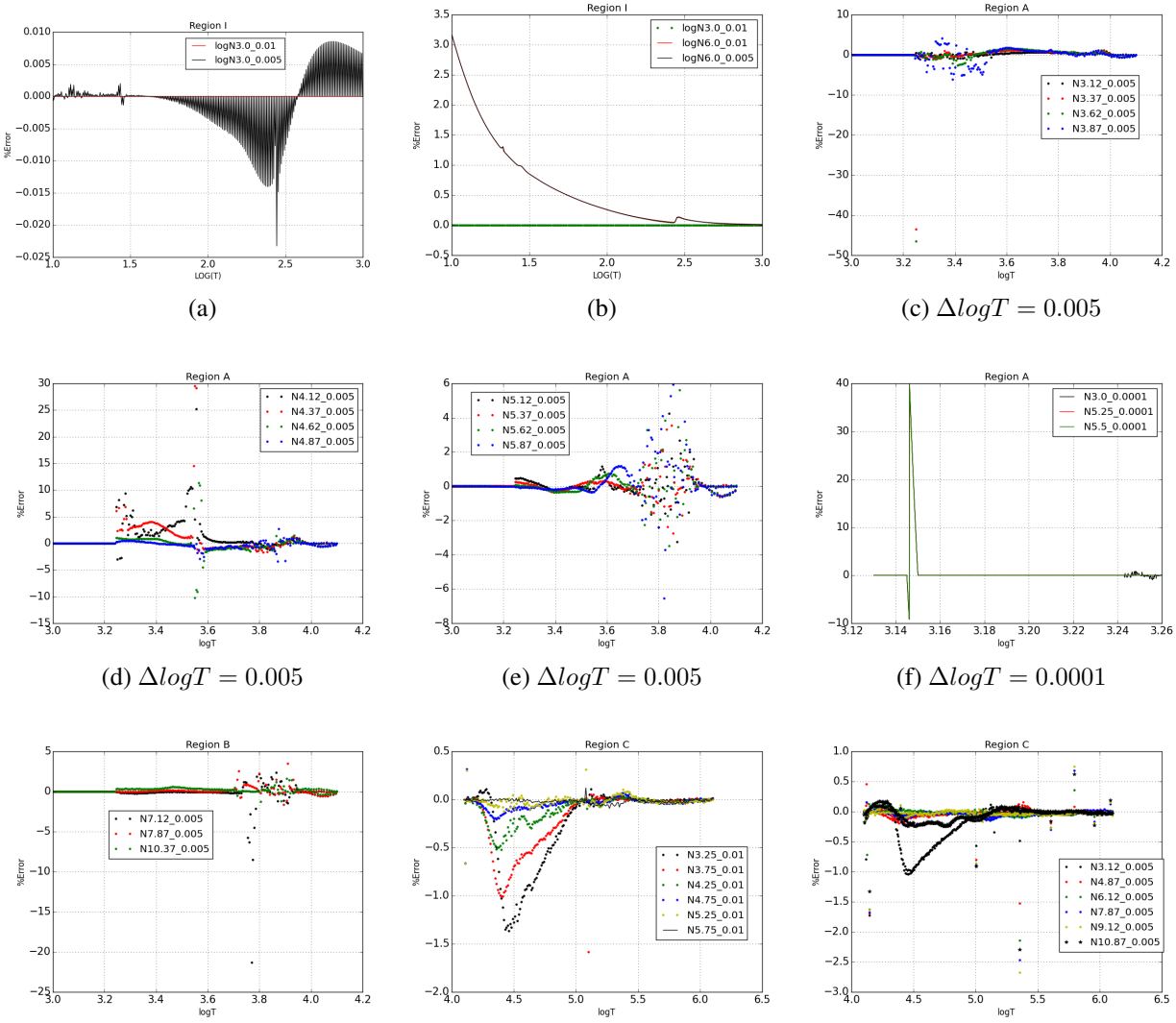

(a) (b) (c) $\Delta logT = 0.005$

(d) $\Delta logT = 0.005$ (e) $\Delta logT = 0.005$ (f) $\Delta logT = 0.0001$

(g) $\Delta logT = 0.005$ (h) $\Delta logT = 0.01$ (i) $\Delta logT = 0.005$

Figure 2.2: Representing the analysis on the accuracy of an interpolation algorithm. For regions I and C, uncertainty in predicted opacity is less than 4%. For regions A and B, error is less than $\sim 10\%$ except for certain $(\log(n_H), \log(T))$ sets, yet less than 50%.

of graphite grains. In region A, the interpolation function gives fairly well prediction. To minimize the percentage error in region B, various resolutions are chosen for subspaces. The percentage error is mostly less than 10% except, near $\sim$ 3.3K and 3.6K, where the error reaches to 50% and 30%, respectively. Region B shows less than 4% error except it can reach up to 25% near 3.8K. In summery, since an every vertical slab may have only $\sim$ 2-5 layers (in compare to total 400+ layers) at maximum with high uncertainty in opacity (yet less than 50%), it will not have a significant effect on the overall structure for the purpose of this project.

2.5 Test Case: Accretion Disk

Before making transition to the modeling of NSDs, we first model the structure of accretion disks and compare results against the work of (Hubeny & Hubeny, 1998). This ensures that the iterative algorithm and numerical method to solve non-linear boundary value problem are correctly implemented in the code. For simplicity, the opacity is considered to be the Thompson opacity (0.4 g cm^{-2}), which should be a good approximation for accretion disks since their temperature is well above 10^4K. The first step in the iterative method is to guess an initial solution. The initial solution is approximated as an "isothermal solution" where the scale height is determined by the isothermal approximation and, later, all other physical quantities are updated through iterations [6]. Afterward, the "isothermal solution" is updated by solving the second order hydrostatic equation (HSE). The HSE is the non-linear second order differential equation with a boundary value problem which is solved using the finite-difference method on the logarithmic grids. A previous solution is iterated until the convergence in temperature is achieved. To test the code, we first produce some of the results published in literature (e.g. Hubeny & Hubeny, 1998). The vertical distribution of viscosity is computed using a similar prescription mentioned in Hubeny & Hubeny (1998). As test models, we select 2, 11, and 20 pc from a central black hole with the mass $M_{\rm bh}$ of

[6] "Isothermal solution" is quoted because only a scale-height is affected by the isothermal approximation. Afterward, all other physical quantities are updated through iterations.

2×10^9 $M_\odot$ with the effective temperature of 80,000K, 27,000K, and 18,000K, respectively from Hubeny & Hubeny (1998). The computed various profiles such as density, height, and temperature are shown in Fig. 2.3.

The figure illustrates that the results are very similar to the work of Hubeny & Hubeny (1998) [7]. There is a small discrepancy, especially near the surface ($\tau \lesssim 1$), which were expected due to the following variance in our modeling in comparison with the work of Hubeny & Hubeny (1998): (i) we do not include general relativity correction which can be important for the very inner part of a disk, (ii) we consider only the electron scattering opacity 0.4 g cm^{-3}, whereas Hubeny & Hubeny (1998) includes hydrogen and helium. And, (iii) the RTE is solved under grey approximation, while the RTE solved in Hubeny & Hubeny (1998) has a dependence on frequency. The results are represented solely for the testing purpose of the code. For analysis of these results, a reader is referred to Hubeny & Hubeny (1998).

[7] A reader is referred to Hubeny & Hubeny (1998) to look at its results. Our Fig. 2.3a, b, c, d and e correspond to the figure 10b, 2 , 3, 1 and 10a in their's.

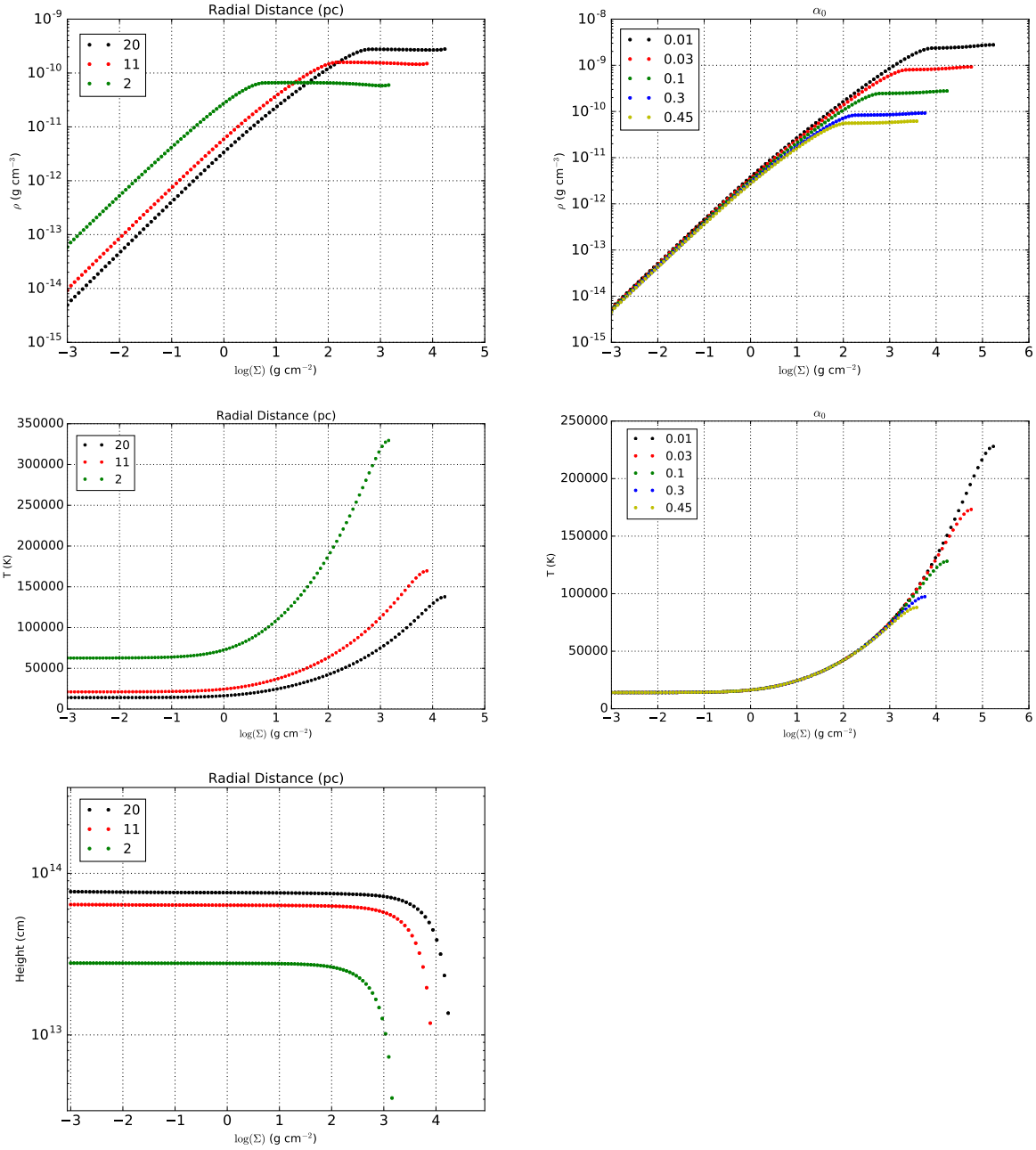

Figure 2.3: Some of the results dependent on a vertical structure for an accretion disk model chosen from Hubeny & Hubeny (1998) is represented to test our code. The figures show how density (top-panels), temperature (middle-panels), and height (bottom-panel) vary with the integrated mass column density (Σ). The right-panels show the black, red, green, blue, and yellow curves which represent model with the viscosity parameter α_0 equal to 0.01, 0.03, 0.1, 0.3, and 0.45, respectively. The left-panels show the black, red, and green curves which represent the vertical slabs at 20, 11, and 2 gravitational radii. The results are in fair agreement with the work of Hubeny & Hubeny (1998).

CHAPTER 3

MODELING THE VERTICAL STRUCTURE OF NUCLEAR STARBURST DISCS: A POSSIBLE SOURCE OF AGN OBSCURATION AT $Z \sim 1$

3.1 Introduction

Active galactic nuclei (AGNs) are extremely luminous regions, more than a billion times the solar luminosity, in galaxies. They emit energy across a large portion of the electromagnetic spectrum from radio waves to X-rays through accretion onto a supermassive black hole (Balbus, 2003). The majority of AGNs discovered in the thousands by *Chandra* and *XMM-Newton* show the presence of obscuration by dust and gas (Brandt & Hasinger, 2005; Gilli et al., 2007; Alexander & Hickox, 2012; LaMassa et al., 2017). Infrared (Thatte et al., 1997; Burtscher et al., 2013) and X-ray based observations (Elvis et al., 2004; Risaliti et al., 2005) point the location of this obscuration at the parsec scale. The simple unification scheme of AGNs suggests that all the variance in the obscuration are due to the difference in viewing angle (θ) of AGNs with respect to an observer, but they are intrinsically the same objects (Antonucci, 1993; Netzer, 2015). The mechanisms and physical conditions responsible behind this obscuration is still not well understood, but they seem to be dependent on AGN luminosity (Lawrence & Elvis, 2010) and, perhaps, redshift (Ballantyne et al., 2006b; Hasinger, 2008).

To explain the obscuration at the parsec scale, many possible mechanisms have been proposed. The detection of polarized broad lines in Seyfert 2 galaxies (e.g., Antonucci & Miller, 1985) led to the modeling of a simple uniform toroidal absorber (Krolik & Begelman, 1986, 1988; Pier & Krolik, 1992). In addition, many groups have proposed a geometrically thick torus supported by infrared (IR) radiation pressure (Krolik, 2007; Dorodnitsyn et al., 2011; Dorodnitsyn & Kallman, 2012; Chan & Krolik, 2016; Dorodnitsyn et al.,

2016). Another possible model is a torus with turbulence pressure due to supernovae or stellar winds (Wada & Tomisaka, 2005; Watabe & Umemura, 2005). Moreover, many authors have suggested a warped/tilted-disc to explain a range of obscuration (Nayakshin, 2005; Caproni et al., 2006; Lawrence & Elvis, 2010). In recent years, there has been some work done in modeling a clumpy torus (Hönig & Beckert, 2007; Nenkova et al., 2008; Hönig & Kishimoto, 2010) partly due to the observed column density variability seen in X-rays (Risaliti, 2002). Another possible source for the observed obscuration is nuclear starburst regions (Fabian et al., 1998; Wada & Norman, 2002; Thompson et al., 2005; Ballantyne, 2008; Hopkins et al., 2016). In this paper, we explore the effect of nuclear starburst discs (NSDs) on the AGN obscuration.

More than 50 years has passed since the discovery of the cosmic X-ray background (CXB) (Giacconi et al., 1962) and it is still not entirely resolved into discrete sources. The CXB is the spectral energy distribution (SED) which is characterized by a power law with the photon index of $\Gamma = 1.4$ in the 2-10 keV band and a peak in the $10 - 30$ keV band (Gruber et al., 1999). The SED up to a few keV energies can be explained by integrating point-like sources (Worsley et al., 2005) and many of these sources are observed to be AGNs (e.g., Mushotzky et al., 2000; Bauer et al., 2004). Understanding the distribution of column density along a line of sight $N_{\rm H}$ is an important aspect in modeling the CXB spectrum (Gilli et al., 2007) since the relative fraction of unobscured (Type 1, $N_{\rm H} < 10^{22}$ cm^{-2}), Compton-thin Type 2s (CN, 10^{22} cm^{-2} $\leq N_{\rm H} < 10^{24}$ cm^{-2}), and Compton-thick (CK, $N_H \geq 10^{24}$ cm^{-2}) AGNs determine the shape of the spectrum. (Variables which are frequently used in the paper are listed in Table 3.1.) In particular, the observed peak of the CXB spectrum requires a significant number of CK AGNs at moderate redshifts (Comastri et al., 1995; Gilli et al., 2001; Churazov et al., 2007; Moretti et al., 2009). Many studies have shown that 10% to 25% of CK AGNs are required in order to produce the observed peak of the CXB near 30 keV (Draper & Ballantyne, 2009; Akylas et al., 2012; Ueda et al., 2014). However, Akylas et al. (2012) shows that the fraction of CK AGNs ($f_{\rm CK}$) can range

Table 3.1: Description of symbols which are used frequently in the paper.

Symbol	Description
c	Speed of light
c_s	Total speed of sound
$f_{\rm CK}$	Fraction of Compton-thick AGNs
$f_{\rm CN}$	Fraction of Compton-thin AGNs
$f_{\rm g,out}$	Gas fraction at the outer radius
G	Gravitational constant
h	Surface scale-height
κ	Opacity
k_B	Boltzmann constant
m	Radial Mach number
$M_{\rm bh}$	A black hole mass
m_p	Mass of proton
$N_{\rm H}$	Column density along a line of sight
Ω	Keplerian angular frequency of a disc
$P_{\rm gas}$	Gas pressure
$P_{\rm rad}$	Radiation pressure
$P_{\rm turb}$	Turbulence pressure
P	Total pressure
Q	Toomre parameter
ρ	Density
R	Radial distance at $z = 0$
$R_{\rm cric}$	Distance where the largest inflation occurs in a disc
$R_{\rm out}$	Size of a disc
$\sigma_{\rm sb}$	Stefan-Boltzmann constant
Σ	Vertically mass integrated column density
$\Sigma_{\rm mp}$	Vertically mass integrated total column density to mid-plane
σ	Velocity dispersion
$\dot{\Sigma}_*$	Star-formation rate density
T	Temperature
τ	Optical depth
$T_{\rm eff}$	Effective temperature
θ	Viewing angle
$v_{\rm turb}$	Turbulence speed
z	Vertical height

from 5% to 50% due to the degeneracy of the input parameters in the modeling of the CXB spectrum. If NSDs are the potential source for producing the CXB peak, we can place a constraint on $f_{\rm CK}$ by modeling the 2D structure of NSDs.

Many reasons point toward NSDs as a potential source of obscuration. Young stellar populations are found in the inner regions of nearby AGNs (e.g., González Delgado et al., 2001; Gu et al., 2001; Cid Fernandes et al., 2004; Storchi-Bergmann et al., 2005; Ruschel-Dutra et al., 2017) including Seyfert galaxies (Davies et al., 2007). Davies et al. (2007) highlights a possible causality between star formation (SF) and AGN activity from studies of nine nearby Seyfert galaxies: the AGN activity occurs later in time separated by 50-200 Myrs from the peak of the SF rate. Such a causality suggests a possible fueling of gas toward a central black hole by stellar winds and supernovae (e.g., Vollmer et al., 2008; Hopkins, 2012), perhaps indicating a strong coupling of SF, stellar winds/supernovae, and the AGN activity. With a simple 1D model of NSDs, Thompson et al. (2005) shows a region near dust sublimation can inflate to $h \sim R$ which can obscure the incoming AGN irradiation. Such a mechanism can build a bridge among star-forming regions, AGN activity, and the obscuration. These reports provide further motivation to study NSDs in detail. Multi-dimensional modeling of NSD is important in order to resolve the dependency of $N_{\rm H}$ on the orientation angle θ of AGNs with respect to an observer.

In order to place a proper constraint on the column density $N_{\rm H}$ and the fractions of CN Type 2s ($f_{\rm CN}$) and CK AGNs, the vertical structure of NSDs is required. In the past, the hydrostatic structure of a disc has been computed for accretion discs using an iterative method (Hubeny, 1990). Using similar procedures as described by Hubeny (1990) and Hubeny & Hubeny (1998), we compute 2D structure of NSDs under various physical conditions. Later, we study the dependency of $N_{\rm H}$ on θ and also place a constraint on $f_{\rm CN}$ and $f_{\rm CK}$ using these models. These are outcomes of the NSD theory which can be used to test whether these discs can plausibly obscure and fuel Seyfert galaxies at $z \sim 1$. (Starburst discs may be a more prominent source for AGN obscuration when a large gas fraction is

available in galaxies (Ballantyne, 2008)-conditions that are more favorable at intermediate redshifts.)

Sect. 3.2 reviews the one-dimensional theory of NSDs. Sect. 3.4 describes the methodology of vertical structure. In Sect. 5.3, we provide and discuss the results including caveats and future work. Then, the paper is concluded in Sect. 3.5. Sect. 2.4 of Chapter 2 provides details on the opacity calculation used in the modeling.

3.2 A Brief Overview of Radial Structure

The one dimensional (radial structure) model of NSDs in the radiation dominated regime has been computed by Thompson et al. (2005) for ultra luminous infrared galaxies (ULIRGs). These models require four input parameters: size of the disc $R_{\rm out}$, the black hole mass $M_{\rm bh}$, the gas fraction at the outer radius $f_{\rm g,out}$, and the Mach number $m \equiv v_r/c_s$, where v_r is the radial velocity and c_s is the total speed of sound. The 1D model has a NSD rotating with the Keplerian frequency Ω around a central black hole with the mass of $M_{\rm bh}$. The Ω includes the potentials of the black hole and the bulge,

$$\Omega(R) = \Big(\frac{GM_{\rm bh}}{R^3} + \frac{2\sigma^2}{R^2}\Big)^{1/2}, \tag{3.1}$$

where G is the gravitational constant and R is the radial distance. The dispersion σ is computed using the $M_{\rm bh} - \sigma$ relationship (Ferrarese & Merritt, 2000; Gebhardt et al., 2000; Tremaine et al., 2002),

$$M_{\rm bh} = 2 \times 10^8 \left(\frac{\sigma}{200 \text{ km s}^{-1}}\right)^4 M_\odot. \tag{3.2}$$

The stability of a disc against gravitational collapse is always governed by Toomre's parameter Q. (The parameter Q is maintained to be 1 because there is an observational evidence in infrared ultraluminous galaxies (Downes & Solomon, 1998) and local spiral galaxies

(Martin & Kennicutt, 2001; Leroy et al., 2008; Westfall et al., 2014) including the Milky Way (Binney & Tremaine, 1987; Rafikov, 2001) for $Q \simeq 1$.) A gas fraction is injected at the outer radius of the disc which is driven towards the black hole at the constant Mach number through a presumed global torque (which can be due to a spiral instability or a bar; Goodman (2003)). The amount of available gas decreases with the radius as gas depletes into the formation of stars in order to maintain the Toomre stability criteria $Q = 1$. Then, the accretion rate ($\dot{M}$) and the SF rate ($\dot{M}_*$) are given by

$$\dot{M}(R) = \dot{M}_{\rm out} - \int_R^{R_{\rm out}} 2\pi R' \dot{\Sigma}_*(R') dR' \tag{3.3}$$

and

$$\dot{M}_*(R) = \pi R^2 \dot{\Sigma}_*(R), \tag{3.4}$$

where $\dot{\Sigma}_*$ is the SF rate density. The radiation pressure from this SF provides a vertical support for the dusty atmosphere against gravity. At some inner radius $R_{\rm in}$, the energy flux production from viscosity takes over the SF energy flux and the $R_{\rm in}$ is considered as a transition radius between a NSD and an accretion disc (AD).

In this 1D model, the vertical structure is not computed except the scale-height of a photosphere $h_{\rm ph}$ is approximated by scaling the mid-plane scale-height $h_{\rm mid}$ with the ratio of $\kappa_{\rm ph}$ and $\kappa_{\rm mid}$:

$$h_{\rm ph} \approx h_{\rm mid} \Big(\frac{\kappa_{\rm ph}}{\kappa_{\rm mid}} \Big), \tag{3.5}$$

where $\kappa_{\rm ph}$ and $\kappa_{\rm mid}$ are the opacities at the photosphere and mid-plane, respectively. $\kappa_{\rm ph}$ is computed by assuming that the temperature at the surface is the same as the effective temperature. With this theory, Thompson et al. (2005) showed that a large expansion of an atmosphere, $h_{\rm ph} \sim R$, is possible on parsec scales for certain conditions of ULIRGs.

Using the same theory, Ballantyne (2008) reaches similar conclusions for "Seyfert-like" conditions.

Here, we relax these assumptions and compute the exact vertical structure of NSDs by solving the coupled equations of hydrostatic balance, radiative transfer, and energy balance.

3.3 2D Structure

For time-independent conditions, radial and vertical structures are not possible to solve simultaneously due to a lack of prior knowledge on the distribution of any physical quantities. Therefore, the distributions of total energy flux and mass-integrated column density at the mid-plane ($\Sigma_{\rm mp}$) are computed using the Thompson et al. (2005) model. These distributions are used to compute the vertical structure at every annulus of radial distance. (This means the solutions of each annulus do not communicate with each other.) We assume discs are symmetric around the z-axis and $z = 0$ plane. The schematic of a NSD is shown in Fig. 3.1. The disk is divided logarithmically into a set number of annuli radially, then the each annulus (slab) is divided vertically into grid points on log-scale. NSDs have two energy sources: viscosity and SF. The energy transport is solely by the radiation in the vertical direction. In other words, the conduction and convection heat transports are excluded in modeling. The total radiation flux is parameterized by an effective temperature ($T_{\rm eff}$) since the energy is transported losslessly to the surface and then radiated away.

3.3.1 Vertical Structure of an Annulus

One can ask what is the vertical structure for a given column of gas with total energy flux at a radial distance R away from a central black hole of mass $M_{\rm bh}$. In order to obtain the hydrostatic solution for such a column of gas, the coupled one dimensional time independent radiative transfer equation (RTE), hydrostatic equation (HSE), and energy balance equation (EBE) must be solved.

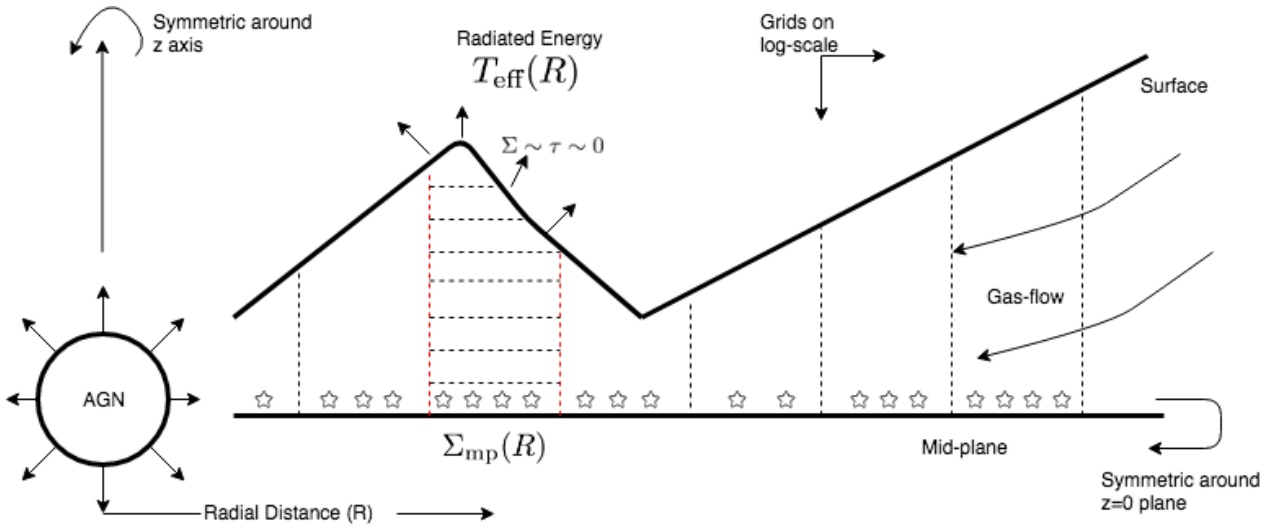

Figure 3.1: Schematic of 2D modeling: we need to model only a quadrant of a NSD due to the symmetry around $z = 0$ plane and $z-$axis. The disk is divided into a set number of annuli on log-scale and each slab (annulus) is divided further into a set of logarithmic grid points. Then, the goal is to compute the vertical structure by using the only information we have: total column density $\Sigma_{\rm mp}$ and energy content $T_{\rm eff}$.

The RTE governs the distribution of the radiation field within a material which is illustrated in Eq. 3.6 for a 1D slab:

$$\mu \frac{\delta I_\nu(z,\mu)}{\delta z} = \eta_\nu(z,\mu) - \chi_\nu(z,\mu) I_\nu(z,\mu). \tag{3.6}$$

Here, ν is the frequency of light, μ is the cosine angle, η_ν is the emissivity, and χ_ν is the extinction coefficient. To solve the RTE, we make the following approximations:

1. a homogeneous plane-parallel geometry (azimuthal symmetry) where properties of a material only depends on the z-direction, i.e. χ_ν is isotropic,

2. isotropic absorption and emission where a source function S_ν is independent of μ, $S_\nu(\mu, z) = S_\nu(z)$,

3. local thermodynamical equilibrium (LTE),

4. grey approximation (frequency integrated radiation field and opacity), and

5. the Eddington approximations: $f_k(\tau) \equiv \frac{K(\tau)}{J(\tau)}$ and $f_H(\tau = 0) \equiv \frac{H(\tau=0)}{J(\tau=0)}$ where J, H, and K are the first, second, and third angular moments of a radiation field.

Then, the temperature profile computed from the RTE for an energy source is given by

$$T^4(\tau) = \frac{3}{4} T_{\text{eff}}^4 \Big[\tau + q(\tau)\Big] \tag{3.7}$$

where $q(\tau)$ is the Hopf function[1] and T_{eff} is the total effective temperature. The optical depth τ is defined as

$$\tau(\Sigma) \equiv \int_{\Sigma_1}^{\Sigma} \kappa(\Sigma') d\Sigma' \tag{3.8}$$

where κ is the opacity and Σ_1 is the mass-integrated column density of the surface layer. For numerical convenience, Σ (which increases monotonically from the surface layer of a slab to its mid-plane) is chosen as the independent variable for all the equations. Then, the vertical distance of a layer from the mid-plane, scale-height z, is related to Σ with the following equation:

$$z(\Sigma) = \int_{\Sigma_{\text{mp}}}^{\Sigma} -\frac{1}{\rho(\Sigma')} d\Sigma', \tag{3.9}$$

where ρ is the density. Since a NSD has two energy sources, an overall temperature can be computed by adding the fluxes of all the sources, $F_{\text{tot}} = F_* + F_{\text{vis}}$, which results in

$$T = (T_*^4 + T_{\text{vis}}^4)^{1/4}. \tag{3.10}$$

[1]The form of $q(\tau)$ can be obtained from Eq. 3.8 in the paper by Hubeny (1990).

Here, T_* and $T_{\rm vis}$ are temperatures corresponding to the flux produced by viscosity and SF, respectively. Under LTE, κ depends on ρ, T,

$$\kappa = \kappa(\rho, T) \tag{3.11}$$

and the composition of the slab.

For the condition of hydrostatic balance, the second order differential form of the HSE,

$$\frac{d^2 P(\Sigma)}{d\Sigma^2} = -\frac{c_s^2(\Sigma)\Omega^2}{P(\Sigma)} - 4\pi G, \tag{3.12}$$

is used with the following boundary conditions[2]:

$$P_{\rm mp}(\Sigma_{\rm mp}) = P_{\rm mp} \ \text{ and } \ P_1(\Sigma_1) = P_1.$$

Here, P is the total pressure and Ω is the Keplerian frequency. P_1 is computed assuming a constant temperature for $\Sigma < \Sigma_1$ (Hubeny, 1990, section IV(b)). c_s is the total speed of sound and, in the case of local thermodynamical equilibrium (locally isothermal), it is defined as:

$$c_s^2(\Sigma) = \frac{P(\Sigma)}{\rho(\Sigma)}. \tag{3.13}$$

The HSE also includes an approximated self-gravity term (Paczynski, 1978) and it is solved in the logarithmic space in order to resolve the structure accurately near the surface. The solution of this boundary value problem can be achieved using the finite-difference method.

Finally, the EBE, Eq. 3.14, balances the total pressure with the gas pressure $P_{\rm gas}$, radi-

[2]Subscript '1' and 'mp' represent quantities at the surface and mid-plane, respectively.

ation pressure P_{rad}, and the turbulence pressure P_{turb}:

$$P(\Sigma) = P_{\text{gas}}(\Sigma) + P_{\text{rad}}(\Sigma) + P_{\text{turb}}(\Sigma). \tag{3.14}$$

The gas and radiation pressures are computed as

$$P_{\text{gas}}(\Sigma) = \frac{\rho(\Sigma) k_B T(\Sigma)}{m_p} \tag{3.15}$$

and

$$P_{\text{rad}}(\Sigma) = \frac{4\sigma_{\text{sb}}}{3c} T^4(\Sigma), \tag{3.16}$$

while P_{turb} is approximated (Thompson et al., 2005) as

$$P_{\text{turb}}(\Sigma) = 1.5 \times 10^8 \Big[\frac{E_0}{10^{51}}\Big]^{13/14} \Big[\frac{\rho(\Sigma)}{m_p}\Big]^{-1/4} \dot{\Sigma}_*(\Sigma) \tag{3.17}$$

$$= \frac{1}{2}\rho(\Sigma) {v_{\text{turb}}}^2, \tag{3.18}$$

where $E_0 = 10^{51}$ ergs is the energy released from a supernova. The turbulence speed v_{turb} is approximated to be a constant in the vertical direction using the density computed from the radial structure if $\dot{\Sigma}_*$ is only allowed to occur at the mid-plane. k_B, m_p, σ_{sb}, and c are the Boltzmann constant, mass of the proton, Stefan-Boltzmann constant, and the speed of light, respectively. We also require a column of gas to satisfy the Toomre stability criteria at the mid-plane which is parameterized by Q:

$$Q(\Sigma_{\text{mp}}) = \frac{c_s(\Sigma_{\text{mp}})\Omega}{2\pi G \Sigma_{\text{mp}}} = 1.0. \tag{3.19}$$

Since the only known information about these coupled equations are the boundary conditions, an iterative method is used to solve them.

3.3.2 Iterative Method

To solve the coupled equations described in the previous section, an iterative algorithm is developed which is non-trivial due to the difficulties in achieving convergence. However, the major iterative steps for constructing the 2D structure of a NSD are as follow:

1. Using the Thompson et al. (2005) model, compute the radial distribution of mass-integrated column density at the mid-plane $\Sigma_{\text{mp}}(R)$ and the effective temperature $T_{\text{eff}}(R)$.

2. Divide the radial distance (from R_{in} to R_{out}) into 50 annuli which are spaced logarithmically.

3. For a given annulus, we set 300 vertical logarithmic grid points in terms of Σ from the surface layer $\Sigma_1 = 10^{-3}$ g cm^{-2} to the mid-plane layer Σ_{mp}.

4. Compute the initial solution (isothermal profiles) for the energy source embedded only at the mid-plane using a similar procedure to the one described in section IV(a) of Hubeny (1990).

4.1. Assume $\kappa(\Sigma_1) = 1.0$ cm^2 g^{-1} and ρ_{mp} from the radial density profile. Using the analytical isothermal solution, compute z_1, τ_1, and T_1 in subsequent order. Compute κ_1 for a given ρ_1 and T_1 using the procedure described in Appen. A; thereafter, compute the remaining physical quantities (i.e., pressures and speed of sound).

4.2. Repeat step 4.1 for the rest of the layers to complete the initial vertical profiles. If there is any numerical issue in computing the initial solution, it can be fixed by changing ρ_{mp} or Σ_1. For example, the Σ_1 may be adjusted for a low density environment.

5. Update the pressure by solving Eq. 3.12, where P_{mp}, P_1, and c_s are used from a previous iteration.

6. Using the updated pressure (or the speed of sound), re-compute $\rho(\Sigma)$, $\kappa(\Sigma)$, $\tau(\Sigma)$, and $T(\Sigma)$ in subsequent order.

7. Since, the RTE and HSE are not solved simultaneously, the pressure computed from the HSE does not necessarily match with the EBE which induces a discrepancy in pressure, $\delta P_{\rm E}$. If Eq. 3.13 is not consistent with the HSE, it causes another discrepancy in pressure, $\delta P_{\rm c}$. To reduce $\delta P_{\rm E}$ and $\delta P_{\rm c}$, iterate the previous solution by updating c_s using the induced $\delta P_{\rm E}$ as follows,

$$c_s \rightarrow c_s + \delta c_s \;\; \text{where} \;\; \delta c_s = \frac{1}{2}\frac{\delta P_{\rm E}}{c_s \rho}. \tag{3.20}$$

   Once $\delta P_{\rm E}$ and $\delta P_{\rm c}$ reach their minimum values, move to the next step.

8. If $\delta P_{\rm E}$ and $\delta P_{\rm c}$ are within the set discrepancy of 0.05, skip this step. Otherwise, go back to the step 5.

9. So far the achieved solution does not necessary satisfy the Toomre criteria ($Q = 1$). To maintain this condition at the mid-plane, repeat steps 4-8, but change $P_{\rm mp}$ while solving the HSE. $P_{\rm mp}$ corresponding to Q =1 can be found using the Newton-Raphson method[3]. Finally, the self-consistent profiles are computed for a given annulus.

10. Repeat steps 1 to 9 for all the radii of a disc to construct the 2D profiles where θ is the viewing angle measured from the $z = 0$ plane.

The major steps of the iterative scheme is also illustrated in Fig. 3.2. Using this developed numerical scheme, we explore NSDs under various conditions (input parameter space) that are shown in Table 3.2. The Mach number m is chosen on the order of a tenth because the gas is not accreted to a parsec scale for a very low m since all the gas is converted into stars in the outer region of the disc and the high Mach number (close to unity or

[3] $P_{\rm mp} = 0.9 P_{\rm rad}$ from the initial solution is a good initial guess for the Newton-Raphson method where $P_{\rm rad}$ is the radiation pressure at the mid-plane.

Table 3.2: We list all the bins in the domain of each input parameter ($M_{\rm bh}$, $R_{\rm out}$, $f_{\rm g,out}$, m). After taking all the possible combination of these bins, a total of 192 models are computed. The Mach number m is chosen such that gas can accrete to the parsec scale and the other parameters represent a possible range of physical conditions for NSDs.

$\log(M_{\rm bh}/M_{\odot})$	$R_{\rm out}$(pc)	$f_{\rm g,out}$	m
6.5	240	0.2	0.1
7.0	180	0.4	0.3
7.5	120	0.6	0.5
8.0	60	0.8	–

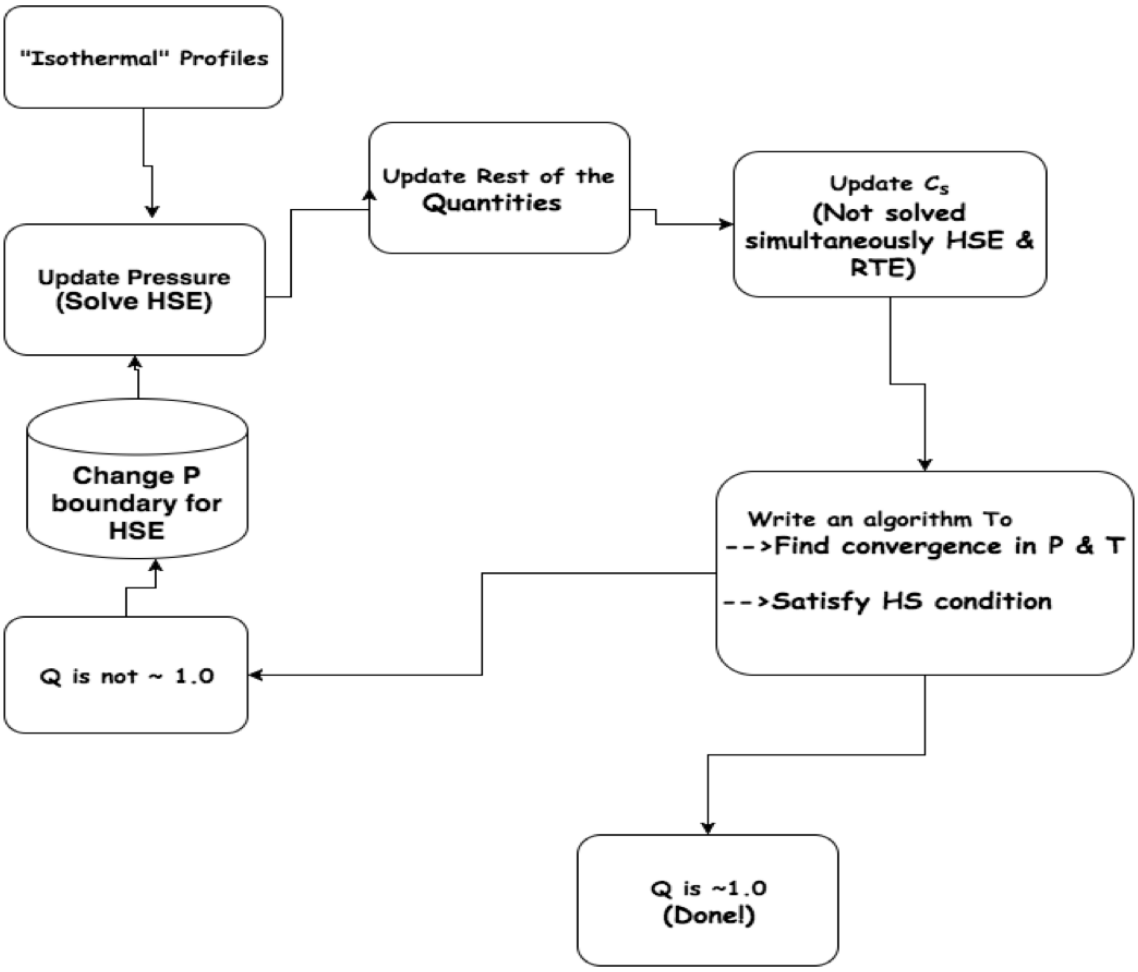

Figure 3.2: Diagram representing the main iterative steps: the idea is to start with some initial approximated,"isothermal", solution, then updated pressure by solving the HSE. With the updated pressure, the rest of the physical quantities are updated. Since the RTE and HSE are not coupled, there will be a discrepancy in pressure. After achieving the convergence in pressure, the final step is to satisfied the stability criteria.

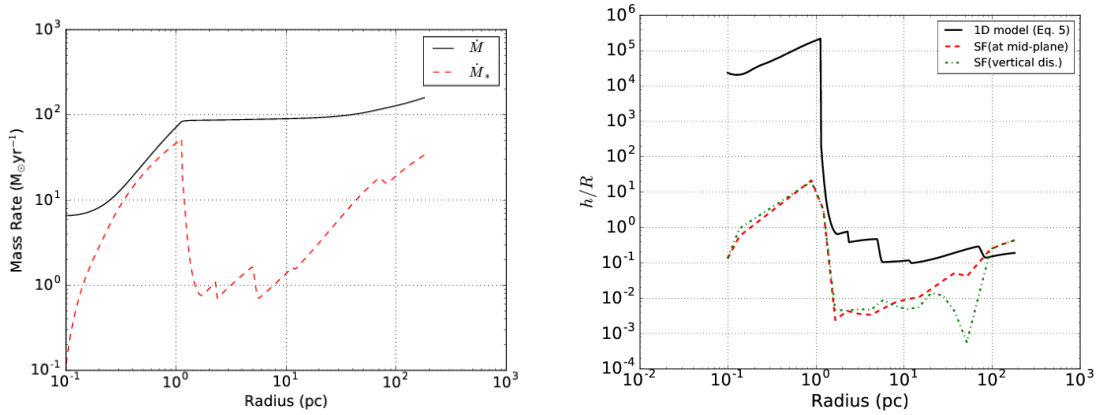

Figure 3.3: A few important quantities as a function of R for Model A, ($M_{\rm bh}$, $R_{\rm out}$,$f_{\rm g,out}$, m)=($10^{7.5}$ $M_\odot$,180.0 pc, 0.8, 0.5). *Left:* The figure shows that the gas is depleted into stars as it accretes toward the black hole in order to achieve the Toomre stability criteria, $Q = 1.0$. When the dusty gas reaches $1750K$, graphite grains are destroyed causing a large starburst. This occurs at the critical radius 0.884 pc in order to support the vertical atmosphere by radiation pressure. *Right:* Here, the scale-height h/R computed from the 1D approximation (Eq. 3.5) and the explicit 2D calculation are shown. The dashed-red curve represents the model with SF occurring at the mid-plane and the dashed-dotted-green curve is the model with the vertical distribution of SF (Sect. 3.4.5). In comparison to an approximated scale-height, the explicit calculation predicts a lower expansion, except at the outer part of the disc. However, near the critical radius, a larger opacity gradient due to the dust sublimation inflates the atmosphere where $h > R$ is achieved.

higher) requires an inclusion of additional physics (i.e., shock waves). The size of the disc, the gas fraction at the outer radius, and the mass of the black hole are chosen such that they cover a reasonable physical range of NSDs. Taking all the possible combination of these four input parameters, we compute in total 192 models.

3.4 Results & Discussion

Out of 192 models, 99 discs show a large expansion of an atmosphere (comparable to R or even higher) on parsec/sub-parsec scale. Here, we present the explicit profiles for one of these discs (hereafter Model A) as an example and its vertical profiles at the critical radius $R_{\rm cric}$ (where the largest expansion occurs). Later, we compute a distribution of $N_{\rm H}$ based on a random selection from sets of θ and 192 models.

3.4.1 Model A

Model A is the nuclear starburst disc whose $f_{\rm g,out}$, $R_{\rm out}$, m, and $M_{\rm bh}$ are set to 80%, 180 pc, 0.5, and $10^{7.5} M_{\odot}$, respectively. As gas accretes toward the black hole, the gas is depleted into star-formation in order to maintain the stability criteria (Fig. 3.3 (left)). In addition, each column of gas becomes denser as gas gets closer to the black hole due to an increase in the vertical gravitational component. This increase in Σ enhances the optical depth. As the gas becomes more optically thick, its temperature rises since T is directly related to τ (which is the consequence of the RTE solution). When the gas crosses the dust sublimation temperature which are 1400K and 1750K for silicate and graphite grains, respectively (Kishimoto et al., 2013), starbursts occur near $\sim$4.0 pc and $\sim$0.884 pc as shown in Fig. 3.3 (left). The loss of the dust opacity induces a large opacity gradient. This opacity gradient causes a large expansion of the atmosphere which is illustrated in the right panel of Fig. 3.3. This atmosphere is supported by radiation pressure from starbursts (Fig. 3.3 (left)). The right panel of Fig. 3.3 compares the approximated surface scale-height (Eq. 3.5) from the Thompson et al. (2005) model to the explicit calculation. The dashed-red curve assumes that SF occurs at the mid-plane, while the dashed-dotted-green curve represents the model with a vertical distribution of SF (which is discussed further in detail in Sect. 3.4.5). The exact calculation predicts a lower scale-height ($\approx$ 4 orders of magnitude lower at $R_{\rm cric} = 0.884$ pc) than the simple approximation except at the outer part of the disc. This discrepancy is due to the inaccuracy in assumptions made under Eq. 3.5: (1) the surface temperature is the same as $T_{\rm eff}$, (2) a constant $\kappa_{\rm mid}$ from $z = 0$ to $h_{\rm mid}$, and (3) κ increases linearly with z. The expansion of the atmosphere at $R_{\rm cric}$ is larger than the radial distance by a factor of 21.5 and covers 97% of the sky (observed from the central black hole).

Fig. 3.4 shows several important vertical profiles of a slab at $R_{\rm cric} = 0.884$ pc for model A. As Σ increases from the surface layer ($\Sigma = 10^{-2}$ g cm^{-2}) to the mid-plane ($\Sigma_{\rm mp}$), density and temperature also increase to achieve hydrostatic balance except when dust sublimates

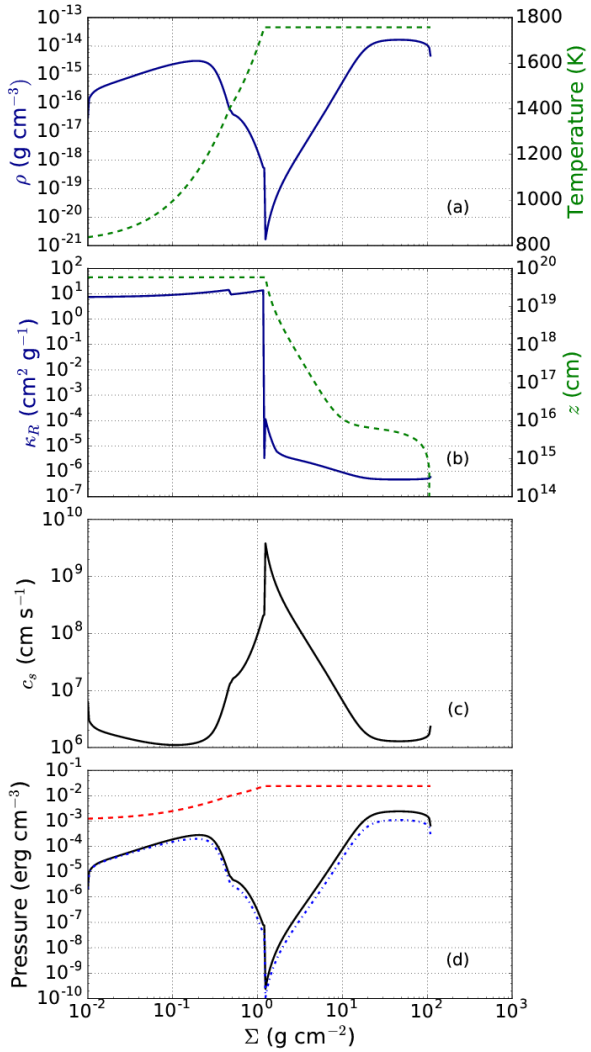

Figure 3.4: A few important vertical profiles as a function of Σ at $R_{\rm cric} = 0.884$ pc for Model A, ($M_{\rm bh}$,$R_{\rm out}$,$f_{\rm g,out}$, m)=($10^{7.5}\ M_{\odot}$,180.0 pc, 0.8, 0.5). ρ (solid-blue) and T (dashed-green) increase with Σ to achieve the hydrostatic balance as shown in panel (a). Panel (b) shows that when grains sublimate near $\Sigma \approx 1.0\,{\rm g\,cm^{-2}}$, the dust opacity is lost (solid-blue) causing a drop in ρ (solid-blue line in panel (a)). This increases c_s as shown in the panel (c) which results in the inflation of the surface scale-height (dashed-green line in panel (b)). The solid-black, dashed-red, and dashed-dotted-blue curves in the bottom panel represent $P_{\rm gas}$, $P_{\rm rad}$ and $P_{\rm turb}$, respectively. The panel (d) shows that the atmosphere is radiation pressure dominated. A density inversion is developed at the surface; however, it has a negligible effect on the overall h since the inverted column of gas contains less than 1% of the total column density $\Sigma_{\rm mp}$. A very small density inversion near the mid-plane (panel a) is introduced due the boundary condition of NSDs (input of large energy flux at the mid-plane) and this, in return, causes the inversion of $P_{\rm gas}$ which is shown in the panel (d).

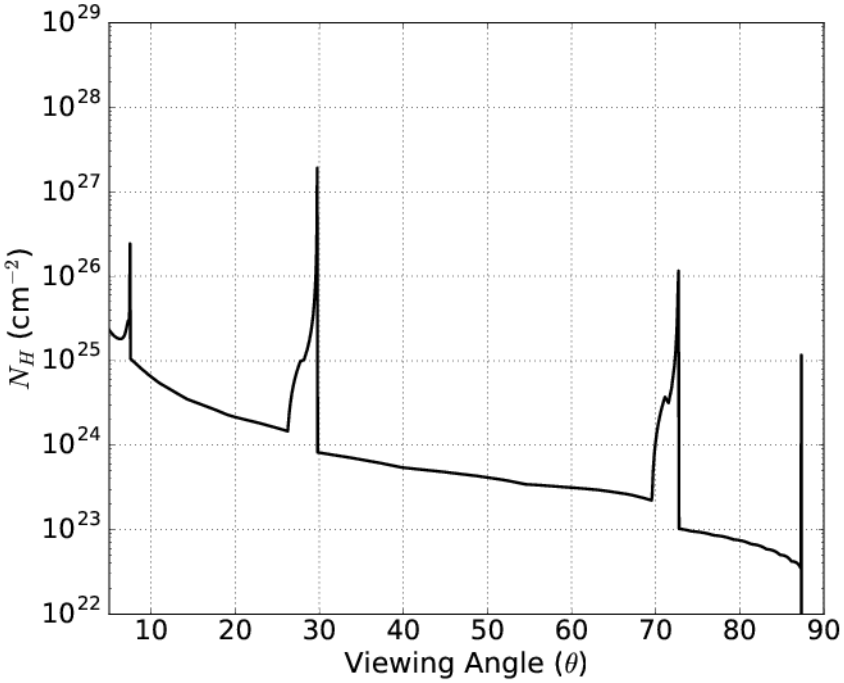

Figure 3.5: The dependence of $N_{\rm H}$ as a function of viewing angle θ for Model A whose radial and vertical profiles are shown in Fig. 3.3 and Fig. 3.4, respectively. Any central AGN would appear to be CN or CK based on the orientation of the AGN-NSD system with respect to an observer. The three peaks in $N_{\rm H}$ are due to the density inversion phenomenon which are observed in slabs at $R_{\rm cric}$ and beyond.

near $\Sigma = 1.0\,{\rm g\,cm^{-2}}$ which is shown in Fig. 3.4 (a). The sublimation of grains results in the immediate drop in the opacity (solid-blue line in Fig. 3.4 (b)). This opacity gradient increases the total speed of sound (Fig. 3.4 (c)) which, in turn, expands the dusty atmosphere (dashed-green line in Fig. 3.4 (b)). Panel (d) shows that radiation pressure (dashed-red curve) dominates throughout the slab over the gas pressure (solid-black curve) and the turbulence pressure (dashed-dotted-blue curve). In such slabs, the density inversion is expected locally since grains are sublimated; however, its effect on the overall scale-height h is insignificant since only a small fraction ($< 1\%$) of $\Sigma_{\rm mp}$ is inverted. In addition, the gas pressure curve in panel (d) shows a slight inversion near the mid-plane. This is due to another density inversion caused by the boundary condition of our systems (outburst of energy flux at the mid-plane).

Once the 2D profiles of a disc is calculated successfully, a subsequent task is to compute the column density along a line of sight $N_{\rm H}$ which is given by

$$N_H \approx \int_{R_{\rm in}}^{R_{\rm out}} \rho(\theta, R) \cos^{-1}(\theta) dR/m_p. \tag{3.21}$$

For model A, the distribution of $N_{\rm H}$ as a function of θ is shown in Fig. 3.5 and shows that $N_{\rm H}$ decreases with θ. The peaks in $N_{\rm H}$ are due to the density inversion phenomenon which occurs in slabs where dust is sublimated (Fig. 3.4a). The relative size of these peaks trace the offset of the large opacity gradient among these slabs. The figure illustrates that $N_{\rm H}$ appears to be CK for $\theta \lesssim 30°$and also near θ where the peaks occur ($\approx$72°and 87°). For any other θ between $\approx$ 30°and $\theta_{\rm max} = 87.3$, a central AGN is obscured by the CN medium. For $\theta >$87.3°, the central AGN appears to be Type 1. A NSD therefore is consistent with the simple AGN unification model where the line-of-sight into the nucleus determines the observed obscuration properties. Although Model A would imply a Type 2/Type 1 ratio of $\sim$7:1, far higher than the observed ratio $\sim$4:1 (Gilli et al., 2007)), depending on the physical conditions $\theta_{\rm max}$ can be as low as 40°, giving a Type 2 to Type 1 ratio of 0.7. The distribution of the obscured to unobscured sky covering factors of all 99 NSD models with an inflationary atmosphere at parsec scale is shown in Fig. 3.6. The sky covering factor is defined as:

$$\text{Covering Factor} := \frac{\arctan(z/R)[\text{Degrees}]}{90°} \times 100\%.$$

The plot shows that, while large ratios are more common in our parameter space, Type 2/Type 1 ratios in line with the observations are found in 31% of the models. These are the models whose h/R at the critical radius is less than 2 and their physical conditions are scattered across the input parameter space. Therefore, the fraction of sky obscured by the NSD can vary significantly from galaxy to galaxy.

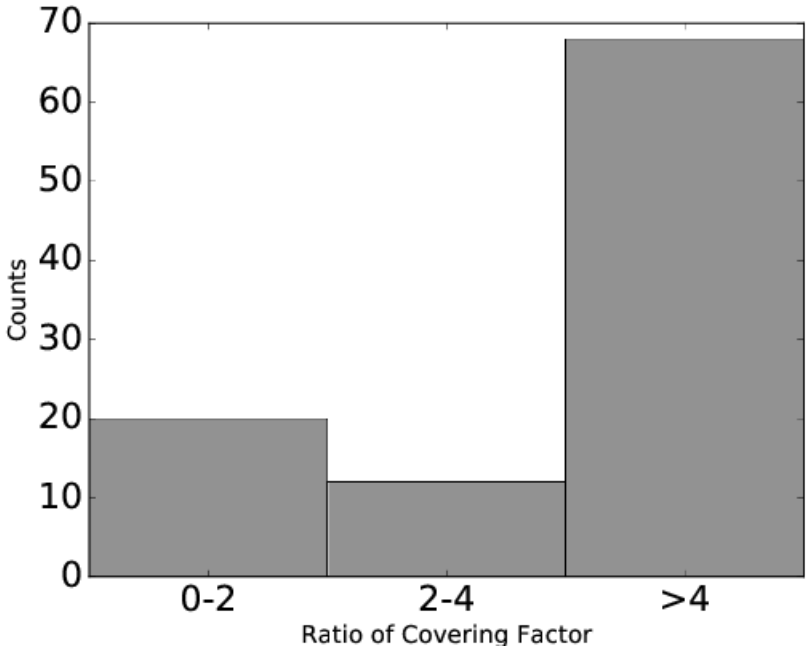

Figure 3.6: The distribution of the ratio of sky covered by $N_H > 10^{22}$ cm^{-2} gas to that covered by $N_{\rm H} < 10^{22}$ cm^{-2} gas (i.e., the potential AGN Type 2/Type 1 ratio) for the 99 NSD models that produced a parsec-scale starburst. About 31% of models (which can vary across the input parameter space) predict covering factors in agreement with the observed ratio. Depending on individual conditions, the fraction of sky covered by a NSD can vary greatly from galaxy to galaxy.

Table 3.3: A total 99 models out of 192 show the starburst phenomenon causing the large atmosphere expansion at the parsec scale. Here, we show a distribution of these models across the input parameter space. This shows that a smaller disc size, a larger gas fraction and Mach number are in favor of a burst of star-formation.

	$\log(M_{\rm bh}/M_\odot)$	6.5	7.0	7.5	8.0	Total (99)
$R_{\rm out}$(pc)	60	7	6	9	10	32
	120	5	6	6	8	25
	180	5	4	6	6	21
	240	5	5	5	6	21
$f_{\rm g,out}$	0.2	0	0	1	3	4
	0.4	5	6	7	8	26
	0.6	8	8	9	9	34
	0.8	9	7	9	10	35
m	0.1	1	1	2	3	7
	0.3	9	10	11	13	43
	0.5	12	10	13	14	49

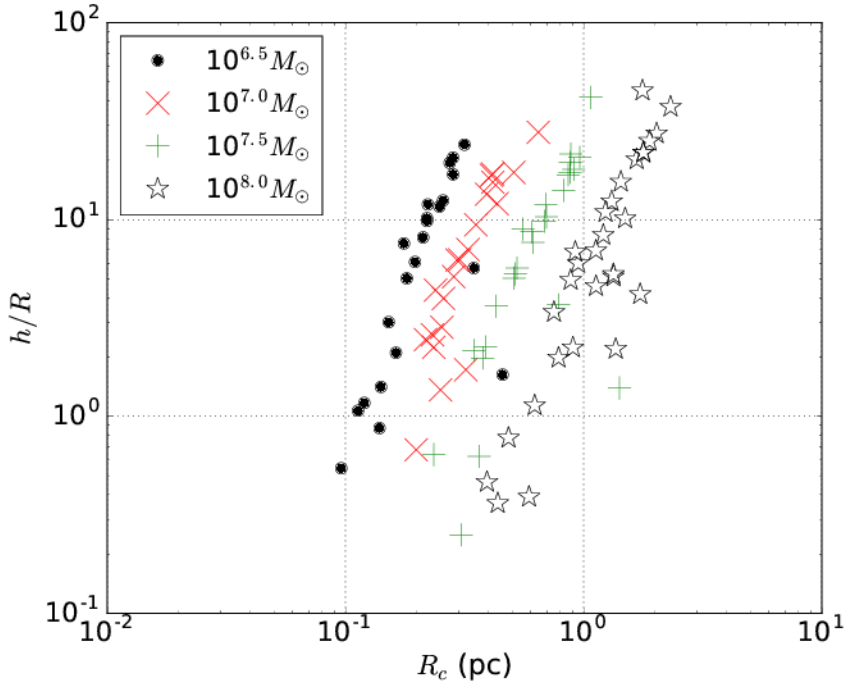

Figure 3.7: The figure shows h/R inflated due to the dust sublimation at critical radii dependent on $M_{\rm bh}$. For a higher $M_{\rm bh}$, an expansion occurs earlier due to a relatively stronger vertical gravitational component. This is also the reason why h/R decreases closer to the black hole for a fixed $M_{\rm bh}$.

3.4.2 All Models: scale-height h

A total of 99 out of 192 models (52%) show the inflation of an atmosphere at a critical radius which is illustrated in Fig. 3.7. It shows the dependency of h/R on the black hole mass and the critical radius. The black, red, green and white data points at the parsec scale show that the critical radius gets closer to a black hole as $M_{\rm bh}$ decreases. This is expected since the gas has to accrete more inward in order to reach to the dust sublimation temperature for the lower $M_{\rm bh}$. Depending on the physical conditions, h/R at the sub-parsec scale can range on the order of few tenths to tens. These large expanded vertical structure can obscure the incoming AGN light. Especially, since these atmospheres are dusty, the UV/optical photons will be reprocessed into IR photons. For a given black hole mass, the $R_{\rm cric}$ increases as a function of $f_{\rm g,out}$ since the optical depth reaches the sublimation temperature quicker due to the availability of gas. The amount of expansion at these critical radii are mainly governed by the magnitude of starbursts occurring at the mid-plane. Table 3.3 shows the distribution of 99 models across the input parameter space. In order to acquire an expanded atmosphere at the parsec scale, a smaller size disc, larger gas fraction, and higher Mach number are favorable conditions which is in the agreement with the work of Ballantyne (2008).

3.4.3 $N_{\rm H}$ Distribution

To estimate the distribution of the column density observed along a line of sight ($N_{\rm H}$) from a large sample of NSDs, the domain of the viewing angle $\theta \in$ [0°,90°] is divided into 30 bins. Afterward, the distribution of $N_{\rm H}$ is computed by randomly selecting $N_{\rm H}$ 10,000 times from the sets of 192 models and 30 bins of θ. The top panel of Fig. 3.8 shows the histogram of the $N_{\rm H}$ fraction in a given bin. Based on the random selection, the fraction of Type 1, CN Type 2s, and CK are 0.56, 0.23, and 0.21, respectively. For obscured AGNs, the fraction of AGNs peaks near $\log[N_H(\mathrm{cm}^{-2})] \approx 23.5$. The bottom panel of Fig. 3.8 represents the scattering of θ for obscured AGNs when they are observed randomly. The

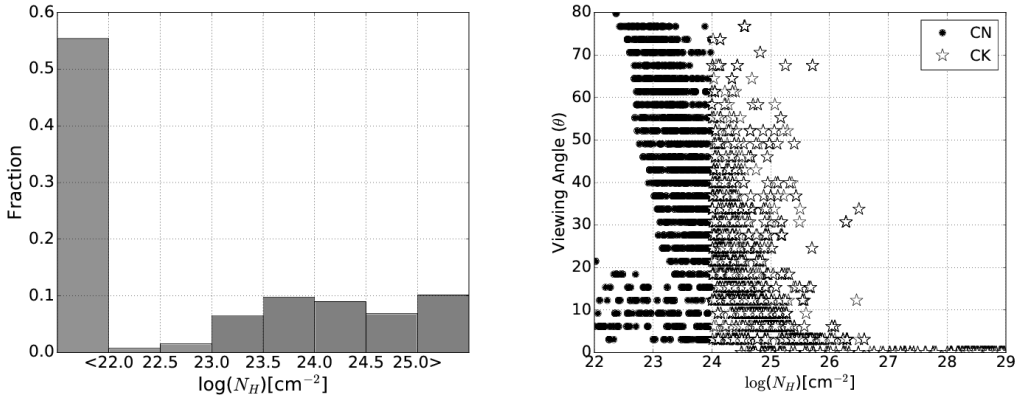

Figure 3.8: *Top:* A histogram of the AGN fraction as a function of $N_{\rm H}$ based on a random selection. The fraction of Type 1, CN Type 2s, and CK AGNs are 0.56, 0.23, and 0.21, respectively. The distribution of heavily obscured AGNs peaks near $\log[N_H(\text{cm}^{-2})] = 23.5$. *Bottom:* Scatter plot of CN and CK AGNs illustrating the dependency of $N_{\rm H}$ on the orientation of NSD-AGN systems based on the random selection. Due to the degeneracy in the input parameter space, the NSD-AGN systems for a given $N_{\rm H}$ spans almost an entire domain of θ for CK and heavily obscured CN AGNs. The gas dominated models do not show the large expansion ($\theta \lesssim 20^{\circ}$) which are presented by data points near $\log[N_H(\text{cm}^{-2})]$=22.5.

solid data points correspond to CN AGNs and the starred ones are for CK AGNs. The data points with $\theta \lesssim 20^{\circ}$ near $N_{\rm H}$=$10^{22.5}$ cm^{-2} are gas dominated NSDs where starbursts did not occur. All the models appeared to be CK when they are viewed edge-on. This is expected since dense gas occupies the mid-plane regions of the discs. The figure illustrates that a given $N_{\rm H}$ of CK or a heavily obscured CN AGN spans almost the entire domain of θ (from 0° to $\approx 80^{\circ}$) dependent on physical conditions. That means that, under certain conditions, the AGNs can be obscured by near face-on CK dusty gas.

The 2D NSD theory predicts $f_{\rm CN}$ and $f_{\rm CK}$ to be 23% and 21%, respectively, which is shown in the top panel of Fig. 3.8. This is in reasonable agreement with the values mentioned in the literature. For instance, the modeling of CXB suggests that $f_{\rm CK}$ can range from 5% to 50% (Akylas et al., 2012). Brightman & Ueda (2012) found $f_{\rm CK} \approx 0.25$ around redshift 1 by studying the sample of *Chandra Deep Field South* survey. In the local universe, $f_{\rm CK}$ is $\approx 20\%$ based on the hard X-ray (Burlon et al., 2011), the optical (Akylas & Georgantopoulos, 2009), and IR (Brightman & Nandra, 2011a,b) samples. Ueda et al.

(2014) constraints the ratio of CK to CN AGNs to be $\approx 0.5-1.6$ in order to produce the 20-50 keV part of the CXB spectrum which is in the agreement with the prediction of the NSD theory, 0.9. The outcomes of our work is in good agreement with observations and suggests that NSDs could be potential sources of AGN obscuration at intermediate redshifts.

3.4.4 Inversion Phenomena

Many of our hydrostatic models of NSDs show a density inversion phenomenon. For example, the phenomenon is observed in model A whose vertical profiles at $R_{\rm cric}$ are shown in Fig. 3.4. There are two causes for the density inversion: (1) sublimation of grains and (2) demand of efficient energy flux transport. The latter case has been widely studied by theorists (Chitre & Shaviv, 1967; Joss et al., 1973; Schwarzschild, 1975; Tuchman et al., 1978; Harpaz, 1984). This inversion phenomenon can lead to a possible Rayleigh-Taylor instability (RTI). The development of RTI in radiation pressure dominated dusty environment has been also observed in hydrodynamical numerical simulations (e.g., Krumholz & Thompson, 2012; Davis et al., 2014). We expect the density inversion due to the sublimation of grains to have an insignificant effect on $N_{\rm H}$ distributions (thus also $f_{\rm CN}$ and $f_{\rm CK}$) since the inverted column density of gas is a small fraction ($< 1\%$) of the total column density.

The density inversion in gas pressure and turbulence pressure dominated layers causes a local pressure inversion. The development of a pressure inversion is expected in thermally unstable regions when temperature is monotonically increasing with τ (e.g., Rozanska & Czerny, 1996). Such a development of inverted pressure has been already reported in the modeling of astrophysical atmospheres in the past (Achmad et al., 1997; Asplund, 1998; Helling & Winters, 2001; Różańska et al., 2002). In order to analyze the effect of the inverted gas on a NSD, a time-dependent calculation becomes necessary which is beyond the scope of this paper. However, our comprehensive conclusion that NSDs are plausible sources for AGN obscuration is still absolute since the loss of dust opacity can cause an

inflation to a parsec/sub-parsec atmosphere by orders of magnitude which is shown in the panel (b) of Fig. 3.4.

3.4.5 Vertical Distribution of $\dot{\Sigma}_*$

Star-formation (SF) does not necessarily have to occur only at the mid-plane. Therefore, it would be interesting to study how the vertical distribution of SF affects the scale-height h and $N_{\rm H}$ distribution of NSDs. The Kennicutt-Schmidt law (which is also called the star-formation law) relates star-formation rate density $\dot{\Sigma}_*$ to the surface gas density $\Sigma_{\rm gas}$ by $\Sigma_{\rm gas} \propto \dot{\Sigma}_*^{\alpha}$ (Schmidt, 1959; Kennicutt, 1998; Kennicutt & Evans, 2012), where α is expected to be ≈ 1 for radiation pressure dominated regions (Ballantyne et al., 2013). Hence, we model the linear vertical distribution of $\dot{\Sigma}_*$ on Σ using the prescription presented by Hubeny & Hubeny (1998). Implementation of the vertical distribution assumes: (1) a surface scale-height at $\tau = 1$ and (2) $\tau_{\rm mp} > 1.0$ (For optically thin column of gas, SF is only allowed to occur at the mid-plane.). With this description, we present the result for model A with the vertical distribution of $\dot{\Sigma}_*$ (hereafter, model $\bar{\rm A}$).

Fig. 3.3 (dashed-dotted-green line) shows the radial distribution of the surface scale-height $\bar{h}$ (for model $\bar{\rm A}$) and Fig. 3.9 plots the ratio of $\bar{h}$ to h (for model A) as a function of R. For $R \leq 5$ pc, the atmospheres are entirely dominated by radiation pressure. On sub-parsec scale (<1.5 pc), grains are sublimated and the opacity gradient induced due to the dust sublimation mainly governs the surface scale-height. Therefore, h is approximately $\bar{h}$ in this region. For $1.5 < R < 5$ pc, the region is still radiation dominated, but the maximum temperature is below the sublimation temperature of dust. Here, model $\bar{\rm A}$ possesses a lower density region than model A which results in a slightly higher $\bar{h}$ than h. For $R > 5$ pc, the region is mostly turbulence pressure dominated for model A and gas pressure dominated for model $\bar{\rm A}$. In these regions, the surface scale-height is primarily set by the pressure inversion phenomena. Model $\bar{\rm A}$ introduces higher pressure inversion than model A. Increasing pressure inversion causes increase in density (Helling & Winters,

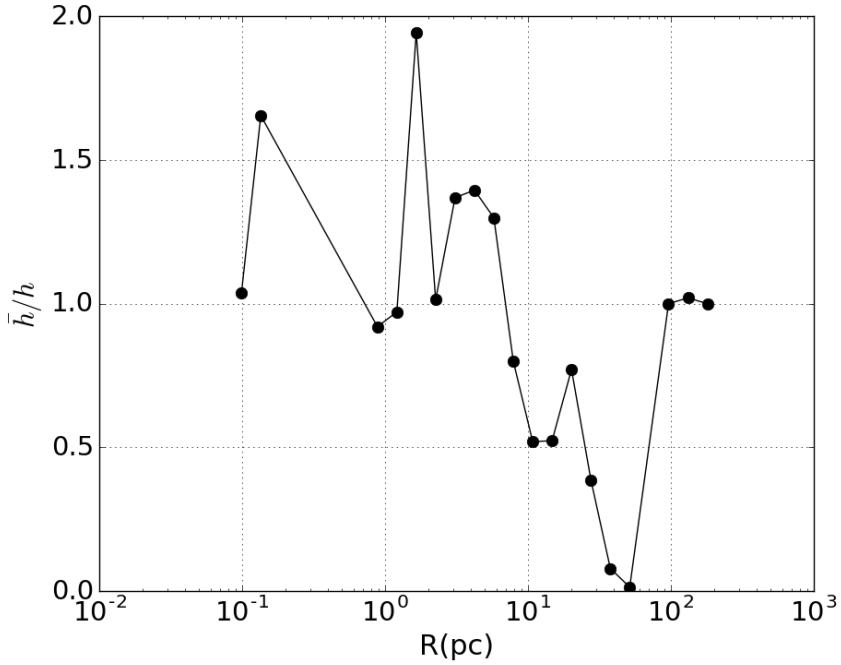

Figure 3.9: Illustrating the effect of vertical distribution of $\dot{\Sigma}_*$ on the surface scale-height. $\bar{h}$ (model $\bar{\text{A}}$) has a slight variation in comparison to h (model A) which are due to the following reasons: (1) a distribution of SF (model $\bar{\text{A}}$) decreases density near the mid-plane for radiation pressure dominated region in compare to model A, (2) P_{turb} is approximated with a constant v_{turb} when SF is only allowed to occur at the mid-plane, and (3) a difference in the amount of pressure inversion affects the difference in the scale-heights computed from both models.

2001) which results in decreasing $\bar{h}$ in comparison to h. At the outer radii, (last three slabs), a column of gas is optically thin; therefore, $\bar{h}/h = 1.0$. Another source of a difference in $\bar{h}$ and h is a difference in treatment of turbulence pressure in both models. For model A, P_{turb} was approximated by assuming a constant v_{turb}, while, for model $\bar{\text{A}}$, P_{turb} was computed exactly using Eq. 3.17. In summary, the vertical distribution of SF has a small effect on the surface scale-height. We also checked the N_{H} distributions from models A and $\bar{A}$ and their difference is negligible. In general, one expect to have a minimum effect of $\dot{\Sigma}_*(\Sigma) \propto \Sigma$ on the vertical structure. That is because a distribution of energy source only affects the Hopf function $q(\tau)$ which is introduced in the temperature solution of RTE and $T(\tau)$ has a weak dependance on the linear distribution of $\dot{\Sigma}_*$.

3.4.6 Caveats & Directions for Future Work

One of the important tasks in modeling a physical system is to be aware of possible caveats which can be introduced due to assumptions, approximations, or an exclusion of relevant mechanisms. In the presented framework of a NSD, due to the assumptions of diffusion approximation and grey problem, results from modeling may be inaccurate for an optically thin limit ($\tau << 1$). However, this does not affect our conclusion that NSDs posses an inflationary atmosphere on parsec/sub-parsec scale which can potentially obscure the AGN irradiation since $h \sim R$ is achieved before τ reaches the optically thin limit. Another implicit assumption due to statistics based on a random selection is that there is not any internal/natural biased in the sample of input parameters. However, this assumption may be imprecise; for instance, the black hole mass distribution function is not evenly weighted for a given redshift. Another caveat in the modeling is that it misses outflows. In star-forming regions, outflows are possible to occur due to stellar feedback (Leitherer et al., 1992), supernovae feedback (Chevalier & Clegg, 1985), and radiation pressure on dusty atmosphere (Murray et al., 2005). Moreover, outflows are observed in many star-forming galaxies with the speed of > 1000km s^{-1} at $z \sim 0.6$ (Tremonti et al., 2007; Diamond-Stanic

et al., 2012). In the sample of local starbursts, outflows with the speed of 1500 km s^{-1} are observed by Heckman et al. (2011). In the future, we may study our sampled models using Bayesian statistics in order to remove an intrinsic biased and compare its conclusion with statistics based on a random drawings.

Another missing ingredient in the modeling is the effect of AGN (if they are present in galaxies) on the NSD structure. To study its importance on the presented modeling, we compute the optical depth along line of sights ($\tau_{\rm los}$) for θ above the dust sublimation layer at the critical radius and check if $\tau_{\rm los}$ is greater than the unity. Only 16 out of 99 models are optically thin and being transparent to the ultraviolet (UV) radiation. Depending on the physical conditions of the NSD, the UV energy can be deposited near the surface or in the deeper region along a line of sight since $\tau_{\rm los}$ can be as large as 10^4. Moreover, we can compute the dust sublimation radius ($r_{\rm s}$) with the following equation (Barvainis, 1987):

$$r_s = 1.3 \left(\frac{L_{\rm UV}}{10^{46} \text{erg s}^{-1}} \right)^{1/2} \left(\frac{T_s}{1500\text{K}} \right)^{-2.8} \text{pc}. \tag{3.22}$$

Here, $L_{\rm UV}$ is the UV luminosity of the AGN and T_s is the sublimation temperature. Using the sublimation temperature of graphite grains (1750 K) and a typical bolometric luminosity (which gives the upper limit on r_s) range of Seyfert galaxies (10^{42} to 10^{44} ergs s^{-1}), the approximated r_s ranges from 0.008 to 0.08 pc, whereas Fig. 3.7 shows that the critical radius (where the largest expansion occurs in a disc) ranges from 0.1 to 2.3 pc. This implies that the AGN heating does not completely destroy the grains which are residing at the surface of the NSD at parsec scale. Based on this rough estimate, the AGN heating may not have a significant effect on the presented hydrostatic structure. However, a proper treatment of the AGN irradiation is required to be conclusive which will be done in detail in future work. Finally, NSDs may be present in galaxies with no central AGNs; therefore, this model may have wider applicability beyond AGNs.

Based on *Hubble Space Telescope* and ground based telescopes, nuclear star clusters (NSCs) are observed to be a common phenomena occurring in many types of galaxies: 70% in spheroidal galaxies (Côté et al., 2006) and 75% in late-type (Sc-Sd) disc galaxies (Böker et al., 2002; Walcher et al., 2005). Their sizes are at the parsec scale, 2-5 pc (Geha et al., 2002; Böker et al., 2004; Côté et al., 2006). Two possible scenarios are proposed for the formation of NSCs: (1) merger of dense clusters via dynamical friction (Andersen et al., 2008; Capuzzo-Dolcetta & Miocchi, 2008) and (2) gas accretion at the parsec-scale (Mastropietro et al., 2005; Seth et al., 2006). NSDs fall under the second scenario which can be a potential progenitor of NSCs. The NSD theory predicts a compact star-forming region with intense SF rate ($> 3M_{\odot}$year^{-1}) on parsec scale. Moreover, the 2D calculation of NSDs show these regions possess an environment whose scale-height is approximately larger by an order of magnitude than the radial distance. These characteristics of NSDs pose an interesting question: can nuclear star clusters be remnants of nuclear starburst discs? We will be addressing this question in the future investigation.

3.5 Conclusion

To summarize, we have successfully developed an iterative algorithm to compute the 2D hydrostatic structure of a nuclear starburst disc. These discs can be a potential source in obscuring the AGN radiation when an abundant amount of gas is available in galaxies at intermediate redshift fueling the central black hole. This modeling allows us to confirm that NSDs can possess the radiation pressure supported dusty structure on sub-parsec/parsec scale covering a major part of the sky (observed from a central back hole). Our results show that the NSD with fixed physical conditions can appear to be obscured by CN or CK gas depending on a viewing angle which supports the basic unification theory of AGNs. Below we summarize our main findings:

- A starburst phenomenon is more likely to occur in a disc with a smaller size, larger gas fraction, and higher Mach number.

- 52% (99/192) of models show the large expansion of an atmosphere on parsec/sub-parsec scales. This indicates that a large expansion at the parsec/sub-parsec scale is a common phenomenon in dusty star-forming regions.

- Within the input parameter space, the atmosphere can be expanded from 0.2 to ~ 30 h/R at the critical radius ($R_{\rm cric}$) ranging from $\sim$0.2 to $\sim$2 pc. For a lower black hole mass, the inflation occurs closer to the black hole as indicated in Fig. 3.7.

- Based on the random sample of input parameters, the NSD theory predicts 56% of Type 1, 23% of CN Type 2s, and 21% of CK AGNs. Within the sample of obscured AGNs, the distribution of CN Type 2s peaks near $10^{23.5}$ cm^{-2}. These predictions are consistent with observational evidence (e.g., Akylas & Georgantopoulos, 2009; Burlon et al., 2011; Brightman & Nandra, 2011a; Ueda et al., 2014).

- Based on the 2D NSD theory, $N_{\rm H}$ along a line of sight varies from $10^{22.5}$ cm^{-2} to $10^{29.5}$ cm^{-2}. From an edge-on view, all NSD models appear to be CK which is expected since dense gas resides at the mid-plane.

- Our results show a heavily obscured CN and CK AGNs span almost the entire range of θ from 0° to $\approx$80°. The given AGN-NSD system (fixed input parameters) appears to be CN to CK for θ less than $\theta_{\rm max}$; otherwise, the central AGN would appear to be Type 1. This supports the basic unification theory of AGNs. The restrictions on $N_{H,\rm max}$ and $\theta_{\rm max}$ of this system is determined by its physical conditions (input parameters).

- A linear vertical distribution of $\dot{\Sigma}_*$ has an insignificant effect on $N_{\rm H}$ distributions since the distribution of SF only affects the temperature solution of RTE (Eq. 3.7) and its effect is negligible.

CHAPTER 4
THE SHAPE OF THE COSMIC X-RAY BACKGROUND: NUCLEAR STARBURST DISCS AND THE REDSHIFT EVOLUTION OF AGN OBSCURATION

4.1 Introduction

The cosmic X-ray background (CXB) spans roughly 1 keV to 400 keV and the shape of its spectrum is characterized by a power law with the photon index of $\Gamma = 1.4 - 1.52$ in the 2-10 keV band (Marshall et al., 1980; De Luca & Molendi, 2004; Moretti et al., 2009; Cappelluti et al., 2017) and a peak in the $\sim$ 20-30 keV band (Gruber et al., 1999). The spectrum up to a few keV is resolved mostly into point sources from the observations of *XMM-Newton* and *Chandra* (Worsley et al., 2005). Many of these sources are confirmed to be active galactic nuclei (AGNs) (Bauer et al., 2004) which suggests that the CXB may be the integrated X-ray spectrum of AGNs throughout the history of the Universe. Numerous AGN spectra exhibit the presence of dusty and gaseous regions (Gilli et al., 2007; Lawrence & Elvis, 2010). The distribution of column density along the line of sight ($N_{\rm H}$) is a key ingredient in modeling the CXB (Akylas et al., 2012), especially the fraction of Compton-thick (CK) AGNs ($f_{\rm CK}$) where the reflection due to the Compton scattering becomes important. They possess a large amount of material ($N_{\rm H} > 10^{24}$ cm^{-2}) along the line of sight which makes them very difficult to observe even in X-ray. Moreover, a wide range of $f_{\rm CK}$ from 5% to 50% can produce the observed CXB spectrum due to the degeneracy within modeling input parameters (Akylas et al., 2012). Therefore, it is essential to compute a theoretically motivated $N_{\rm H}$ distribution.

The physical conditions, driving mechanisms, and geometrical configuration of the obscuring region in the vicinity of AGNs are very poorly known. They appear to be dependent

on the AGN luminosity (Akylas et al., 2006; Hasinger, 2008; Ebrero et al., 2009; Burlon et al., 2011; Ueda et al., 2014; Aird et al., 2015; Buchner et al., 2015; Sazonov et al., 2015) and also possibly on redshift (Ballantyne et al., 2006b; Hasinger, 2008; Brightman & Ueda, 2012; Iwasawa et al., 2012; Vito et al., 2014). Moreover, various mechanisms and physical conditions can play an important role for this observed obscuration such as a dusty atmosphere, star-formation, radiation pressure dominance, stellar wind, magnetic field, AGN feedback, and so-forth. For example, based on the study of 836 AGNs from hard X-ray Swift Burst Alert Telescope survey, Ricci et al. (2017) find that the radiation pressure on dust plays an important role in distributing the circumnuclear material which is mainly driven by an accretion rate. Furthermore, these regions may vary significantly from galaxy to galaxy (i.e., between Seyfert galaxies and quasars). To explain the observed properties of $N_{\rm H}$, various modeling perspectives have been proposed: a simple uniform toroidal torus (Krolik & Begelman, 1986; Pier & Krolik, 1992), geometrically thick medium supported by infrared (IR) radiation pressure (Krolik, 2007; Dorodnitsyn et al., 2011; Dorodnitsyn & Kallman, 2012; Chan & Krolik, 2016; Dorodnitsyn et al., 2016), the turbulent pressure dominated torus (Wada & Tomisaka, 2005; Watabe & Umemura, 2005), warped/tilted discs (Nayakshin, 2005; Caproni et al., 2006; Lawrence & Elvis, 2010), a clumpy torus (Hönig & Beckert, 2007; Nenkova et al., 2008; Hönig & Kishimoto, 2010), and nuclear starburst discs (Fabian et al., 1998; Wada & Norman, 2002; Thompson et al., 2005; Ballantyne, 2008; Hopkins et al., 2016; Gohil & Ballantyne, 2017).

A great deal of work is done in modeling the observed cosmic X-ray background (e.g., Ueda et al., 2003; Treister & Urry, 2005; Ballantyne et al., 2006a; Gilli et al., 2007; Draper & Ballantyne, 2009; Draper & Ballantyne, 2010). However, the $N_{\rm H}$ distributions used in those models are not related to any physical mechanism. Nuclear starburst discs are promising candidates to explain the obscuration in Seyfert galaxies at intermediate redshift $z \sim 1$ (Ballantyne, 2008; Gohil & Ballantyne, 2017). This is the era when there is a large gas-fraction available in galaxies (i.e., Narayanan et al., 2012) and not long after the

peak in the history of cosmic star-formation rate is observed (Madau & Dickinson, 2014). Moreover, one-dimensional (1D) (Thompson et al., 2005) and two-dimensional (Gohil & Ballantyne, 2017) model of NSDs suggest that a disc can possess an inflationary atmosphere at parsec/sub-parsec scale when the grains are sublimated at mid-plane. Then, the AGN spectrum can be reprocessed by such an expanded atmosphere. Therefore, in this work, we use the 2D NSD theory of Gohil & Ballantyne (2017) and compute 768 NSDs across the input parameter space (disc size, Mach number, gas fraction, and black hole mass). A distribution of column density along the line of sight ($N_{\rm H}$) is computed using these models. Afterward, the $N_{\rm H}$ distribution is evolved by calculating redshift dependent distribution functions of the input parameters. By utilizing the evolution of the $N_{\rm H}$ distribution, we predict the cosmic X-ray background as well as the AGN number counts in 2-8 keV and 8-24 keV bands.

Sect. 4.2 reviews the modeling aspect of the 2D NSD structure. Sect. 4.3 describes the methodology used in order to evolve the $N_{\rm H}$ distribution. In Sect. 4.4, we provide the results including the predicted cosmic X-ray background and also the AGN number counts in 2-8 keV and 8-24 keV bands. Sect. 4.5 discusses the results and compares to observations. Then, the paper is concluded in Sect. 4.6.

4.2 A Brief Review on Modeling of NSDs

Gohil & Ballantyne (2017) predicted the integrated $N_{\rm H}$ distribution associated with the starburst regions by modeling the 2D hydrostatic structure of NSDs. The modeling of a NSD depends on four input parameters: disc size $R_{\rm out}$, the black hole mass $M_{\rm bh}$, the gas fraction at the outer radius $f_{\rm g,out}$, and the Mach number $m = v_r/c_s$, where v_r and c_s are the radial velocity and the speed of sound, respectively (frequently used variables in the paper are described in Table 4.1.). We assumed that the discs are symmetric around the $z = 0$ plane and z-axis. The first step in constructing the 2D structure was to compute the radial distribution of the mass integrated column density $\Sigma_{\rm mp}(R)$ and the energy content which

Table 4.1: Description of symbols used frequently in the paper.

Symbol	Description
f_2	Fraction of Type-2 AGNs
f_{2,R_f}	Fraction of obscured AGNs with high reflection
$f_{2,Q}$	Fraction of obscured quasars
$f_{\rm CK}$	Fraction of Compton-thick AGNs
$f_{\rm CN}$	Fraction of Compton-thin AGNs
$f_{\rm g,out}$	Gas fraction at the outer radius
L	Bolometric luminosity
$M_{\rm bh}$	A black hole mass
$N_{\rm H}$	Column density along the line of sight
R_f	Reflection parameter
$R_{\rm out}$	Size of a nuclear starburst disc
$P(\lambda)$	Eddington ratio distribution
$\Phi_{\rm AGN}$	Distribution function of an active black hole mass
Φ_f	Distribution function gas fraction
θ	Viewing angle
z	redshift

was parameterized by the effective temperature $T_{\rm eff}(R)$. These were obtained by following 1D NSD model of Thompson et al. (2005). The disc was then divided into a number of annuli and, for each annulus of a given $\Sigma_{\rm mp}$ and $T_{\rm eff}$, the hydrostatic structure was obtained. The vertical structure was computed by solving coupled equations of hydrostatic balance, energy balance, and the radiative transfer using the iterative method. By resolving the structure at every annulus, we computed the 2D structure of NSDs where the physical quantities (i.e., temperature, density, and opacity) varied with the radial distance R and the viewing angle θ (measured at the mid-plane).

The NSDs were modeled under various physical conditions which span a large range of the input parameter space. In total 192 models were computed and the range of their input parameters are shown in Table 2 of Gohil & Ballantyne (2017). In total 99 models showed a starburst phenomenon at the parsec/sub-parsec scale (0.2-2 pc) when the discs exceeded the dust sublimation temperature at mid-plane. This causes a large opacity gradient resulting in an inflationary atmosphere. The phenomenon is more common in discs with a smaller size, a larger gas fraction, and/or high Mach number. These discs exhibit the inflated atmosphere

with surface height (h) ranging from 0.2 to 30 R. Since 52 per cent of discs show a large expanded atmosphere, this suggests that the starburst phenomena could be common and these conditions can potentially obscure the incoming AGN radiation. Moreover, the $N_{\rm H}$ distribution as a function of θ for a given NSD shows that its AGN can be observed as Type-1 (T1), Compton-thin (CN), or CK depending on the viewing angle. This conclusion is in agreement with the simple unification theory of AGNs which states the Type-1 and Type-2 AGNs are intrinsically the same objects except their orientations are different with respect to an observer (Antonucci, 1993; Netzer, 2015).

Finally, the $N_{\rm H}$ distribution associated with a sample of 192 discs was computed based on random selection. The predicted $N_{\rm H}$ distribution had a few features which were consistent with the observational evidence. First, the fraction of obscured AGNs (f_2) peaks near 10^{23} cm^{-2} (Burlon et al., 2011; Ueda et al., 2014; Buchner et al., 2015; Sazonov et al., 2015). Second, the 2D NSD theory predicts the ratio of CN to CK AGNs to be 0.9 (Gohil & Ballantyne, 2017) which is within the required range, 0.5-1.6, of producing the 20-50 keV part of the CXB spectrum (Ueda et al., 2014). Third, the fraction of CK AGNs ($f_{\rm CK}$) associated with the NSDs is 21% (Gohil & Ballantyne, 2017) which is within the uncertainties of observational evidence (Akylas & Georgantopoulos, 2009; Burlon et al., 2011; Brightman & Ueda, 2012; Ricci et al., 2017). This consistency leads to the conclusion that the starburst discs can obscure the AGNs and may also be the dominant contributors to the peak of CXB spectrum. [1]

[1]The 2D NSD model was updated with energy input from AGN irradiation by following the similar scheme as described in Appendix (d) of Hubeny (1990). The AGN irradiation has an insignificant effect on the structure of NSDs since the energy content from the starburst outshines the AGN spectrum at parsec/sub-parsec scale while the AGN spectrum weakens at a larger distance. This result is consistent with the conclusion of Gohil & Ballantyne (2017) which was based on the rough estimate of the dust sublimation radius and the optical depth along the line of sight. Outflows driven by star-formation or AGN irradiation are not considered by this model.

4.3 Methodology: Evolution of the $N_{\rm H}$ Distribution

Gohil & Ballantyne (2017) computed the $N_{\rm H}$ distribution based on the random distribution of input parameters. In order to evolve the $N_{\rm H}$ distribution with redshift, we take the statistical approach where the observationally motivated distribution functions of input parameters are adopted. Since these functions have a redshift dependency, one can compute the $N_{\rm H}$ distribution with respect to redshift. Unfortunately, there is not enough observational data on the disc size $R_{\rm out}$ and the Mach number m. Therefore, their weights (probability) are assumed to be uniform. For $R_{\rm out}$ and m, we choose

$$R_j \equiv R_{\rm out} \in [60, 120, 180, 240]\text{pc} \quad \text{and} \tag{4.1}$$

$$m_l \in [0.1, 0.3, 0.5]. \tag{4.2}$$

Then, their respective weights are

$$W_R(z, R) = 1/4, \quad \text{and} \tag{4.3}$$

$$W_m(z, m) = 1/3. \tag{4.4}$$

However, there is enough observational data which can be used to compute the distribution functions of active black hole mass $M_{\rm bh}$ and the gas fraction in galaxies.

4.3.1 Evolution of the AGN Mass Function $\Phi_{\rm AGN}$

Mass of a black hole plays an important role in deciding the location of starburst phenomenon in NSDs (Ballantyne, 2008; Gohil & Ballantyne, 2017). For instance, gas has to accrete more to smaller radii before reaching the sublimation temperature of dust for a lower $M_{\rm bh}$. A bolometric luminosity of an AGN (L) is directly linked to a central black hole ($M_{\rm bh}$) through the Eddington radio ($\lambda = L/L_{\rm Edd}$), where $L_{\rm Edd} = lM_{\rm bh}$ with $l \approx 1.26 \times 10^{38} M_{\odot}^{-1}$erg s^{-1}. Given the Eddington ratio distribution $P(\lambda)$ and the AGN

luminosity function Φ_L, the AGN mass function ($\Phi_{\rm AGN}$) is computed as

$$\Phi_{\rm AGN}(z, L) = \int_{\log(\lambda_{\rm min})}^{0} \Phi_L(z, L) P(\lambda) d\log\lambda. \tag{4.5}$$

In terms of $M_{\rm bh}$, $\Phi_{\rm AGN}$ becomes

$$\Phi_{\rm AGN}(z, M_{\rm bh}) = \int_{\log[\lambda_{\rm min}(M_{\rm bh})]}^{0} \Phi_L(z, L(M_{\rm bh}, \lambda)) P(\lambda) d\log\lambda. \tag{4.6}$$

The lower limit on the Eddington ratio $\lambda_{\rm min}$ is set by the definition of an AGN ($L \geq 10^{42}$ erg s^{-1}). Then, $\lambda_{\rm min}$ is linked to the active black hole mass $M_{\rm bh}$ by

$$\lambda_{\rm min}(M_{\rm bh}) = \frac{10^{42}\ \text{erg s}^{-1}}{l(M_{\rm bh}/M_{\odot})}. \tag{4.7}$$

For the AGN luminosity function, we adopt the work of Ueda et al. (2014). The bolometric luminosity (L) is converted into the X-ray luminosity(L_x) by

$$\log(L/L_x) = 1.54 + 0.24\zeta + 0.012\zeta^2 - 0.0015\zeta^3 \tag{4.8}$$

where $\zeta = \log(L/L_{\odot}) - 12$ and $L_{\odot} = 4 \times 10^{33}$ ergs s^{-1} (Marconi et al., 2004). Unfortunately, the Eddington ratio distribution $P(\lambda)$ is very poorly known observationally. They are observed to be in two forms: log-normal and power-law distribution (e.g., Kollmeier et al., 2006; Aird et al., 2012; Kelly & Shen, 2013; Shankar et al., 2013). We tried both forms of the Eddington ratio distribution from Tucci & Volonteri (2017) which also has dependency on redshift. The log-normal distribution from Tucci & Volonteri (2017) takes the form of

$$P(\lambda, z) = \frac{1}{2\pi\sigma(z)\lambda} \exp\Big[- \frac{(\ln\lambda - \ln\lambda_0)^2}{2\sigma^2(z)} \Big]. \tag{4.9}$$

Here, the the central value λ_0 and the dispersion σ are

$$\log \lambda_0(z) = \max[-1.9 + 0.45z, \log(0.03)] \text{ and} \tag{4.10}$$

$$\sigma(z) = \max[1.03 - 0.15z, 0.6], \tag{4.11}$$

respectively. The log-normal distribution is more favored for high luminous Type-1 AGNs and they may be related to the thin accretion flow (Trump et al., 2011). The power-law distribution of the Eddington ratio takes the form of (Tucci & Volonteri, 2017)

$$P(\lambda, z) = P_0(z)\lambda^{\alpha_\lambda(z)} e^{-\lambda/\lambda_0} \tag{4.12}$$

where

$$\alpha_\lambda = \begin{cases} -0.6 & z \leq 0.6 \\ -0.6/(0.4 + z) & z > 0.6. \end{cases} \tag{4.13}$$

Here, λ_0 is 1.5 for $\eta \leq 0.1$ or $\lambda_0 = 2.5$ otherwise. Eq. 4.12 seems to be associated with the Type-2 AGNs (Aird et al., 2012) and is also consistent with work of Hopkins & Hernquist (2009), Kauffmann & Heckman (2009), and Aird et al. (2012) at low redshift.

Finally, one can compute the active black hole mass function by using Eq. 4.6. We choose a total of 16 bins in the domain of $x = \log(M_{\text{bh}})$,

$$\begin{aligned} x_i \in &[6.5, 6.6, 6.7, 6.8, 6.9, 7.0, 7.1, 7.2, \\ &7.3, 7.4, 7.5, 7.6, 7.7, 7.8, 7.9, 8.0]. \end{aligned} \tag{4.14}$$

Then, the proper weights (probability) of each bin W_x is computed by

$$W_x(z, x) = \frac{\Phi_{\text{AGN}}(z, x)}{\sum_i \Phi_{\text{AGN}}(z, x_i)}. \tag{4.15}$$

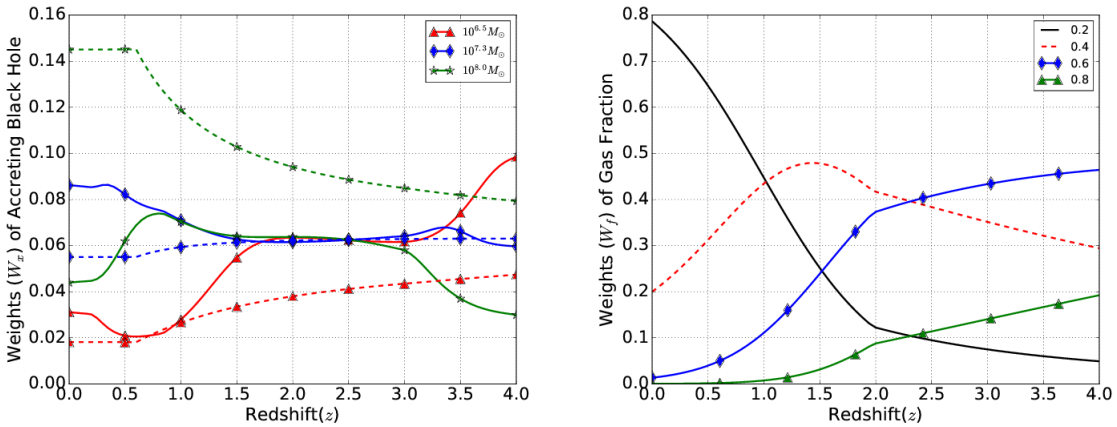

Figure 4.1: *Left:* Illustrating the probability weights of black hole mass $10^{6.5}M_\odot$,$10^{7.3}M_\odot$, and $10^{8.0}M_\odot$ as a function of redshift (Eq. 4.15). The solid and dashed curves are computed assuming the log-normal (Eq. 4.9) and power-law (Eq. 4.12) distribution of $P(\lambda)$, respectively. Regardless of a choice on $P(\lambda)$, weights of low-end mass accreting black holes increases with redshift and the reverse holds true for the high-end black hole mass. We have tested both the distribution functions of $P(\lambda)$ and they have a negligible effect on the evolution of $N_{\rm H}$ distribution. *Right:* The panel illustrates the probability weights W_f of 20%, 40%, 60%, and 80% gas fraction as a function of redshift (Eq. 4.20) which are represented by black, red, blue, and green curves, respectively. In general, the figure follows the observational feature that the gas fraction increases with redshift.

The left panel of Fig. 4.1 illustrates the weights of an active black hole mass W_x as a function of redshift. The solid curve represents the log-normal distribution of $P(\lambda)$ (Eq. 4.9), while the dashed curve is computed using the power-law distribution (Eq. 4.12). The red, green, and blue color show W_x for the black hole mass of $10^{6.5}M_\odot$,$10^{7.3}M_\odot$, and $10^{8.0}M_\odot$, respectively. In the case of log-normal distribution, black holes with the mass near $10^{7.3}M_\odot$ dominates in the local universe, while the lower black hole mass dominates at higher redshift. At $z \sim 2$, black holes in the entire domain of $M_{\rm bh}$ seem to have equal contribution. On other hand, when the power-law distribution is chosen, the weights of

higher black hole mass dominate redshift. With either choice of $P(\lambda)$, the result shows that the weights of lower black hole mass increases with redshift and the reverse is true for the higher black hole mass. There are some differences in active black hole mass function and its evolution depending on the choice of $P(\lambda)$. However, a choice of of $P(\lambda)$ has negligible effect on the final results (the evolution of $N_{\rm H}$ distribution and the CXB spectrum) and that is because the statistical evolution of $N_{\rm H}$ distribution is mainly governed by the weights of $f_{\rm g,out}$ rather than $M_{\rm bh}$. Therefore, we select the power-law distribution $P(\lambda)$ for the further work since that particular distribution $P(\lambda)$ seems to be associated with Type-2 AGNs (Aird et al., 2012).

4.3.2 Evolution of the Gas Fraction Function Φ_f

Gohil & Ballantyne (2017) showed that the AGN obscuration phenomenon depends on the gas fraction in NSDs. With the higher gas fraction, more amount of gas is available to accrete which increases a column of gas in annulus $\Sigma_{\rm mp}$ and, in turn, controls an expansion of an atmosphere. An overall gas fraction (f_0) in galaxies is observed to be increasing with redshift. f_0 is related to the depletion time and the specific star-formation rate (sSFR) through

$$f_0(z) = \frac{1}{1 + (t_{\rm dep}(z)\text{sSFR}(z))^{-1}}. \tag{4.16}$$

The depletion time is estimated to be (Saintonge et al., 2013)

$$t_{\rm dep} = 1.5(1+z)^{\alpha}[\text{Gyr}] \tag{4.17}$$

with $\alpha = -1.0$ (Tacconi et al., 2013). Lilly et al. (2013) provides the analytical expression

for the evolution of sSFR given by

$$\text{sSFR}(M_*, z) = \begin{cases} 0.07\Big(\frac{M_*}{10^{10.5}M_\odot}\Big)^{-0.1}(1+z)^3 & z < 2 \\ 0.30\Big(\frac{M_*}{10^{10.5}M_\odot}\Big)^{-0.1}(1+z)^{5/3} & z \geq 2 \end{cases} \tag{4.18}$$

which was motivated from observational data (e.g., Daddi et al., 2007; Elbaz et al., 2007; Noeske et al., 2007; Pannella et al., 2009; Stark et al., 2013). Since there is a weak dependence on the galaxy mass M_*, we choose $M_* = 10^{10.5}M_\odot$. Then, the distribution of gas fraction (Φ_f) is assumed to be Gaussian around f_0 which is given by

$$\Phi_f(z, f) = \frac{1}{\sqrt{2\pi}\sigma_f} \exp\Big[-\frac{(f-f_0)^2}{2\sigma_f^2}\Big]. \tag{4.19}$$

The dispersion σ_f is estimated to be 0.2 by roughly fitting the Gaussian to the results of Tacconi et al. (2013). Finally, we can compute the weights W_f of input parameter $f \equiv f_{\text{g,out}}$ from

$$W_f(z, f) = \frac{\Phi_f(z, f)}{\sum\limits_k \Phi_f(z, f_k)} \tag{4.20}$$

where

$$f_k \in [0.2, 0.4, 0.6, 0.8]. \tag{4.21}$$

The right panel of Fig. 4.1 shows the evolution of 20%, 40%, 60%, and 80% gas fraction with redshift which are represented by black, red, blue, and green curves, respectively. At low redshift, NSDs with low gas fraction dominates the sample, while NSDs with a 40% gas fraction dominates at $1< z <2$. Beyond $z = 2$, NSDs with a 60% gas fraction dominates. W_f of NSDs with low gas fraction decreases overall with redshift and the reverse is true for the the NSDs with the high gas fraction (60% and 80%). Similar to the

observational evidence, the figure illustrates that the dominant gas fraction increases with z and its evolution flattens out at higher redshift.

4.3.3 Evolution of the $N_{\rm H}$ Distribution

Using redshift dependent weights of input parameters ($W_x(z)$,W_R,$W_f(z)$, and W_m), one can evolve the $N_{\rm H}$ distribution with redshift $W_{N_{\rm H}}(z)$. The $N_{\rm H}$ distribution is divided among 11 bins

$$\begin{aligned}\log[N_H(\text{cm}^{-2})] \in &[20.0, 20.5, 21.0, 21.5, 22.0, 22.5,\\ &23.0, 23.5, 24.0, 24.5, 25].\end{aligned} \tag{4.22}$$

For a given NSD disc, a viewing angle (an orientation of an NSD with respect to an observer) is divided into 30 bins between 0 and 90 degrees. Then, the weights of $N_{\rm H}$ bins $W_{N_{\rm H}}(\vec{I})$ for the disc is given by

$$W_{N_{\rm H}}(\vec{I}_P, N_{\rm H}) = N(N_{\rm H})/N_{\rm tot} \tag{4.23}$$

where $N(N_{\rm H})$ is the number of column density with $N_{\rm H}$ and $N_{\rm tot}$ is the total number of columns of gas. The weights of $\log[N_H(\text{cm}^{-2})] = 20.0$ and $\log[N_H(\text{cm}^{-2})] = 25.0$ bins include all the lines of sight with column density $N_H \leq 10^{20}\text{cm}^{-2}$ and $N_H \geq 10^{25}\text{cm}^{-2}$, respectively. $\vec{I}_P$ is the input parameter vector equal to $[x, R_{\rm out}, f_{\rm g,out}, m]$. In total, 768 models are computed across the input parameter space which gives 23,040 (768×30) columns of gas. Then, the evolution of $N_{\rm H}$ distribution is given by

$$W_{N_{\rm H}}(z, N_{\rm H}) = A_N \sum_{i,j,k,l} W_{N_{\rm H}}(\vec{I}_P, N_{\rm H})\Pi(z, \vec{I}_P) \tag{4.24}$$

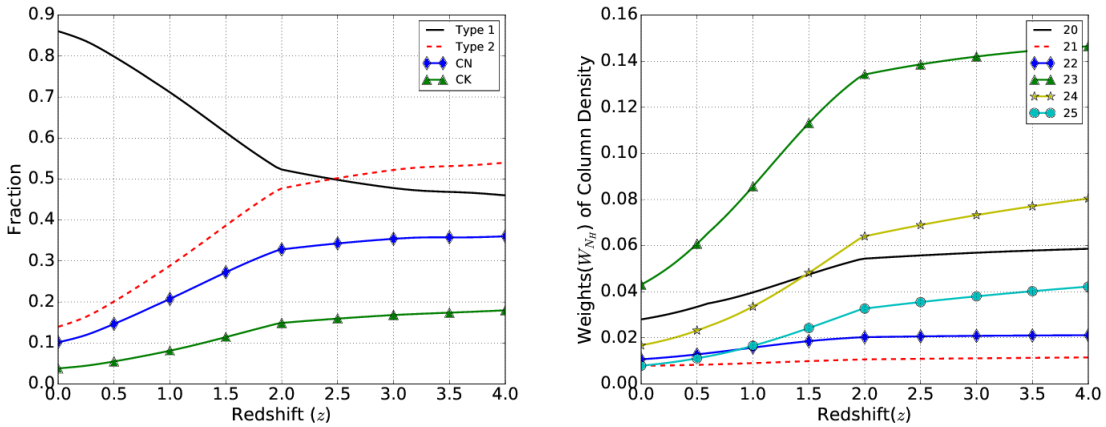

Figure 4.2: *Left:* The figure shows the evolution for different type of AGN fractions. The fraction of Type-1 AGNs decreases with redshift while the converse is true for the Type-2 AGNs. The fraction of Type-2 AGN, CN, and CK AGNs evolve as $(1+z)^{\delta}$ with δ equal 1.2, 1.12, and 1.45 for $z < 2$, respectively. Beyond this redshift, their evolution strength decrease to 0.24, 0.16, and 0.42, respectively. *Right:* The evolution of a few columns of gas (Eq. 4.24) are shown here. All $N_{\rm H}$ bins exhibit the evolution with z and the $N_{\rm H} \sim 10^{23}$ cm^{-2} dominates the distribution for all redshifts.

where

$$\Pi(z, \vec{I_P}) = W_x(z, x) \times W_f(z, f) \times W_m \times W_R \tag{4.25}$$

and A_N is the normalization constant. By using Eq. 4.24, the evolution of Type-1, Type-2, CN and CK fractions can be predicted, as well as the evolution of each column density $N_{\rm H}$. The results are shown in Fig. 4.2.

4.4 Results

By employing an adequate statistical method, we compute the evolution of AGN obscuration. By utilizing this result, we later predict the cosmic X-ray background and the AGN number counts in 2-8 keV and 8-24 keV bands as well as in different $N_{\rm H}$ bins.

4.4.1 Evolution of AGN obscuration

A simple statistical evolution shows that obscuring material has a strong evolution with redshift which is illustrated in Fig. 4.2. The left panel exhibits that the evolution of Type-1, Type-2, CN, and CK AGN fractions are represented by black-solid, red-dashed, blue-diamond, and green-triangle curves, respectively. All the fractions of obscured AGNs increase with redshift, while the Type-1 AGN fraction decreases.[2] The AGN fractions have a strong evolution up to $z = 2$ which is also concluded by many other groups (Ballantyne et al., 2006b; Treister et al., 2006; Ueda et al., 2014; Liu et al., 2017). For $z > 2$, there is a weak dependence on redshift which is also consistent with the work of Liu et al. (2017). The drastic change at $z = 2$ can be explained by the discontinuous sSFR function which is given by Eq. 4.18. The ratio of CN AGN fraction ($f_{\rm CN}$) to $f_{\rm CK}$ is always higher than 1 throughout the redshift range. The right panel shows the evolution of a few individual column density bins. The black-solid, red-dashed, blue-diamond, green-triangle, yellow-star, and cyan-circle curves represent a column of gas with $\log[N_{\rm H}({\rm cm}^{-2})]$ equal 20, 21, 22, 23, 24, and 25, respectively. In general, their weights $W_{N_{\rm H}}$ are predicted to increase with redshift. The panel exhibits that the $N_{\rm H}$ distribution peaks near 10^{23} cm^{-2} throughout the redshift range which is in agreement with observations (e.g., Burlon et al., 2011; Ueda et al., 2014; Buchner et al., 2015; Sazonov et al., 2015). The unobscured AGNs with $N_{\rm H} = 10^{20}$ cm^{-2} have a strong evolution while the AGNs with $N_{\rm H} = 10^{21}$ cm^{-2} possess a weak dependence on z.

The evolution strength of the AGN fraction can be measured by fitting the power-law $(1+z)^{\delta}$. $\delta = \delta_1$ and $\delta = \delta_2$ represent the power-law index for $z < 2$ and $z > 2$, respectively and their values are shown in Table 4.2. The $f_{\rm CK}$ always has a slightly stronger evolution than $f_{\rm CN}$. The strength of an evolution for each $N_{\rm H}$ bin is again measured by fitting the power-law $W_{N_{\rm H}} \propto (1+z)^{\alpha}$. The power index $\alpha = \alpha_1$ for $z < 2$ (solid curve) and $\alpha = \alpha_2$

[2]The sample of $N_{\rm H}$ distribution has a column of gas along all the line of sight from 0° to 90°. We added the galactic scale obscuration (10^{20} cm^{-2}) to the line of sights which has zero column density from nuclear regions.

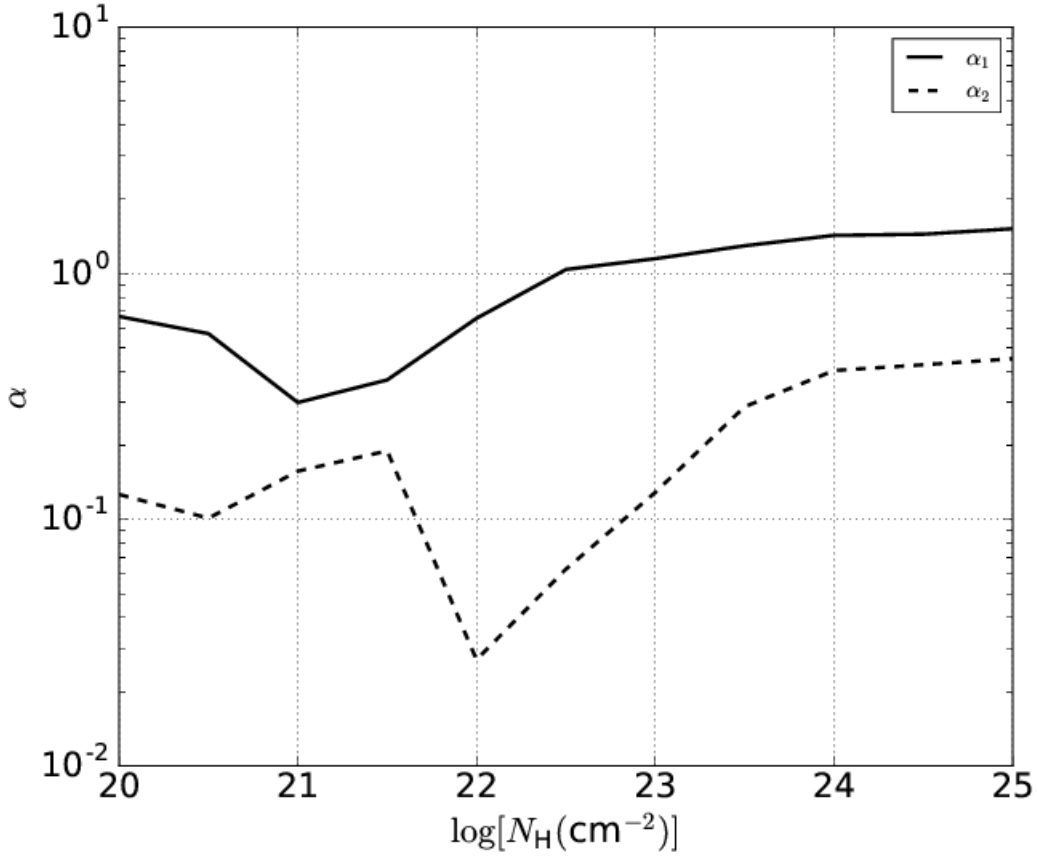

Figure 4.3: Figure illustrates the dependence of evolution strength α on $N_{\rm H}$, where α is the power-law index such that $W_{N_{\rm H}} \propto (1+z)^{\alpha}$. AGNs with increasing $N_{\rm H}$ have a faster evolution for both cases: $z < 2$ (solid curve) and $z > 2$ (dashed curve). In other words, the difference between the fraction of a given $N_{\rm H}$ bin at $z = 0$ and $z = 2$ significantly rises as the $N_{\rm H}$ increases.

Table 4.2: The redshift evolution $(1+z)^{\delta}$ of Type-1, Type-2, CN, and CK AGN fractions are characterized by the power-law index δ. $\delta = \delta_1$ and $\delta = \delta_2$ represent the evolution strength for $z < 2$ and $z > 2$, respectively.

Obscuration	$\delta_1(z<2)$	$\delta_2(z>2)$
f_1	-0.43	-0.28
f_2	1.2	0.24
$f_{\rm CN}$	1.12	0.16
$f_{\rm CK}$	1.45	0.42

for $z > 2$ (dash curve) as a function of a column density are illustrated in Fig. 4.3. The power-law indices are predicted to increase with the amount of obscuration for obscured AGNs in both eras: $z < 2$ and $z > 2$. The α has a weak dependence on column density in Compton thick regime. Fig. 4.3 also suggests that the evolution of AGN environment highly depends on obscuring medium. The difference between the AGN fraction of a given $N_{\rm H}$ bin in local universe and at $z = 2$ increases as the amount of obscuration ($N_{\rm H}$) increases. Similar conclusion holds true while comparing the AGN fraction at $z = 2$ and $z = 4$.

4.4.2 Cosmic X-ray Background

By utilizing redshift dependent $N_{\rm H}$ distribution $W_{N_H}(N_{\rm H}, z)$ and starting with the work of Ballantyne et al. (2011), we predict the cosmic X-ray background (CXB) associated with the dusty starburst regions.[3] Since the average photon index of an intrinsic AGN X-ray spectrum $\langle\Gamma\rangle$ is observed to peak near 1.85 (Ueda et al., 2014), the $\langle\Gamma\rangle$ is fixed at 1.85. The high energy cutoff $E_c = 220$ keV is chosen such that the best fit to the observed CXB spectrum is produced. We also introduce the redshift dependent reflection fraction $R_f(z)$ which is defined as

$$R_f(z) \equiv \frac{4\pi f_{2,R_f}(z)}{2\pi}.$$

Here, the fraction of AGNs with high reflection $f_{2,R_f}(z)$ is computed using the $N_{\rm H}(z)$ distribution from the 2D NSD theory. Since, high reflection is also observed from moderately obscured CT AGNs (Ricci et al., 2011; Esposito & Walter, 2016), $f_{2,R_f}(z)$ is defined as the fraction of $N_{\rm H}$ from $10^{23.5}$ to 10^{25} cm^{-2}. The $N_{\rm H}$ distribution of NSDs is used for $L_{2-10\rm keV} < 10^{44}$ erg s^{-1} (Seyfert regime) since they are more viable source of obscuration for "Seyfert-like" AGNs (Ballantyne, 2008; Gohil & Ballantyne, 2017). For $L_{2-10\rm keV} > 10^{44}$ erg s^{-1} (quasar regime), we adopt two cases: (i) only unobscured AGNs in order to study the consequences of solely NSDs on CXB spectrum, and (ii) the fraction of

[3]The AGN luminosity function used is from the work of Ueda et al. (2014).

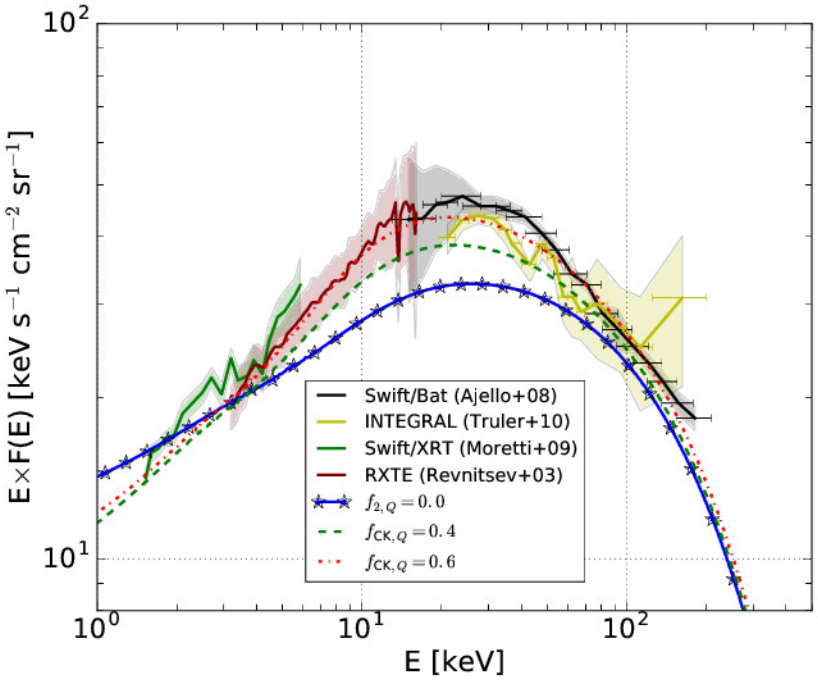

Figure 4.4: The predicted CXB spectra are shown by assuming the photon-index $\langle\Gamma\rangle = 1.85$ (Ueda et al., 2014) for an intrinsic AGN X-ray spectrum and the high energy cutoff $E_c = 220$ keV. The shaded area represents uncertainty in observational data. The blue-star curve is the predicted CXB spectrum produced by AGNs with $L_{2-10\mathrm{keV}} < 10^{44}$ erg s^{-1} (Seyfert regime). These AGNs are obscured by nuclear starburst discs with the N_{H} distribution given by the 2D NSD theory while the AGNs with $L_{2-10\mathrm{keV}} > 10^{44}$ erg s^{-1} (quasar regime) are assumed to be unobscured. The $E < 3.0$ part of the spectrum is overestimated while the spectrum has a lower peak (blue-star curve) with comparison to the observed one (shaded area). In order to produce the correct SED, at least 40 per cent of CK "quasars-like" AGNs are required (green-dashed curve). The contribution of 20 per cent CN and 60 per cent CK quasars predict the best fit spectrum to observations which is shown by the red-dash-dotted curve. The spectrum has $\Gamma = 1.49$ in 2-10 keV bands which is consistent with observations (e.g., Moretti et al., 2009; Cappelluti et al., 2017)

.

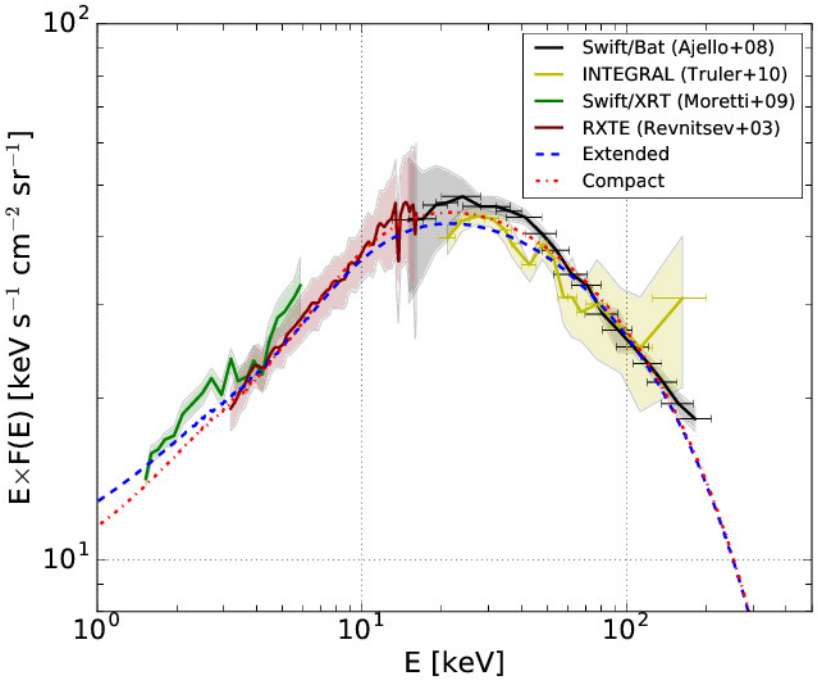

Figure 4.5: The compact ($R_{\rm out}$ with 60 pc and 120 pc) and extended ($R_{\rm out}$ with 180 pc and 240 pc) NSDs do not have a significant difference on the CXB spectrum. However, the peak of the spectrum has a slightly better match with the observations when only the compact NSDs are used. The 2-10 keV photon index (Γ) is 1.46 in the case of compact NSDs while the case of extended NSDs predict it to be 1.52.

Type-1 (T1), CN, and CK such that it produces the best fit to the observed CXB spectrum.

The predicted CXB spectra are shown in Fig. 4.4. The shaded regions are the uncertainty in the observed CXB spectrum. The blue-star curve represents the first case without any contributions of obscured quasars ($f_{2,Q} = 0.0$). The high energy part of spectrum matches the observation which is due to the selection of a particular energy cutoff E_c. The spectrum is predicted lower in general, but the converse is true for $E < 3.0$ keV. Straightaway, we can find the required contribution of "quasar-like" AGNs in order to predict the observed CXB spectrum. The green-dashed curve shows that at least 40 per cent of such CK AGNs ($f_{\mathrm{CK},Q}$) along with 0.4 and 0.2 fractions of CN and T1 "quasars-like" AGNs, respectively are required in order to produce the spectrum within observed uncertainty. The 0.2, 0.2, and 0.6 fractions of T1, CN, and CK yields the best matched spectrum which fits very well with the observed one. The 2-10 keV photon index is 1.49 which is consistent with the observed value, 1.4-1.54 (Marshall et al., 1980; De Luca & Molendi, 2004; Moretti et al., 2009; Cappelluti et al., 2017).

We also explore the effect of compact and extended NSDs on CXB spectrum which are illustrated by red-dash-dotted and blue-dashed curves in Fig. 4.5, respectively. The NSDs with R_{out} equal 60 pc and 120 pc are considered as compact, while the extended NSDs are referred to the one with the size of 180 pc and 240 pc. A sample with either type of NSDs produces the CXB peak (20-30 keV) within the observational uncertainty; however, the NSDs with a smaller size are more favorable. The compact and extensive NSDs predict the photon index of 2-10 keV to be 1.46 and 1.52, respectively which are still in good agreement with observations (Marshall et al., 1980; De Luca & Molendi, 2004; Moretti et al., 2009; Cappelluti et al., 2017).

4.4.3 AGN Number Counts

A widely used physical quantity in studying the cosmic X-ray background is the AGN number counts per unit area N (e.g., Brandt et al., 2001; Bauer et al., 2004; Kim et al.,

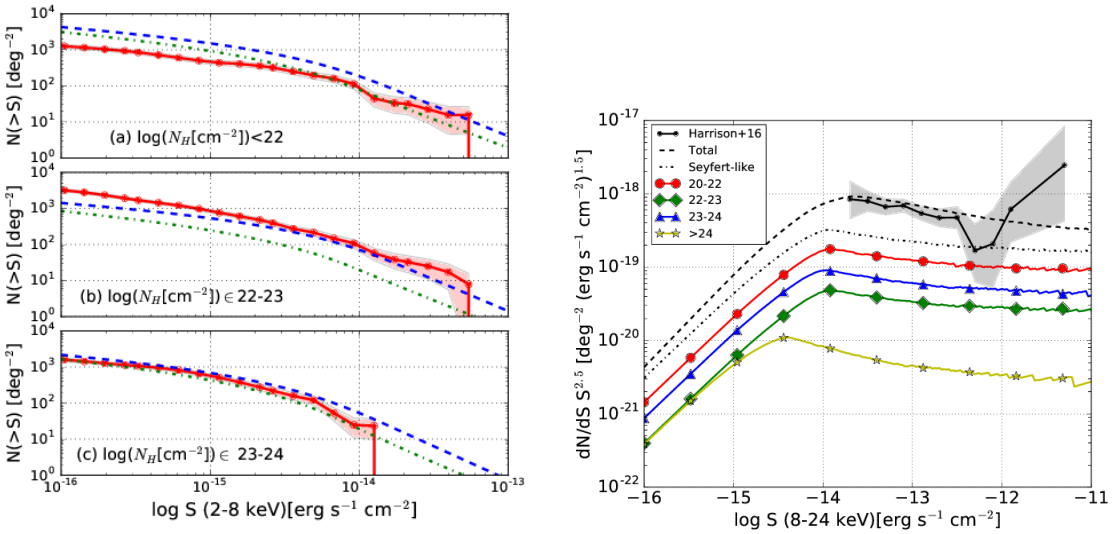

Figure 4.6: *Left:* Figure illustrates the number counts (N) of unobscured, moderately obscured, and heavily obscured AGNs in 2-8 keV bands through panel (a), (b), and (c) respectively. The number counts of moderately obscured AGNs at high energy flux (S) and the heavily obscured AGNs are in fair agreement with the observational data from CDF-S (Lehmer et al., 2012). The green-dash-solid shows the number counts of "Seyfert-like" AGNs which are obscured by the $N_{\rm H}$ distributions associated with NSDs. The blue-dashed curve shows the total number counts which also includes the contributions from quasars (20 per cent CN and 60 per cent CK). *Right:* The total differential AGN number counts in 8-24 keV band (black-dashed curve) are shown in this panel which agrees with the observational sample of *NuSTAR* (Harrison et al., 2016). The panel also provides the prediction of differential number counts of AGNs in many obscuration bands associated with the "Seyfert-like" AGNs. Their total differential number counts are shown with the black-dash-dotted curve. The figure also illustrates that contribution from quasars is important in order to match the observations.

2007; Georgakakis et al., 2008; Lehmer et al., 2012; Harrison et al., 2016). Therefore, we predict the AGN number counts in 2-8 keV and 8-24 keV bands for the case of best matched CXB spectrum with the observational one (i.e., $f_{2,Q} = 0.8$). Afterward, they are compared against the observations made by 4 Ms *Chandra* Deep Field-South (CDF-S) survey and *NuSTAR*. The left panel of Fig. 4.6 shows the predicted AGN number counts in 2-8 keV as a function of energy flux (S) where panels (a), (b), and (c) are sorted by a range of column density. The red curve represents the observed number counts and the shaded area is observational uncertainty (Lehmer et al., 2012). The AGN number counts with $L_{2-10\mathrm{keV}} < 10^{44}$ erg s^{-1} are shown in green-dash-dotted curve and the blue-dashed show the total number of AGN number counts. The number counts of unobscured AGNs (top-left panel) is overestimated even with the exclusion contribution from quasars. The obscured AGN number counts in $22 \leq \log(N_{\mathrm{H}}[\mathrm{cm}^{-2}]) < 23$ range is underestimated. With the inclusion of quasars contribution, the number counts fits the observed ones for high energy flux, but it is still lower for $S < 10^{-14.7}$ erg s^{-1} cm^{-2}. For heavily obscured AGN (10^{23}-10^{24} cm^{-2}), the contribution from quasars is very small and the AGN number counts are in fair agreement with observations (Lehmer et al., 2012) as shown in bottom-left panel of Fig. 4.6. This suggests that the 2D NSD theory produces the correct form of N_{H} distribution for heavily obscured AGNs in Seyfert galaxies.

A major source for overestimating the unobscured AGNs could be an exclusion of galaxy-scale obscuration. The CXB model only includes the obscuring medium which resides within a couple of hundred parsec scale (NSDs). Inclusion of galaxy-scale obscuration would produce a better match with observations for both unobscured AGNs and weakly-obscured AGNs (middle-left panel of Fig. 4.6) since this will shift some of the AGNs number counts from unobscured AGNs bin (top-left panel of Fig. 4.6) to $22 \leq \log(N_{\mathrm{H}}[\mathrm{cm}^{-2}]) < 23$ bin. Other possible sources for discrepancy include cosmic variance in observational data (Somerville et al., 2004) and a first-order estimate for N_{H} based on energy band ratios (Lehmer et al., 2012).

The right panel of Fig. 4.6 exhibits the differential number counts (dN/dS) in 8-24 keV band and are compared against the *NuSTAR* observation (e.g., Harrison et al., 2016). The black-solid line represents the observational data with uncertainty in shaded area and this is in fair agreement with the predicted total differential AGN number counts (black-dashed line) which also includes the quasar contribution. The black-dash-dotted curve shows the total differential counts of only "Seyfert-like" AGNs (associated with NSDs) which alone are not sufficient enough to produce the observed ones. The red-circle, green-diamond, blue-triangle, and yellow-star curves represent "Seyfert-like" AGNs ($L_{2-10\mathrm{keV}} < 10^{44}$ erg s^{-1}) with the obscuration in the range of $\log(N_{\mathrm{H}}[\mathrm{cm}^{-2}]) \in$ 20-22, 22-23, 23-24, $>$24, respectively. The figure suggests that the unobscured differential counts dominate the entire flux range. Furthermore, the differential counts of AGNs with 10^{23}-10^{24} cm^{-2} range dominates the sample of obscured AGNs.

4.5 Discussion

Unlike previous CXB models (Ueda et al., 2003; Treister & Urry, 2005; Ballantyne et al., 2006b; Gilli et al., 2007), we include redshift-dependent distribution of column density $W_{N_{\mathrm{H}}}(z, N_{\mathrm{H}})$ and the reflection parameter $R_f(z)$ motivated from a physical model of NSDs in modeling of the CXB. This CXB model comprises of a diverse evolution of CN AGNs (e.g., $\delta = 1.2$) and CK AGNs (e.g., $\delta = 1.45$). However, the predicted CXB spectrum mainly due to the 2D NSD models is lower comparison to the observed spectrum. This is not surprising for many reasons. The CXB traces an entire history of AGNs from low to high redshift. NSDs are more viable source of the AGN obscuration at the intermediate redshift (Ballantyne, 2008; Gohil & Ballantyne, 2017). Moreover, there are also other physical mechanisms which are not included in this modeling and they can play an important role in AGN obscuration such as the magnetic field, outflow, and extreme high Mach number flow (shock wave regions). For instance, outflows are observed in many star-forming galaxies (Tremonti et al., 2007; Heckman et al., 2011; Diamond-Stanic et al., 2012) which can re-

duce the amount of obscuration through removal of gas. Besides the "Seyfert-like" AGNs, very luminous quasars are also observed to be obscured (Iwasawa et al., 2012; Buchner et al., 2015). The obscuration in their environment may be driven by different mechanisms than the star-forming regions in "Seyfert-like" AGNs. The assumptions such as the evolution of gas fraction at hundreds of parsec scale being same as the galaxy gas fraction, and the random selection of $R_{\rm out}$ and m can also contribute to errors in final results.

4.5.1 Comparison with observed fraction of obscured quasars

Our work suggests that 80 per cent of the quasars need to be obscured in order to produce the observed CXB spectrum besides the $N_{\rm H}$ distribution associated with the dusty starburst discs. This value is in fair agreement with the observational work done by many groups. Buchner et al. (2015) find that the cosmic averaged obscured fraction of AGNs with X-ray luminosity $L_x > 10^{43}$ erg s^{-1} is 0.72-0.81 using 2000 sample size from a various surveys. Iwasawa et al. (2012) detect ≈0.75 fraction of obscured "quasar-like" AGNs in deep XMM-CDFS survey sample at $z > 1.7$. Schawinski et al. (2012) estimate ~ 90 per cent of observed quasars in $1 < z < 3$ by deep HST WFC3/IR imaging to be heavily obscured. Using Chandra Deep Field South (CDF-S) data in 4-7 keV band, Wang et al. (2007) find that 71 ± 19 per cent of quasars are obscured (Type-2). Furthermore, a majority of these "quasar-like" AGNs are predicted to be CK. Our CXB model requires 40 (lower limit) to 60 per cent (best match) of these high luminous AGNs to be CK. Similar conclusions are also reached by many groups (e.g., Martínez-Sansigre et al., 2007; Draper & Ballantyne, 2010). Martínez-Sansigre et al. (2007) finds that 10 out of 12 observed quasars at $z > 1.7$ are Type-2 and ~ 67 per cent of them are likely to be Compton-thick. Based on the analysis of Chandra and XMM-Newton data, Jia et al. (2013) estimate the fraction of Compton-thick in Type-2 quasars sample to be 46 to 64 per cent at $z < 0.73$. By studying the sample of 33 mid-IR luminous quasars at $1 < z < 3$, Del Moro et al. (2015) find that 67 to 80 per cent of quasars are Type-2 and the $f_{\rm CK}$ was constraint to be 24-48 per cent. Thus, the predicted

fractions of obscured quasars are impressively in fine agreement with observations.

4.5.2 Evolution of the obscured AGNs fraction

The evolution of AGN fractions is expected to be overestimated by the NSD models due to several reasons mentioned above. Therefore, the predicted AGN fractions should be taken as a lower limit. We again emphasize that the AGN fractions are computed with respect to the entire domain of a sample, $N_{\rm H} \in [0.0, 10^{26}]$ cm^{-2}; for instance,

$$f_2 \equiv \frac{N(22 \leq \log[N_{\rm H}(\text{cm}^{-2})] \leq 26)}{N(20 \leq \log[N_{\rm H}(\text{cm}^{-2})] \leq 26)}, \tag{4.26}$$

where N is the number of obscured AGNs in that given $N_{\rm H}$ bin. The power-law evolution of obscured AGNs $f_2 \propto (1+z)^{\delta}$ associated with the dusty starburst discs ("Seyfert-like" AGNs) is governed by $\delta = 1.2$ for $z < 2$. Many groups have predicted δ in 0.4-0.5 range (Ballantyne et al., 2006b; Treister et al., 2006; Ueda et al., 2014; Liu et al., 2017). Since, the number density of "quasar-like" AGNs peaks at $z \sim 2-3$ (Ueda et al., 2003; Barger et al., 2005; Silverman et al., 2008; Yencho et al., 2009; Aird et al., 2012), $f_{2,Q}$ can play an important role at $z \sim 2$. Therefore, if the quasar contribution ($f_{2,Q} = 0.8$) is added to the obscured AGN fraction at $z = 2$ and one requires δ to be 0.45, then the estimated f_2 is approximately 40 per cent in the local universe. This serves as the lower limit since the presence of outflows at higher redshift are more likely to remove gas from a system which will reduce the amount of obscuration resulting in lower δ (<0.45). However, the estimated $f_2(z=0) = 0.4$ is lower than the work of Liu et al. (2017) who finds that $f_{\rm CN}$ by itself is around 40 per cent in local universe. Moreover, the power-index of $f_{\rm CN}$ evolution is observed to be steeper ($\delta = 0.6$) than the power-index of $f_{\rm CK}$ AGNs ($\delta = 0.45$) (Liu et al., 2017). However, we find an opposite conclusion in scenario of AGNs associated with NSDs. In that case, the $f_{\rm CK}$ has a stronger evolution with comparison to $f_{\rm CN}$.

4.5.3 Evolution of Compton-thick fraction and reflection parameter

Analysis similar to the above section can also be done for the evolution of the CK fraction $f_{\rm CK} \propto (1+z)^{\delta}$. With the contributions from "quasars-like" AGNs, $f_{2,Q}$ corresponds to ~ 37 per cent at $z = 2$. The recent studies have found 0.33-0.46 fraction of CK AGNs in local universe (Brightman & Ueda, 2012; Buchner et al., 2015; Lansbury et al., 2017). If we take the observed value of $f_{\rm CK}$ in local universe to be around 35 per cent (Brightman & Ueda, 2012; Buchner et al., 2015), then a very weak evolution, $\delta = 0.05$, is predicted, which is consistent with the conclusion of Brightman & Ueda (2012) and Buchner et al. (2015). However, other groups have also inferred $f_2 \sim 20$ per cent in local universe from observations (Akylas & Georgantopoulos, 2009; Brightman & Nandra, 2011a,b; Burlon et al., 2011). In that case, the f_2 is predicted to evolve with $\delta \sim 0.56$. Using *NuSTAR* extragalactic survey data, Del Moro et al. (2017) find that the reflection (R_f) is around 0.5 for AGNs with $\Gamma = 1.8$ and Zappacosta et al. (submitted, 2017) find the mean value to be $R_f = 0.41$ at $0 < z < 2.1$. These values are in fair agreement with our introduced definition of reflection quantity (R_f). The R_f associated with the NSDs rises from 0.13 at $z = 0$ to 0.47 at $z = 2.0$ and 0.58 at $z = 4.0$.

4.6 Conclusion

To summarize, we statistically evolve the $N_{\rm H}$ distribution ($W_{N_{\rm H}}(z, N_{\rm H})$) using redshift dependent distribution of the input parameters: the gas fraction $f_{\rm g,out}$ (Eq. 4.19) and the black hole mass $M_{\rm bh}$ (Eq. 4.6). Then, the $N_{\rm H}(z)$ is utilized to predict the evolution of Compton thin and CK AGNs. In addition, by utilizing the $W_{N_{\rm H}}(z, N_{\rm H})$ (Eq. 4.24), we predict the CXB spectrum and the AGN number counts in 2-10 keV and 8-24 keV bands. Below we summarize our main findings:

- The obscured AGNs show a strong positive evolution with redshift up to $z = 2$ and it is weakened afterward. The main driver of the evolution is gas-fraction in galaxies.

- The fraction of CN and CK AGNs do not evolve $\propto (1+z)^{\delta}$ in the same manner. The predicted power-law index of evolution δ is 1.12 and 1.45 for $f_{\rm CN}$ and $f_{\rm CK}$ for $z < 2.0$ which are associated solely with the dusty starburst regions. Moreover, the ratio of $f_{\rm CK}$ to $f_{\rm CN}$ is always less than 1.

- Within the sample of obscured AGNs, the distribution column density along the line of sight peaks near 10^{23} cm^{-2} independently of redshift (e.g., Burlon et al., 2011; Ueda et al., 2014; Buchner et al., 2015; Sazonov et al., 2015).

- Based on the *NuSTAR* extragalactic survey sample, Del Moro et al. (2017) infer the reflection parameter $R_f = 0.41$ for the AGNs with $\Gamma = 1.8$ and Zappacosta et al. (submitted, 2017) compute the mean R_f equal 0.41 for sample at redshift $0 < z < 2.1$. These values are within the range of modeled R_f associated with the NSDs: the reflection parameter increases from 0.13 at z = 0 to 0.58 at z = 4.0.

- The evolution of AGN environment with redshift depends on obscuring medium. As the amount of obscuration increases, the AGN fraction of a given $N_{\rm H}$ bin in local universe deviates more with comparison to higher redshift $z = 2$.

- The AGNs with starburst regions alone are not sufficient to produce the observed CXB peak. In addition, 20, 20, and 60 per cent of unobscured, CN, and CK type of high luminous AGNs (quasars) are required, respectively. The predicted lower limit on CK quasars from the CXB model is 40 per cent.

- The predicted peak of SED has a better match with observation as NSDs get more compact. Compact NSDs produce a 1.46 photon index in 2-10 keV band, while the extended NSDs favor higher photon index ~ 1.52 (Marshall et al., 1980; De Luca & Molendi, 2004; Moretti et al., 2009; Cappelluti et al., 2017).

- With comparison to the observational sample of CDF-S (Lehmer et al., 2012), the predicted number counts of unobscured AGNs in 2-8 keV band are overestimated.

However, the number counts of low obscured AGNs at higher flux ($S > 10^{14.7}$ erg s^{-1} cm^{-2}) and moderately obscured AGNs are in fair agreement. The estimated total AGN number counts in 8-24 keV band are also consistent with the *NuSTAR* observations (Harrison et al., 2016).

- The predicted fraction of obscured "quasar-like" AGNs is in reasonable agreement with observations. This supports the possibility that nuclear starburst discs can be an important source of obscuration in Seyfert galaxies at intermediate redshift. (Ballantyne, 2008; Gohil & Ballantyne, 2017).

CHAPTER 5

THE EFFECTS OF DUST ON THE EQUIVALENT WIDTH OF THE FE Kα LINE IN AGNS

Obscured AGNs provide an opportunity to study the material surrounding the central engine. Geometric and physical constraints on the absorber can be deduced from the reprocessed AGN emission. In particular, the obscuring gas may reprocess the nuclear X-ray emission producing a narrow Fe Kα line and a Compton reflection hump. In recent years, models of the X-ray reflection from an obscuring torus have been computed; however, although the reflecting gas may be dusty, the models do not yet take into account the effects of dust on the predicted spectrum. We study this problem by analyzing two sets of models, with and without the presence of dust, using the one dimensional photoionization code Cloudy. The calculations are performed for a range of column densities ($22 < \log[N_H(\mathrm{cm}^{-2})] < 24.5$) and hydrogen densities ($6 < \log[n_H(\mathrm{cm}^{-3})] < 8$). The calculations show the presence of dust can enhance the Fe Kα equivalent width (EW) in the reflected spectrum by factors up to ≈ 8 for Compton thick (CK) gas and a typical ISM grain size distribution. The enhancement in EW with respect to the reflection continuum is due to the reduction in the reflected continuum intensity caused by the anisotropic scattering behaviour of dust grains. This effect will be most relevant for reflection from distant, predominately neutral gas, and is a possible explanation for AGNs which show a strong Fe Kα EW and a relatively weak reflection continuum. Our results show it is an important to take into account dust while modeling the X-ray reflection spectrum, and that inferring a CK column density from an observed Fe Kα EW may not always be valid. Multi-dimensional models are needed to fully explore the magnitude of the effect.

5.1 Introduction

All active galactic nuclei (AGN) are powered by gas accreting onto a central supermassive black hole (e.g. Balbus, 2003), a process which emits a significant amount of energy across the electromagnetic spectrum. Interestingly, a significant number of AGNs show the presence of local obscuration (Comastri, 2004) at distances $\sim$ 1-10 pc from the central engine (e.g. Antonucci, 1993; Urry & Padovani, 1995). The nature and origin of the absorbing gas is largely unknown but the gas presents an unique opportunity to study material as it transitions from the galaxy to the AGN environment.

Superimposed onto the typical $\Gamma \sim$ 1.8-2 X-ray power-law in AGNs (e.g. Dadina, 2008; Beckmann et al., 2009; Corral et al., 2011) is an Fe Kα line (e.g. Nandra & Pounds, 1994; Ebisawa et al., 1996). The narrow component of the line is observed in a large number of objects (Yaqoob et al., 2001; Kaspi et al., 2001), even in many high-redshift samples (Brusa et al., 2005; Corral et al., 2008; Chaudhary et al., 2012; Iwasawa et al., 2012), and the width of the line indicates that it may originate in the obscuring material (e.g. Yaqoob & Padmanabhan, 2004; Shu et al., 2010). Moreover, the equivalent width (EW) of the Fe Kα line can be as large as several keV (e.g. Levenson et al., 2006) which may be a signature of Compton thick (CK) gas (e.g. Murphy & Yaqoob, 2009). A correlation between the Fe Kα EW and the line-of-sight column density is observed for columns $> 10^{23}$ cm^{-2} indicating that the line is often produced by CK gas in the AGN environment (e.g. Guainazzi et al., 2005; Fukazawa et al., 2010). Thus, the Fe Kα line can be used as an important proxy to study the properties of the obscuring gas around AGNs.

In recent years, there have been several Monte-Carlo models of X-ray reprocessing from a CK torus (e.g. Ikeda et al., 2009; Murphy & Yaqoob, 2009; Brightman & Nandra, 2011a). However, all of these calculations omit dust from the models which in many cases may be present in the X-ray absorbing gas (Jaffe et al., 2004; Prieto et al., 2004, 2005; Meisenheimer et al., 2007; Tristram et al., 2007; Raban et al., 2009). As these models are

now being used to determine the gross properties of the obscuring material, it is important to consider the effects of dust on the X-ray reflection spectrum. Here, we use Cloudy models to show that the inclusion of dust in the distant obscuring gas may have an important impact on the reflected Fe Kα EW. Sect. 5.2 describes the geometrical set up of the models and the calculation procedure. Sect. 5.3 describes the results, and Sect. 5.4 discusses the implications of this study.

5.2 Calculations

The photo-ionization code Cloudy v13.02 (Ferland et al., 2013), is utilized to study the impact of dust on the reflected iron Kα line. Although the calculations with Cloudy are one dimensional, the code includes multiple grain species with a realistic size distribution (e.g. Mathis et al., 1977) as well as a comprehensive treatment of grain physics (Weingartner & Draine, 2001; van Hoof et al., 2004; Weingartner et al., 2006), i.e. scattering and absorption of dust based on its size and shape. All calculations assume an AGN spectrum with an intrinsic luminosity of 10^{43} erg s^{-1} in the 2-10 keV band and a typical photon index of 1.9 (e.g. Beckmann et al., 2009). The optical to UV spectrum is characterized by α_{ox} = -1.4 (e.g. Zamorani et al., 1981), a UV slope of -0.5 (e.g. Francis, 1993; Elvis et al., 1994), and a blackbody temperature of 1.4×10^5 K (appropriate for a black hole of 10^7 $M_\odot$ accreting at 10% of its Eddington rate). The gas irradiated by this spectrum has an uniform hydrogen density, n_H, extended radially outward until it reaches a specified column density, N_H. The covering factor is fixed at 0.67, equivalent to a 30° opening angle, and calculations are performed for $22 < \log[N_H(\mathrm{cm}^{-2})] < 24.5$ (with 0.25 dex spacing), and $6 < \log[n_H(\mathrm{cm}^{-3})] < 8$ (with a spacing of 1 dex).

To study the effects of dust, two sets of models are computed. The first has gas with solar abundances (Grevesse et al., 2011) and no dust (ND), while the second includes ISM dust (WD) (Mathis et al., 1977; Cowie & Songaila, 1986; Savage & Sembach, 1996; Meyer et al., 1998; Snow Jr & Dodgen, 1980). In order to isolate the effects of dust on the reflected

spectra, the abundances in the gas in the WD models are kept at solar, but the metal abundances are reduced using the depletion factors of Cowie & Songaila (1986), and Jenkins (1987) and the gas-to-dust ratio was kept at 151. To check the self consistency of the two models, the abundances of each element are added and the overall abundance of elements is consistent within 0.05% in both ND and WD models; however, the Fe abundance in the WD models is 5% higher than ND models.

At high AGN luminosities grains may reach the sublimation temperature and return the metals back to the gas phase. This effect is not easily treated by Cloudy, so the inner radius of the illuminated gas is fixed at a distance of 10 pc away from the AGN. At this distance the dust temperature inside the illuminated gas is always below the sublimation temperature of the grains. As a further check on the choice of parameters, the reprocessed 12μm luminosity of the WD models is compared against the one expected from the 12 μm-X-ray luminosity relationship (Gandhi et al., 2009). Depending on n_H, the simulated 12μm luminosities are 1.2-1.5 times larger than the observationally predicted one. Thus, our simple dusty gas setup will be a reasonable model for the average properties of a Seyfert-type AGN.

Finally, to study the effects of dust on the Fe Kα emission line, the equivalent width (EW) of the line is analyzed as a function of N_H and n_H for both sets of models. The EW is defined as the ratio of the intensity of the Fe Kα emission line ($I_{FeK\alpha}$) to the reflected continuum at the line energy (I_c) multiplied by the energy bin width (ΔE):

$$EW = \frac{I_{FeK\alpha}}{I_c} \times \Delta E. \tag{5.1}$$

Ideally, I_c should be measured at 6.4 keV, but because of the presence of the emission line, it is difficult to determine I_c at that energy. Therefore, I_c is measured at 6.3 keV as there are no predicted emission lines at that energy. Using a different I_c between 6.3 keV and 6.5 keV leads to only very small changes in the EW. Rather than measuring $I_{FeK\alpha}$ from the predicted spectrum, we use the emergent line intensities reported in the Cloudy output

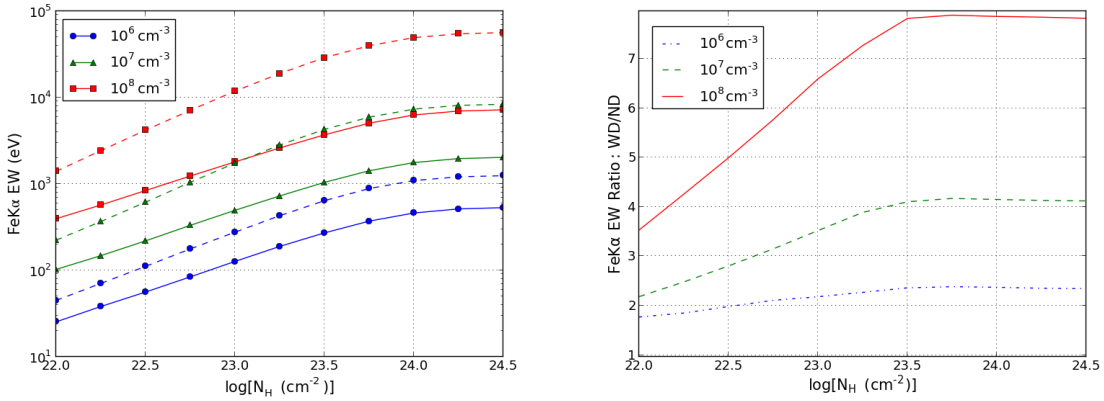

Figure 5.1: $Left$: Solid and dashed lines plot the EW versus N_H for the case of ND and WD respectively. The EW increases with N_H and n_H in both ND and WD cases. $Right$: The Fe Kα EW gets significantly enhanced in the WD models with a factor that depends strongly on n_H.

since it takes into account the effects of extinction on the line intensities. In the ND models, the Fe Kα emission line comes from cold gas (e.g George & Fabian, 1991; Weaver et al., 2001; Page et al., 2004; Yaqoob & Padmanabhan, 2004; Zhou & Wang, 2004; Jiang et al., 2006; Levenson et al., 2006), and in the WD models it comes from both cold gas and grains which are added to obtain $I_{FeK\alpha}$. The cold Fe Kα fluorescence line defined by Cloudy is actually emitted between 6.4 to 6.424 keV for Fe I to Fe XIV (House, 1969); therefore, we set ΔE = 24 eV in eq. 1. As a consistency check, the EW calculation was compared with the result from Ikeda et al. (2009). Our results predict the ND Fe Kα EW to be ≈ 1.8 keV for N_H = 10^{24} cm^{-2} and n_H = 10^7 cm^{-3} which is slightly lower than the EW $\approx$ 2 keV predicted from the Monte Carlo simulations of Ikeda et al. (2009). However, given the differences in computational techniques and physical setup, this difference is adequate. In addition, we are focused on the relative changes in the EW when dust is included in the irradiated gas.

5.3 Results

Fig. 5.1 shows how the Fe Kα EW depends on N_H and n_H. The left panel of Fig. 5.1, shows that the Fe Kα EW increases with N_H for Compton thin gas ($10^{22} < N_H < 10^{24}$ cm^{-2}). Such a dependency is expected since the amount of illuminated gas increases with N_H and this produces more Fe Kα emission. For Compton thick gas ($N_H > 10^{24}$ cm^{-2}), the amount of gas irradiated by X-rays is limited by Compton scattering and the Fe Kα EW is fairly invariant with N_H. In addition, the EW of Fe Kα increases with n_H in both the ND and WD models due to the rise in total opacity with n_H. This reduces I_c and therefore increases the EW.

Our calculation shows that the presence of dust may significantly enhance the Fe Kα EW. The right panel of Fig. 5.1 shows that the EW of the Fe Kα line is increased by a factor of 2.5 for n_H = 10^6 cm^{-3} (for $N_H > 10^{24}$ cm^{-2}) due to presence of grains. For n_H = 10^7 and 10^8 cm^{-3}, the EW is enhanced by a factor of 4.1 and 8, respectively. To illustrate the reason for this enhancement, Fig. 5.2 plots I_c and $I_{FeK\alpha}$ ratios vs. N_H. This figure clearly shows that the change in EW between WD and ND is due to the reduction in the continuum and not because of a change in $I_{FeK\alpha}$. ($I_{FeK\alpha}$ does slightly increase due to the presence of grains, but this is largely due to the abundances in the models ND and WD not being perfectly self consistent; the Fe abundance is 5% higher in WD models. Therefore, it is expected to have slightly more Fe Kα emission line in the case of WD.)

Fig. 5.2 shows the increase in EW of Fe Kα when reflected by dusty gas is due to a reduced continuum. This suppressed reflection continuum is due to the reduction in backscattering opacity (κ_s) in dusty gas. Fig. 5.3 shows how κ_s varies inside the column of an illuminated gas as a function of depth for WD and ND models for N_H = 10^{24} cm^{-2} and n_H = 10^7 cm^{-3}. At depths $> 10^{13}$ cm, H is no longer ionized and dust contributes significantly to the scattering opacity; therefore, κ_s decreases significantly deep inside the cloud in WD models compared to the ND models. This drop in κ_s due to dust is because

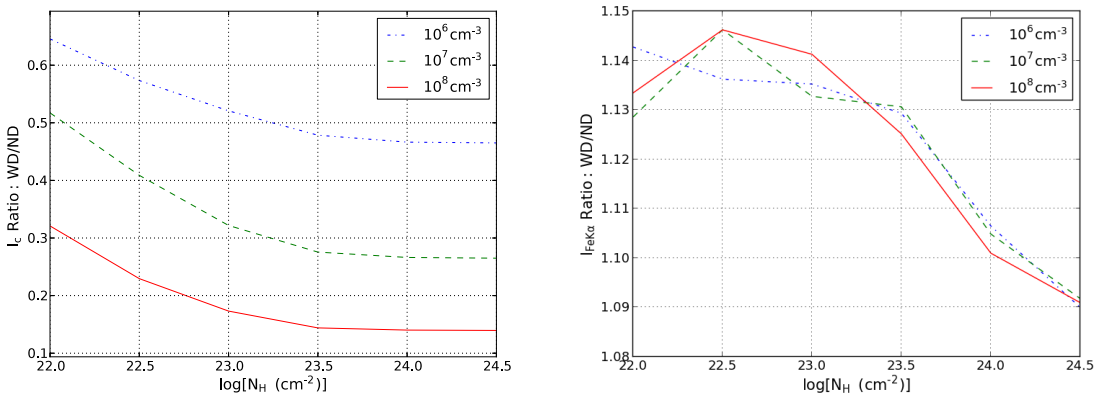

Figure 5.2: $Left$: The effect of dust on I_c. As n_H increases, the effects of dust grows and the I_c ratio significantly decreases and is therefore responsible for the increased Fe Kα EW. $Right$: The presence of grain only slightly increases the Fe Kα intensity, but this has a very small effect on its EW.

scattering from grains is highly anisotropic and favor scattering in the forward direction by an amount depending on the size, structure and shape of the grains (Draine, 2003). Since the wavelength of X-rays is smaller than the size of most grains, there is only a weak coupling between the radiation and the grain leading to anisotropic scattering. As the Fe EW is computed using the backscattered continuum, this anisotropic scattering will reduce the backscattered intensity for WD models and thus the EW increases.

It has been proposed that dust in an AGN environment has fewer small grains than the typical ISM distribution (Maiolino, 2001). As k_s is proportional to grain size (Hayakawa, 1970), a grain size distribution deficient in small grains will likely produce a stronger reflection continuum and thus the Fe Kα EW will not increase as strongly as with the ISM grains. To check this effect we computed a Cloudy model (n_H=10^7 cm^{-3}, N_H = 10^{24} cm^{-2}) with Orion abundances that includes a grain size distribution deficient in small grains. The k_s from this model is overplotted on Fig. 5.3 to compare against the results from the ND and WD calculations. As expected, the Orion k_s is larger than the one using ISM grains, but still smaller than the model with no dust. The EW of the Fe Kα line is enhanced by a factor of $\approx$ 4 with the ISM grains, and by a factor of $\approx$ 2.6 with the Orion grains. Hence, the anisotropic scattering behaviour of grains may still have an observable impact on the

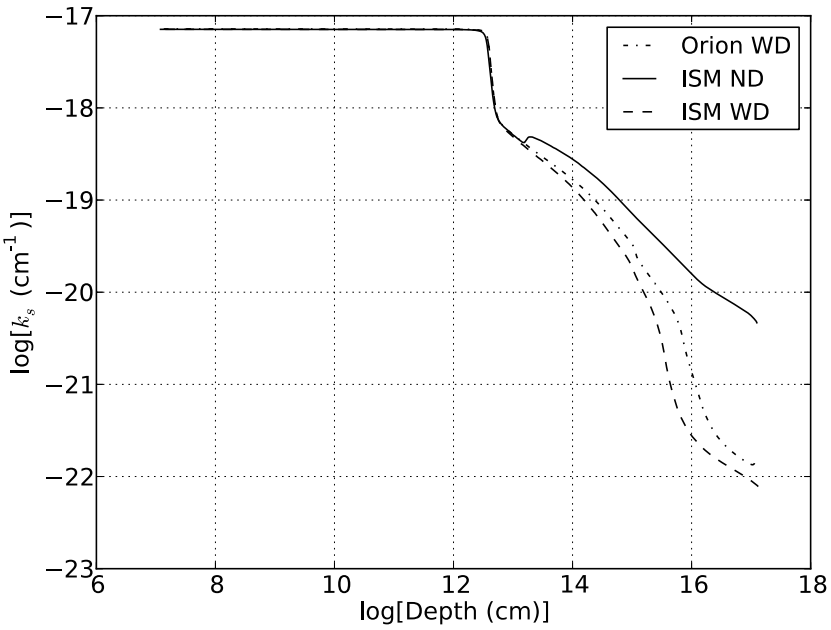

Figure 5.3: The isotropic backscattering opacity in the irradiated gas as a function of depth for the n_H = 10^7 cm^{-3} and N_H = 10^{24} cm^{-2} models. Deep inside the column of gas at depths $> 10^{13}$ cm, H recombines and the scattering is dominated by the grains which is highly anisotropic and results in lowering the backscattering opacity in the WD models. The Orion WD model shows a higher k_s than the ISM WD model due to the deficiency of small grains. However, the Orion distribution still produces a lower backscattering opacity than the ND model which corresponds to an increase in the Fe Kα EW by a factor of $\approx$ 2.6.

Fe Kα EW if the smaller grains are not present.

5.4 Discussion and Summary

Many groups have computed two dimensional X-ray reflection models for AGN torii without taking into account the effects of grains (e.g. Ikeda et al., 2009; Murphy & Yaqoob, 2009; Brightman & Nandra, 2011a). However, it is possible that distant X-ray reflectors arise from dusty gas (Jaffe et al., 2004; Prieto et al., 2004, 2005; Meisenheimer et al., 2007; Tristram et al., 2007; Raban et al., 2009). Moreover, the Fe Kα line is an important proxy to estimate the column density of distant observing gas (Ghisellini et al., 1994). Therefore, we used Cloudy to compute simple one-dimensional models of dusty gas illuminated by an AGN in order to study the effects of dust on Fe Kα emission line. We found that the presence of dust may significantly enhance the Fe Kα EW (by factors of ~ 5) in the reflection spectrum even in non-CK gas. When grains are present in the gas, scattering is anisotropic and there are less backscattered photons in the reflected continuum and the overall continuum intensity is decreased. This suggests that inferring a CK N_H from the Fe Kα EW can be precarious.

The increase in EW occurs when dust dominates k_s and therefore will be most important when the gas contains predominantly neutral hydrogen. This limits the reflecting cloud to be relatively distant from the nucleus or to have a significant density. Therefore, the Fe Kα EW enhacement may only be important for a certain subset of AGNs that exhibit infrared emission from AGN heated dust, a large Fe Kα EW, and an unusually weak Compton reflection component. For example, NGC 7213 is observed to have significant hot dust emission (Ruschel-Dutra et al., 2014), an Fe Kα EW ≈ 120 eV, and a very weak Compton reflection component (Bianchi et al., 2009; Emmanoulopoulos et al., 2013). Similary, NGC 2210 also shows strong dust emission (Hönig & Kishimoto, 2010) and is observed to have an Fe Kα EW of $\approx 35 - 200$ eV from Compton thin gas (Marinucci et al., 2014). Although a broad-line region origin for the Fe Kα line is a possibility (Bianchi et al., 2003), our

results also suggest that reprocessing from the dusty Compton thin gas in the absorber may also contribute to the Fe Kα line.

We conclude that the anisotropic scattering behavior of grains is an important mechanism to take into account when modeling X-ray reflection from torii since it may have a significant effect on the predicted Fe Kα EW. However, the effects of geometry are important. Since the scattering behavior of grains directly affects the continuum, the effects of grains depends on the viewing angle relative to the orientation of torus, therefore the true magnitude of the effect needs to be studied in multi-dimensional models. The EW of the emission line may be reduced, enhanced or unchanged since the continuum can be the transmitted spectrum, reflected spectrum, incident spectrum or their combination depending on the viewing angle.

CHAPTER 6

CONCLUSION

Many AGNs show the presence of obscuration as described in the above chapters. Moreover, the presence of dust has been observed at parsec scales (Raban et al., 2009; Tristram et al., 2007). Therefore, in 2014-2015, I conducted research on the equivalent width (EW) of an emission line produced by a parsec scale dusty medium. I explored the effect of dust on the Fe Kα emission line produced by a one dimensional dusty absorber in AGNs. The correlation between the Fe Kα line and the column density $N_{\rm H}$ has been observed for $N_{\rm H} > 10^{23}$ cm^{-2} (Guainazzi et al., 2005; Fukazawa et al., 2011). Thus, the Fe Kα line can be used as a proxy to study the properties of the obscuring gas around AGNs. I utilized the CLOUDY code, one dimensional photo-ionization code, to study the interaction between the AGN spectrum and a column of gas. The results show that the presence of dust enhances the equivalent width of Fe Kα line due to the anisotropic scattering of dust which in turn decreases the reflected continuum intensity (Gohil & Ballantyne, 2015). The analysis suggests that this is expected since the wavelength of the continuum (near emission; ~ 1.92 Angstrom) is much more smaller than the size of grains. In other words, the dust grains are fairly "transparent" to the continuum. Therefore, the reflected continuum decreases when dust is included. Since the EW is inversely proportional to the continuum, it can be enhanced by factors up to ~ 8 depending on the density of a cloud. However, a geometry of a torus plays an important role in reflection of the continuum. Therefore, it will be interesting to carry out multi-dimensional modeling in the future and study the importance of dust in parsec absorbers.

I have also worked on the two-dimensional (2D) computational modeling of dusty nuclear starburst disks around a central black hole and studied its impact on the AGN obscu-

ration. Modeling of these regions can be extremely complicated since it involves radiation transport and also dust physics, which is not well understood due to the various size and composition of grains. Moreover, modeling also involves computational challenges, such as solving a non-linear second order boundary value problem and a coupled hydrostatic balance, radiative transfer, and energy balance equations using an iterative method. In my recent work (Gohil & Ballantyne, 2017), I computed the 2D structure of NSDs by solving these coupled equations with the iterative algorithm that I developed. By utilizing this method, a total of 192 NSDs were computed under various conditions across the input parameter space. The predicted fraction of Compton-thick (CK) AGNs, the ratio of CK to Compton-thin AGNs, and the peak of $N_{\rm H}$ distribution from this work were in fair agreement with observations.

Besides the previous projects, I also studied the evolution of the AGN obscuration using the 2D modeled NSDs and the impact of this obscuration on the cosmic X-ray background. The first step was to compute the dependence of $N_{\rm H}$ distribution on redshift. I took a statistical approach where the $N_{\rm H}$ distribution is weighted according to the observationally motivated distribution functions of modeling input parameters. Since these functions have redshift dependence, one can compute the evolution of $N_{\rm H}$ distribution. The recent conclusion and findings of my work are as follows: (1) the amount of obscuration increases with redshift, (2) the $N_{\rm H}$ distribution always peaks near 10^{23} cm^{-2}, and (3) the evolution of obscuration is stronger with the increasing $N_{\rm H}$ (Gohil & Ballantyne, 2018). I then used the evolved $N_{\rm H}$ distribution to predict the AGN number counts as well as the cosmic X-ray background (Gohil & Ballantyne, 2018). The result shows that $\sim 80\%$ of obscured quasars are required in order to produce the observed cosmic X-ray background. Moreover, 60% of quasars are needed to be Compton-thick.

What is the fate of nuclear starburst disks? That is also an important question to explore. One of the possibilities is nuclear star clusters (NSCs). NSCs are observed in 70%

of spheroidal galaxies (Côté et al., 2006) and in 75% of late-type disk galaxies (Walcher et al., 2005) with the size around 2-5 pc (Geha et al., 2002; Böker et al., 2004; Côté et al., 2006). Since the NSDs have a compact starburst region at the parsec scale, they can be the potential progenitors of NSCs. Currently, we plan to study the remnants of NSDs by evolving stellar population via stellar population synthesis code and predict the observables such as the color-magnitude diagrams and spectrum which can be tested against observations in the local universe. In addition to this project, I am also working with Prof. Carol Paty (professor in School of Earth and Atmospheric Sciences) on the interaction of an exoplanet in the habitable zone with its M-dwarf host star. About 75% of stars in the Galaxy are M-dwarf and several exoplanets have been found around them (www.exoplanets.eu). The habitability around these stars is not trivial since they have an enhanced stellar activity in comparison with the Sun and also emit a large flux of the UV radiation. On the other hand, the work of Kay et al. (2016) suggests that an exoplanet with a higher inclination angle has a lower chance of being impacted by stellar wind. Therefore, we are investigating the dynamical interaction between the magnetosphere of an exoplanet and the stellar wind through multifluid magnetohydrodynamic (MHD) model. The plan is to study the occurrence rate of magnetic storms on the exoplanet and their impact on habitability, which is also dependent on inclination angle.

Well, a Ph.D. is just one stop, but research is a never-ending process.....

Appendices

APPENDIX A

CLOUDY INPUT FILE

```
def fwrite(logtemp,logN):
    pre="N"+str(logN)+"T"
    fin=pre+str(logtemp)+'.in'
    f = open(fin,"w")
    f.write("AGN T=140000k, a(ox)=-1.4 a(uv)=-0.5 a(x)=-0.7\n")
    f.write("energy density 0.0001K linear\n")
    f.write("cosmic rays background\n")
    linearT=pow(10,logtemp)
    if (linearT<1400):
        f.write("abundances Orion \n")
        f.write('constant temperature '+str(logtemp)+' K\n')
        f.write('constant grain temperature '+str(logtemp)+' K\n')


    if (linearT>=1400) and (linearT<=1750):
        f.write("abundances Orion no grains\n")
        f.write("grains Orion graphite\n")
        f.write('constant temperature '+str(logtemp)+' K\n')
        f.write('constant grain temperature '+str(logtemp)+' K\n')

    if (linearT>1750):
        f.write("abundances Orion no grains\n")
        f.write('constant temperature '+str(logtemp)+' K\n')

    f.write('hden '+str(logN)+'\n')
    f.write("stop zone 1\n")
    f.write("stop temperature 5k linear\n")
    f.write("iterate to convergence\n")
    f.write('save total opacity last ".opac" units centimeters last iteration\n')
    f.close()
    return
```

APPENDIX B

LOGARITHMIC SPACE

In some instances, the differential equation is more appropriate and easier (computationally) to solve on the logarithmic space; for example, when a domain of an independent variable has a large range (i.e from 0 to 10^5). In order to achieve the task, we will have to transfer a differential equation (second order for our purpose)

$$\frac{d^2\theta}{dt^2} = \alpha(t, \theta, \omega) \tag{B.1}$$

with BCs of

$$\theta(t = t_{min}) = \theta_0 \text{ and } \theta(t = t_{max}) = \theta_{max} \tag{B.2}$$

into the logarithmic space. Then, solve a following transformed differential equation:

$$\frac{d^2\theta}{dT^2} = f(T, \theta, \Omega) \tag{B.3}$$

where

$$T := log(t);\ \Omega := \frac{d\theta}{dT};\ \ f := \frac{d\Omega}{dT} \tag{B.4}$$

We need to know the transformation of $\omega \rightarrow \Omega$ and $\alpha \rightarrow$ f.

Transformation

$$\frac{d^2\theta}{dt^2} = \alpha(t, \theta, \omega); \quad \text{where } \omega := \frac{d\theta}{dt}$$

$$\frac{d\theta}{dt} = \frac{d\theta}{d\log(t)}\frac{d\log(t)}{dt} = \frac{d\theta}{d\log(t)}\frac{1}{t}$$

$$\frac{d\theta}{d\log(t)} = \omega t$$

$$\begin{aligned}\frac{d^2\theta}{dt^2} &= \frac{d}{dt}\Big(\frac{d\theta}{d\log(t)}\frac{1}{t}\Big) \\ &= \frac{d}{d\log(t)}\Big(\frac{d\theta}{d\log(t)}\frac{1}{t}\Big)\frac{d\log(t)}{dt} \\ &= \Big(\frac{d^2\theta}{d\log(t)^2}\frac{1}{t} + \frac{d\theta}{d\log(t)}\frac{dt^{-1}}{d\log(t)}\Big)\frac{1}{t}\end{aligned}$$

$$\begin{aligned}\frac{dt^{-1}}{d\log(t)} &= \frac{dt^{-1}}{dt}\frac{dt}{d\log(t)} \\ &= \frac{-1}{t}\Big(\frac{d\log(t)}{dt}\Big)^{-1} = \frac{-t}{t^2} = \frac{-1}{t}\end{aligned}$$

Plugging this into the equation of $\frac{d^2\theta}{dt^2}$ gives:

$$\begin{aligned}\frac{d^2\theta}{dt^2} &= \Big(\frac{d^2\theta}{d\log(t)^2}\frac{1}{t} + \frac{d\theta}{d\log(t)}\frac{-1}{t}\Big)\frac{1}{t} \\ \frac{d^2\theta}{d\log(t)^2} &= t\Big(t\frac{d^2\theta}{dt^2} + \frac{1}{t}\frac{d\theta}{d\log(t)}\Big) \\ &= t\Big(t\alpha + \omega\Big).\end{aligned}$$

Finally, we get the following transformations:

$$\Omega = \omega t$$

$$f = t(t\alpha + \omega).$$

BIBLIOGRAPHY

Achmad L., Lamers H. J. G. L. M., Pasquini L., 1997, A&A, 320, 196

Aird J., et al., 2012, The Astrophysical Journal, 746, 90

Aird J., Coil A. L., Georgakakis A., Nandra K., Barro G., Pérez-González P. G., 2015, Monthly Notices of the Royal Astronomical Society, 451, 1892

Akylas A., Georgantopoulos I., 2009, A&A, 500, 999

Akylas A., Georgantopoulos I., Georgakakis A., Kitsionas S., Hatziminaoglou E., 2006, A&A, 459, 693

Akylas A., Georgakakis A., Georgantopoulos I., Brightman M., Nandra K., 2012, A&A, 546, A98

Alexander D. M., Hickox R. C., 2012, NewAR, 56, 93

Andersen D. R., Walcher C. J., Böker T., Ho L. C., van der Marel R. P., Rix H.-W., Shields J. C., 2008, ApJ, 688, 990

Antonucci R., 1993, ARA&A, 31, 473

Antonucci R. R. J., Miller J. S., 1985, ApJ, 297, 621

Asplund M., 1998, A&A, 330, 641

Balbus S. A., 2003, ARA&A, 41, 555

Ballantyne D. R., 2008, ApJ, 685, 787

Ballantyne D., Everett J., Murray N., 2006a, The Astrophysical Journal, 639, 740

Ballantyne D. R., Shi Y., Rieke G. H., Donley J. L., Papovich C., Rigby J. R., 2006b, ApJ, 653, 1070

Ballantyne D. R., Draper A. R., Madsen K. K., Rigby J. R., Treister E., 2011, ApJ, 736, 56

Ballantyne D. R., Armour J. N., Indergaard J., 2013, ApJ, 765, 138

Barger A. J., Cowie L. L., Mushotzky R. F., Yang Y., Wang W.-H., Steffen A. T., Capak P., 2005, AJ, 129, 578

Barvainis R., 1987, ApJ, 320, 537

Bauer F. E., et al., 2004, Advances in Space Research, 34, 2555

Beckmann V., et al., 2009, A&A, 505, 417

Bianchi S., Matt G., Balestra I., Perola G., 2003, Astronomy & Astrophysics, 407, L21

Bianchi S., Guainazzi M., Matt G., Bonilla N. F., Ponti G., 2009, Astronomy & Astrophysics, 495, 421

Binney J., Tremaine S., 1987, Galactic Dynamics. Princeton University Press, Princeton

Böker T., Laine S., van der Marel R. P., Sarzi M., Rix H.-W., Ho L. C., Shields J. C., 2002, AJ, 123, 1389

Böker T., Sarzi M., McLaughlin D. E., van der Marel R. P., Rix H.-W., Ho L. C., Shields J. C., 2004, AJ, 127, 105

Bolatto A. D., et al., 2013, Nature, 499, 450

Brandt W. N., Hasinger G., 2005, ARA&A, 43, 827

Brandt W. a., et al., 2001, The Astronomical Journal, 122, 2810

Brightman M., Nandra K., 2011a, MNRAS, 413, 1206

Brightman M., Nandra K., 2011b, MNRAS, 414, 3084

Brightman M., Ueda Y., 2012, MNRAS, 423, 702

Brusa M., Gilli R., Comastri A., 2005, The Astrophysical Journal Letters, 621, L5

Buchner J., et al., 2015, The Astrophysical Journal, 802, 89

Burlon D., Ajello M., Greiner J., Comastri A., Merloni A., Gehrels N., 2011, ApJ, 728, 58

Burtscher L., et al., 2013, A&A, 558, A149

Cappelluti N., et al., 2017, The Astrophysical Journal, 837, 19

Caproni A., Livio M., Abraham Z., Mosquera Cuesta H. J., 2006, ApJ, 653, 112

Capuzzo-Dolcetta R., Miocchi P., 2008, ApJ, 681, 1136

Chan C.-H., Krolik J. H., 2016, ApJ, 825, 67

Chaudhary P., Brusa M., Hasinger G., Merloni A., Comastri A., Nandra K., 2012, Astronomy & Astrophysics, 537, A6

Chevalier R. A., Clegg A. W., 1985, Nature, 317, 44

Chitre S. M., Shaviv G., 1967, Proceedings of the National Academy of Science, 57, 573

Churazov E., et al., 2007, A&A, 467, 529

Cid Fernandes R., et al., 2004, ApJ, 605, 105

Comastri A., 2004, in , Supermassive Black Holes in the Distant Universe. Springer, pp 245–272

Comastri A., Setti G., Zamorani G., Hasinger G., 1995, A&A, 296, 1

Corbin M. R., 1995, ApJ, 447, 496

Corral A., et al., 2008, Astronomy & Astrophysics, 492, 71

Corral A., Della Ceca R., Caccianiga A., Severgnini P., Brunner H., Carrera F., Page M., Schwope A., 2011, Astronomy & Astrophysics, 530, A42

Côté P., et al., 2006, ApJS, 165, 57

Cowie L. L., Songaila A., 1986, Annual review of astronomy and astrophysics, 24, 499

Daddi E., et al., 2007, The Astrophysical Journal, 670, 156

Dadina M., 2008, A&A, 485, 417

Davies R. I., Müller Sánchez F., Genzel R., Tacconi L. J., Hicks E. K. S., Friedrich S., Sternberg A., 2007, ApJ, 671, 1388

Davis S. W., Jiang Y.-F., Stone J. M., Murray N., 2014, ApJ, 796, 107

De Luca A., Molendi S., 2004, A&A, 419, 837

Del Moro A., et al., 2015, Monthly Notices of the Royal Astronomical Society, 456, 2105

Del Moro A., et al., 2017, preprint, (arXiv:1710.01041)

Diamond-Stanic A. M., Moustakas J., Tremonti C. A., Coil A. L., Hickox R. C., Robaina A. R., Rudnick G. H., Sell P. H., 2012, ApJL, 755, L26

Dorodnitsyn A., Kallman T., 2012, ApJ, 761, 70

Dorodnitsyn A., Bisnovatyi-Kogan G. S., Kallman T., 2011, ApJ, 741, 29

Dorodnitsyn A., Kallman T., Proga D., 2016, ApJ, 819, 115

Downes D., Solomon P. M., 1998, ApJ, 507, 615

Draine B. T., 2003, The Astrophysical Journal, 598, 1026

Draper A. R., Ballantyne D. R., 2009, ApJ, 707, 778

Draper A., Ballantyne D., 2010, The Astrophysical Journal Letters, 715, L99

Ebisawa K., Ueda Y., Inoue H., Tanaka Y., White N. E., 1996, The Astrophysical Journal, 467, 419

Ebrero J., et al., 2009, A&A, 493, 55

Elbaz D., et al., 2007, Astronomy & Astrophysics, 468, 33

Elvis M., et al., 1994, ApJS, 95, 1

Elvis M., Risaliti G., Nicastro F., Miller J. M., Fiore F., Puccetti S., 2004, ApJL, 615, L25

Emmanoulopoulos D., Papadakis I., Nicastro F., McHardy I., 2013, Monthly Notices of the Royal Astronomical Society, 429, 3439

Esposito V., Walter R., 2016, A&A, 590, A49

Fabian A. C., Barcons X., Almaini O., Iwasawa K., 1998, MNRAS, 297, L11

Ferland G. J., et al., 2013, RMxAA, 49, 137

Ferrarese L., Merritt D., 2000, ApJL, 539, L9

Francis P. J., 1993, ApJ, 407, 519

Fukazawa Y., et al., 2010, The Astrophysical Journal, 727, 19

Fukazawa Y., et al., 2011, ApJ, 727, 19

Gandhi P., Horst H., Smette A., Hönig S., Comastri A., Gilli R., Vignali C., Duschl W., 2009, Astronomy & Astrophysics, 502, 457

Gebhardt K., et al., 2000, ApJL, 539, L13

Geha M., Guhathakurta P., van der Marel R. P., 2002, AJ, 124, 3073

Georgakakis A., Nandra K., Laird E., Aird J., Trichas M., 2008, Monthly Notices of the Royal Astronomical Society, 388, 1205

George I., Fabian A., 1991, Monthly Notices of the Royal Astronomical Society, 249, 352

Ghisellini G., Haardt F., Matt G., 1994, Monthly Notices of the Royal Astronomical Society, 267, 743

Giacconi R., Gursky H., Paolini F. R., Rossi B. B., 1962, Physical Review Letters, 9, 439

Gilli R., Salvati M., Hasinger G., 2001, A&A, 366, 407

Gilli R., Comastri A., Hasinger G., 2007, A&A, 463, 79

Gohil R., Ballantyne D. R., 2015, MNRAS, 449, 1449

Gohil R., Ballantyne D. R., 2017, MNRAS, 468, 4944

Gohil R., Ballantyne D. R., 2018, Monthly Notices of the Royal Astronomical Society, 475, 3543

González Delgado R. M., Heckman T., Leitherer C., 2001, ApJ, 546, 845

Goodman J., 2003, MNRAS, 339, 937

Grevesse N., Asplund M., Sauval A., Scott P., 2011, Canadian Journal of Physics, 89, 327

Gruber D. E., Matteson J. L., Peterson L. E., Jung G. V., 1999, ApJ, 520, 124

Gu Q., Dultzin-Hacyan D., de Diego J. A., 2001, RMxAA, 37, 3

Guainazzi M., Matt G., Perola G. C., 2005, Astronomy & Astrophysics, 444, 119

Harpaz A., 1984, MNRAS, 210, 633

Harrison F., et al., 2016, The Astrophysical Journal, 831, 185

Hasinger G., 2008, A&A, 490, 905

Hayakawa S., 1970, Progress of Theoretical Physics, 43, 1224

Heckman T. M., Best P. N., 2014, ARA&A, 52, 589

Heckman T. M., et al., 2011, ApJ, 730, 5

Helling C., Winters J. M., 2001, A&A, 366, 229

Hönig S. F., Beckert T., 2007, MNRAS, 380, 1172

Hönig S. F., Kishimoto M., 2010, A&A, 523, A27

Hopkins P. F., 2012, MNRAS, 420, L8

Hopkins P. F., Hernquist L., 2009, The Astrophysical Journal, 698, 1550

Hopkins P. F., Hernquist L., Cox T. J., Di Matteo T., Robertson B., Springel V., 2006, ApJS, 163, 1

Hopkins P. F., Torrey P., Faucher-Giguère C.-A., Quataert E., Murray N., 2016, MNRAS, 458, 816

House L. L., 1969, The Astrophysical Journal Supplement Series, 18, 21

Hubeny I., 1990, ApJ, 351, 632

Hubeny I., Hubeny V., 1998, ApJ, 505, 558

Hubeny I., Mihalas D., 2014, Theory of Stellar Atmospheres: An Introduction to Astrophysical Non-equilibrium Quantitative Spectroscopic Analysis. Princeton University Press

Ikeda S., Awaki H., Terashima Y., 2009, ApJ, 692, 608

Iwasawa K., et al., 2012, A&A, 546, A84

Jaffe W., et al., 2004, Nature, 429, 47

Jenkins E. B., 1987, in , Interstellar Processes. Springer, pp 533–559

Jia J., Ptak A., Heckman T., Zakamska N. L., 2013, The Astrophysical Journal, 777, 27

Jiang P., Wang J., Wang T., 2006, The Astrophysical Journal, 644, 725

Joss P. C., Salpeter E. E., Ostriker J. P., 1973, ApJ, 181, 429

Kaspi S., et al., 2001, The Astrophysical Journal, 554, 216

Kauffmann G., Heckman T. M., 2009, Monthly Notices of the Royal Astronomical Society, 397, 135

Kay C., Opher M., Kornbleuth M., 2016, The Astrophysical Journal, 826, 195

Kelly B. C., Shen Y., 2013, The Astrophysical Journal, 764, 45

Kennicutt Jr. R. C., 1998, ApJ, 498, 541

Kennicutt R. C., Evans N. J., 2012, ARA&A, 50, 531

Kim M., Wilkes B. J., Kim D.-W., Green P. J., Barkhouse W. A., Lee M. G., Silverman J. D., Tananbaum H. D., 2007, The Astrophysical Journal, 659, 29

Kishimoto M., et al., 2013, ApJL, 775, L36

Kollmeier J. A., et al., 2006, ApJ, 648, 128

Kormendy J., Richstone D., 1995, ARA&A, 33, 581

Krolik J. H., 2007, ApJ, 661, 52

Krolik J. H., Begelman M. C., 1986, ApJL, 308, L55

Krolik J. H., Begelman M. C., 1988, ApJ, 329, 702

Krumholz M. R., Thompson T. A., 2012, ApJ, 760, 155

LaMassa S. M., et al., 2017, The Astrophysical Journal, 835, 91

Lansbury G. B., et al., 2017, ApJ, 846, 20

Lawrence A., Elvis M., 2010, ApJ, 714, 561

Lehmer B. D., et al., 2012, The Astrophysical Journal, 752, 46

Leitherer C., Robert C., Drissen L., 1992, ApJ, 401, 596

Leroy A. K., Walter F., Brinks E., Bigiel F., de Blok W. J. G., Madore B., Thornley M. D., 2008, AJ, 136, 2782

Levenson N., Heckman T., Krolik J., Weaver K., Życki P., 2006, The Astrophysical Journal, 648, 111

Levin Y., 2003, ArXiv Astrophysics e-prints,

Lilly S. J., Carollo C. M., Pipino A., Renzini A., Peng Y., 2013, ApJ, 772, 119

Liu T., et al., 2017, arXiv preprint arXiv:1703.00657

Lumsden S. L., Alexander D. M., 2001, MNRAS, 328, L32

Madau P., Dickinson M., 2014, ARA&A, 52, 415

Maiolino R., 2001, in AIP Conference Proceedings. pp 199–208

Marconi A., Risaliti G., Gilli R., Hunt L. K., Maiolino R., Salvati M., 2004, MNRAS, 351, 169

Marinucci A., et al., 2014, Monthly Notices of the Royal Astronomical Society, 447, 160

Marshall F., Boldt E., Holt S., Miller R., Mushotzky R., Rose L., Rothschild R., Serlemitsos P., 1980, The Astrophysical Journal, 235, 4

Martin C. L., Kennicutt Jr. R. C., 2001, ApJ, 555, 301

Martínez-Sansigre A., et al., 2007, Monthly Notices of the Royal Astronomical Society: Letters, 379, L6

Mastropietro C., Moore B., Mayer L., Debattista V. P., Piffaretti R., Stadel J., 2005, MNRAS, 364, 607

Mathis J. S., Rumpl W., Nordsieck K. H., 1977, ApJ, 217, 425

Meisenheimer K., et al., 2007, Astronomy & Astrophysics, 471, 453

Menci N., Fiore F., Puccetti S., Cavaliere A., 2008, ApJ, 686, 219

Merloni A., 2004, MNRAS, 353, 1035

Meyer D. M., Jura M., Cardelli J. A., 1998, The Astrophysical Journal, 493, 222

Mihos J. C., Hernquist L., 1996, ApJ, 464, 641

Moretti A., et al., 2009, A&A, 493, 501

Murphy K. D., Yaqoob T., 2009, Monthly Notices of the Royal Astronomical Society, 397, 1549

Murray N., Quataert E., Thompson T. A., 2005, ApJ, 618, 569

Mushotzky R. F., Cowie L. L., Barger A. J., Arnaud K. A., 2000, Nature, 404, 459

Nandra K., Pounds K., 1994, Monthly Notices of the Royal Astronomical Society, 268, 405

Narayanan D., Bothwell M., Davé R., 2012, MNRAS, 426, 1178

Nayakshin S., 2005, MNRAS, 359, 545

Nenkova M., Sirocky M. M., Nikutta R., Ivezić Ž., Elitzur M., 2008, ApJ, 685, 160

Netzer H., 2015, ARA&A, 53, 365

Noeske K., et al., 2007, The Astrophysical Journal Letters, 660, L43

Paczynski B., 1978, AcA, 28, 91

Page K. L., O'Brien P. T., Reeves J., Turner M. J., 2004, Monthly Notices of the Royal Astronomical Society, 347, 316

Pannella M., et al., 2009, The Astrophysical Journal Letters, 698, L116

Pier E. A., Krolik J. H., 1992, ApJL, 399, L23

Pollack J. B., McKay C. P., Christofferson B. M., 1985, Icarus, 64, 471

Prieto M. A., et al., 2004, The Astrophysical Journal, 614, 135

Prieto M. A., Maciejewski W., Reunanen J., 2005, arXiv preprint astro-ph/0507071

Raban D., Jaffe W., Röttgering H., Meisenheimer K., Tristram K. R., 2009, Monthly Notices of the Royal Astronomical Society, 394, 1325

Rafikov R. R., 2001, MNRAS, 323, 445

Ricci C., Walter R., Courvoisier T. J.-L., Paltani S., 2011, A&A, 532, A102

Ricci C., et al., 2017, Nature, 549, 488

Risaliti G., 2002, A&A, 386, 379

Risaliti G., Elvis M., Fabbiano G., Baldi A., Zezas A., 2005, ApJL, 623, L93

Rosario D. J., et al., 2013, A&A, 560, A72

Rosdahl J., Teyssier R., 2015, MNRAS, 449, 4380

Rozanska A., Czerny B., 1996, AcA, 46, 233

Różańska A., Dumont A.-M., Czerny B., Collin S., 2002, MNRAS, 332, 799

Ruschel-Dutra D., Pastoriza M., Riffel R., Sales D. A., Winge C., 2014, Monthly Notices of the Royal Astronomical Society, 438, 3434

Ruschel-Dutra D., Rodríguez Espinosa J. M., González Martín O., Pastoriza M., Riffel R., 2017, preprint, (arXiv:1701.05048)

Saintonge A., et al., 2013, ApJ, 778, 2

Salak D., Nakai N., Hatakeyama T., Miyamoto Y., 2016, ApJ, 823, 68

Savage B. D., Sembach K. R., 1996, Annual Review of Astronomy and Astrophysics, 34, 279

Sazonov S., Churazov E., Krivonos R., 2015, MNRAS, 454, 1202

Schawinski K., Simmons B. D., Urry C. M., Treister E., Glikman E., 2012, Monthly Notices of the Royal Astronomical Society: Letters, 425, L61

Schmidt M., 1959, ApJ, 129, 243

Schwarzschild M., 1975, ApJ, 195, 137

Seth A. C., Dalcanton J. J., Hodge P. W., Debattista V. P., 2006, AJ, 132, 2539

Shakura N. I., Sunyaev R. A., 1973, A&A, 24, 337

Shankar F., Weinberg D. H., Miralda-Escudé J., 2009, ApJ, 690, 20

Shankar F., Weinberg D. H., Miralda-Escudé J., 2013, MNRAS, 428, 421

Shu X., Yaqoob T., Wang J., 2010, The Astrophysical Journal Supplement Series, 187, 581

Silverman J., et al., 2008, The Astrophysical Journal, 679, 118

Sirko E., Goodman J., 2003, MNRAS, 341, 501

Snow Jr T., Dodgen S., 1980, The Astrophysical Journal, 237, 708

Somerville R. S., Lee K., Ferguson H. C., Gardner J. P., Moustakas L. A., Giavalisco M., 2004, The Astrophysical Journal Letters, 600, L171

Stark D. P., Schenker M. A., Ellis R., Robertson B., McLure R., Dunlop J., 2013, The Astrophysical Journal, 763, 129

Stirpe G. M., 1991, A&A, 247, 3

Storchi-Bergmann T., Nemmen R. S., Spinelli P. F., Eracleous M., Wilson A. S., Filippenko A. V., Livio M., 2005, ApJL, 624, L13

Tacconi L. J., et al., 2013, ApJ, 768, 74

Tan J. C., Blackman E. G., 2005, MNRAS, 362, 983

Thatte N., Quirrenbach A., Genzel R., Maiolino R., Tecza M., 1997, ApJ, 490, 238

Thompson T. A., Quataert E., Murray N., 2005, ApJ, 630, 167

Tran H. D., 2001, ApJL, 554, L19

Treister E., Urry C. M., 2005, The Astrophysical Journal, 630, 115

Treister E., et al., 2006, ApJ, 640, 603

Tremaine S., et al., 2002, ApJ, 574, 740

Tremonti C. A., Moustakas J., Diamond-Stanic A. M., 2007, ApJL, 663, L77

Tristram K., et al., 2007, Astronomy & Astrophysics, 474, 837

Trump J. R., et al., 2011, ApJ, 733, 60

Tsai A.-L., Matsushita S., Kong A. K. H., Matsumoto H., Kohno K., 2012, ApJ, 752, 38

Tsang B. T.-H., Milosavljević M., 2015, MNRAS, 453, 1108

Tucci M., Volonteri M., 2017, A&A, 600, A64

Tuchman Y., Sack N., Barkat Z., 1978, ApJ, 219, 183

Ueda Y., 2015, Proceedings of the Japan Academy, Series B, 91, 175

Ueda Y., Akiyama M., Ohta K., Miyaji T., 2003, The Astrophysical Journal, 598, 886

Ueda Y., Akiyama M., Hasinger G., Miyaji T., Watson M. G., 2014, ApJ, 786, 104

Urry C. M., Padovani P., 1995, PASP, 107, 803

Vito F., Gilli R., Vignali C., Comastri A., Brusa M., Cappelluti N., Iwasawa K., 2014, MNRAS, 445, 3557

Vollmer B., Beckert T., Davies R. I., 2008, A&A, 491, 441

Wada K., Norman C. A., 2002, ApJL, 566, L21

Wada K., Tomisaka K., 2005, ApJ, 619, 93

Walcher C. J., et al., 2005, ApJ, 618, 237

Walter F., Weiss A., Scoville N., 2002, ApJL, 580, L21

Wang J.-X., et al., 2007, The Astrophysical Journal, 657, 95

Watabe Y., Umemura M., 2005, ApJ, 618, 649

Weaver K., Gelbord J., Yaqoob T., 2001, The Astrophysical Journal, 550, 261

Weingartner J. C., Draine B. T., 2001, ApJ, 548, 296

Weingartner J. C., Draine B. T., Barr D. K., 2006, ApJ, 645, 1188

Westfall K. B., Andersen D. R., Bershady M. A., Martinsson T. P. K., Swaters R. A., Verheijen M. A. W., 2014, ApJ, 785, 43

Wolf C., Wisotzki L., Borch A., Dye S., Kleinheinrich M., Meisenheimer K., 2003, A&A, 408, 499

Worsley M. A., et al., 2005, MNRAS, 357, 1281

Yaqoob T., Padmanabhan U., 2004, The Astrophysical Journal, 604, 63

Yaqoob T., George I., Nandra K., Turner T., Serlemitsos P., Mushotzky R., 2001, The Astrophysical Journal, 546, 759

Yencho B., Barger A., Trouille L., Winter L., 2009, The Astrophysical Journal, 698, 380

Zamorani G., et al., 1981, ApJ, 245, 357

Zhou X.-L., Wang J.-M., 2004, The Astrophysical Journal Letters, 618, L83

van Hoof P. A. M., Weingartner J. C., Martin P. G., Volk K., Ferland G. J., 2004, MNRAS, 350, 1330

VITA

Raj Gohil was born in Gujarat in India and moved to the U.S.A. in 2007. Since high school, he was always interested in pursuing a Ph.D. in Physics. Upon his completion of a B.S. in Physics from the University of California - Los Angeles, he began his doctoral degree at the Georgia Institute of Technology. He believes life is like an ocean with the depth of treasures that one cannot fathom; hence, just dive in and explore as much as one can. Besides solving problems, Raj enjoys developing new skills; therefore, he likes to spend his free time in philosophical discussion with friends, playing sports (table tennis, racquetball, or badminton), guitar, or dancing salsa.